이학박사학위논문

Quantum measurements of electron spin degree of freedom in solid state system: from ensemble time averaged measurements to single-shot detection of individual spins

고체소자 전자스핀 자유도의 양자측정: 앙상블 평균 측정과 단발측정을 중심으로

August 2022

서울대학교 대학원
물리천문학부
김제현

Quantum measurements of electron spin degree of freedom in solid state system: from ensemble time averaged measurements to single-shot detection of individual spins

Advisor: Dohun Kim

Submitting a Ph.D. Dissertation of Public Administration

August 2022

Graduate School
Seoul National University
Physics Major

Jehyun Kim

Confirming the Ph.D. Dissertation written by
Jehyun Kim
August 2022

Chair	이탁희	(Seal)
Vice Chair	김도헌	(Seal)
Examiner	최현용	(Seal)
Examiner	장준호	(Seal)
Examiner	장차운	(Seal)

Acknowledgments

박사 학위 논문의 챕터 하나하나를 마무리 지으면서, 그 동안 같이 연구를 했던, 많은 도움을 주셨던 분들이 떠올랐습니다. 긴 시간 동안 많은 분들의 도움이 있었기에 이 논문을 무사히 잘 마무리 할 수 있었고, 이 자리를 빌어 감사의 말씀을 전하고자 합니다. 먼저, 저의 지도 교수님인 김도헌 교수님께 감사의 말씀을 드립니다. 여러 우여곡절을 거친 후 교수님을 만나서, 정말 좋은 연구를 하며, 연구에 대한 많은 것들을 배울 수 있었습니다. 연구적으로 많이 거칠고, 부족했던 저를 지도해주시고 지지해주셔서 감사 드립니다. 앞으로도 좋은 방향으로 열심히 하여 부끄럽지 않은 제자가 되도록 노력 하겠습니다.

저의 챕터 2, 3 관련 연구에 많은 도움을 주신 KIST에 장차운 박사님께 감사의 말씀을 드립니다. 박사님 덕분에, 저온 앙상블 스핀 측정에 대해 많이 배울 수 있었고 재미있게 연구했던 기억이 납니다. 2주마다 KIST 에서 측정을 하는 시간이 기다려졌고, 덕분에 좋은 결과를 학위논문에 실을 수 있었습니다. 더불어, 이론적인 해석에 도움을 주신 홍석민 박사님과, 고품질의 재료를 개발하여 제공해준 Johnpierre Paglione 교수님 연구팀, 재료분석을 도와주신 천동원 박사님, 이차원 재료를 이용한 소자 제작에 도움을 주신 최현용 교수님 연구팀 분들께 감사의 말씀을 드립니다.

챕터 4,5 관련 연구에 많은 도움을 주신 우리 연구실 연구원 모두에게 감사의 말씀을 드립니다. 상당히 어렵고 큰 주제의 연구인데 같이 참여하여 열심히 일한 많은 분들의 도움이 있었기에, 좋은 결과를 얻을 수 있었습니다. 측정 관련하여 많은 도움을 준 장원진, 윤종인 연구원, 극저온 냉동기 설치 및 양자점 소자 공정에 있어 많은 도움을 준 송영욱, 박재민, 조민균, 장현규, 손한서 연구원께 감사의 말씀을 드립니다. 더불어 GaAs 양자점 소자 공정에 있어 큰 도움을 주신 부산대학교 정윤철 교수님 연구팀, 특히 정환철 연구원께 감사의 말씀을 드립니다. 비록 다른 연구주제로 많은 접점은 없었지만, 같은 연구실에서 같이 동고동락한 머신러닝의 정경훈, 조경민, 김경훈, NV팀의 윤지원, 김기호, 박성준 연구원께도 너무 고생 많으셨고 감사의 말씀을 드립니다.

마지막으로 오랫동안 지지해주고 묵묵히 기다려주신 부모님께 감사의 말씀을 드립니다. 이제 또 다른 시작을 앞두고 있는 시점에서, 그 동안 많은 도움을 주신 분들 잊지 않고, 저 또한 여러분들에게 도움이 될 수 있는, 더욱 나은 연구자가 되도록 노력하겠습니다. 그 동안 도움을 주신 모든 분들께 다시 한번 진심으로 감사의 말씀을 드립니다. 감사합니다!

2022년 8월

김제현

Abstract

Starting with the discovery of a magnet known as a mysterious stone in ancient times, the discovery of spin revealed through the modern Stern Gerlach's experiment has had a tremendous impact on our lives and spurred a big change in our life. Together with mass and charge, which are the basic physical quantities of matter, spin is currently being applied in many places of life. In particular, in the field of electronic devices for storing and processing information, spin is an indispensable physical quantity. According to the size of the system, I tried to classify the application into an ensemble spin system that can be explained by a classical spin picture, and a few-electron spin system that can be explained by a quantum spin picture. In the case of classical spin, spin is used as a spin memory device and a spin transistor in the spintronics field, and in the case of quantum spin, electron spin is being applied in the field of quantum computing as a representative field of quantum information. A common important part for these applications is the technology to control and read the electron spin states precisely.

My thesis is divided into two main parts. The first part is about the study of detecting ensemble spins flowing on the surface of SmB_6 single crystal. SmB_6 is a representative Kondo insulator, and theoretical and experimental studies have been conducted to show that spin-momentum locking property exists on the surface of SmB_6. However, meanwhile, researches have not been conducted with an electrical spin measurement method, and I tried to use a method called potentiometric measurement where a ferromagnetic material is used as a detector in order to measure the direction of ensemble spin, and showed a spin polarized current flowing on the surface of SmB_6. In addition, by changing the positions of the terminals for current and

voltage, the spin polarized current induced by the ferromagnetic material is measured using the SmB_6 surface state in reverse. These results can be interpreted as an electrical measurement results showing that a spin-momentum locking property exists on the SmB_6 surface.

The second part of the research is about forming spin singlet-triplet qubits in GaAs quantum dot devices, and controlling and measuring their spin state. In order to achieve spin-to-charge conversion of singlet-triplet qubit states, a new method is demonstrated using energy-selective tunneling between doubly occupied quantum dots and electron reservoirs, commonly called Elzerman type readout. In order to further improve this method, real time Hamiltonian parameter estimation is introduced to improve the fidelity of energy-selective tunneling readout. Optimization of readout fidelity enables to reduce a single-shot measurement time down to 16 μs on average, with adaptive initialization and efficient qubit frequency estimation based on real-time Bayesian inference. Active frequency feedback is also demonstrated, resulting in quantum oscillation visibility, single-shot measurement fidelity, and state initialization fidelity up to 97.7%, 99%, and over 99.7%, respectively.

Depending on the physical size of the system, or whether the action value of the system is near Planck's constant or not, an appropriate method should be considered to control and measure the spin of the system. I believe that my research can be helpful in this regard where how spin-to-charge conversion, measurement setup and design for device structure should be planned and expanded for precisely controlling and measuring spin states of any quasiparticles.

Keywords : Spin measurement, Spin valve, Spin polarization, Spin singlet−triplet qubit, Energy selective tunneling, Single−shot measurement

Student Number : 2016−27344

Table of Contents

Chapter 1. Introduction

1.1. Background & Outline

My thesis is divided into two main parts. The first part is about the study of detecting ensemble spins flowing on the surface of SmB_6 single crystal. The second part of the research is about forming spin singlet-triplet qubits in GaAs quantum dot devices, and controlling and measuring their spin states. In this section, basic backgrounds are provided. Section 1.1.1 and 1.1.2 are for the first part, ensemble spin system. Section 1.1.3~1.1.6 are for the second part, a few-electron spin system.

1.1.1. Expansion of spin valves

A spin valve, which is the most basic form of spin devices, has a structure where two magnetic layers exist and a non-magnetic material are inserted between them as shown in Fig. 1(a). Electrical resistance of the spin valve can change depending on the relative alignment of the magnetization of the two magnetic layers, that is, parallel or antiparallel. This phenomenon is known as giant magnetoresistive effect, and for this discovery, the 2007 Nobel prize in Physics was awarded (Fig. 1(b)). In such a spin valve, the lower layer can be replaced with a layer through which spin polarized current flows. Because spin polarized current flowing in the bottom layer can act as an effective magnetization, similar magnetoresistive effect can be observed. Recently, a spin polarized layer is created by injecting electron spin into a non-magnetic layer, or by flowing a current through a material with spin momentum locking properties. In this structure, top magnetic layer can be used as a detector in order to measure the spin of the lower layer by reducing the size of the upper magnetic layer [1]. This idea is called potentiometric spin measurement, which will be explained in detail in chapter 2 and 3.

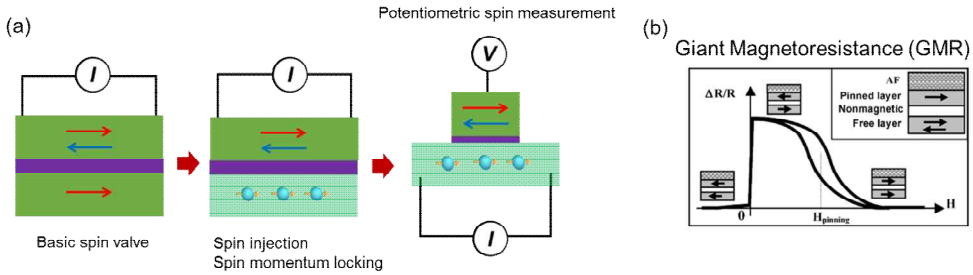

Fig. 1. (a) Schematic structures and variants of a spin valve. A current is applied through two terminals, denoted by *I*, and change in a voltage is measured at a ferromagnet contact, denoted by *V*. (b) Representative result for giant magnetoresistance, showing large change in a resistance according to the relative alignment of the magnetization of the two magnetic layers.

1.1.2. Surface states of topological insulators

Topological insulator has surface state in the gap and its Fermi level is located in the gap, which introduces two remarkable properties in surface states (Fig. 2.) [2]. One is electrical conduction through surface states and the other is spin-momentum locking property where electrons traveling into one direction should have their spins in a specific direction, usually orthogonal to the direction of a current. Although these properties can be demonstrated using other techniques such as spin angle-resolved photoemission spectroscopy or ferromagnetic resonance, using a spin valve device aforementioned is also effective method to demonstrate topological nontrivial states due to simpleness or application prospect of the setup. SmB_6 single crystal, a representative Kondo insulator, is a material system that I am interested in, and the process of revealing the topological properties of SmB_6 are shown in chapter 2 and 3.

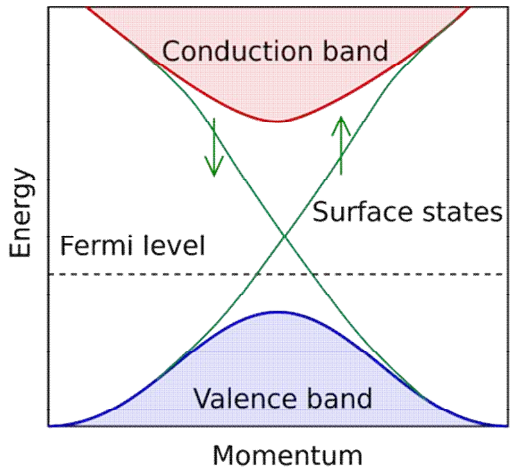

Fig. 2. An idealized band structure for a topological insulator. The Fermi level resides in the bulk band gap where topologically-protected spin-textured Dirac surface states exist [2].

1.1.3. Classical bits vs Quantum bits

From the past, it was important issues to quickly and accurately spread the information meaning the message people wanted to convey. So, various methods to convey the information were developed and used according to the technological capabilities of the time. The telegraph using the modern Morse code based on binary number was a revolutionary invention enabling to transmit the information at the speed of light. However, it was difficult to process and store the information using it. Recent semiconductor technologies have made it possible to store, process and transmit information quickly, and the key basic element, a representative product of this technology, is field effect transistors (FETs). FETs are nono-scale devices that can turn the flow of current on and off using electric field that we can control quickly and accurately. When current flows through the FET, the state of the FET corresponds to 1, and when no current flows, the state corresponds to 0. Such a binary system can express arbitrary information and is called classical bits.

On the other hand, the quantum bit is based on the quantum two level

system where the two possible states obeys the laws of quantum mechanics, thereby showing the unique properties such as superposition and entanglement. The quantum bit called qubit can be described as the linear combination of $|1\rangle$ and $|0\rangle$ as shown below.

$$\psi = a|0\rangle + b|1\rangle, \text{ where } |a|^2 + |b|^2 = 1$$

Arbitrary state of the qubit can be mapped on a Block sphere surface where two bases are located at north and south poles, respectively, as shown in Fig. 3. Block sphere is very useful tool because we can check easily the changes of the state of the qubit with time.

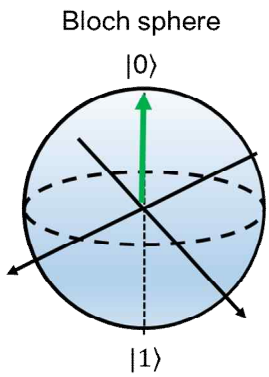

Fig. 3. The Bloch sphere is a geometrical representation of the pure state space of a qubit, named after the physicist Felix Bloch.

1.1.4. Types of spin qubit

The spin of electrons is a fundamental quantity along with mass and charge. The spin interacts with the magnetic field, resulting in the system having different energy levels which depend on the direction to the spin. Furthermore, even without the magnetic field, the system energy can be changed according to the spin direction because the electrons follow the exchange statistics as fermions connecting the symmetry of spatial wave function to the symmetry of spin wave function. Therefore, two level

systems where the energy of the system depends on the spin status are called the spin qubits.

For the spin qubits operating with one electron, the two distinct states are expressed as spin-up and down under an external magnetic field. The energy difference between spin-up and down states is the Zeeman splitting. For operation of the single spin qubit, the AC magnetic field with the frequency corresponding to the Zeeman splitting is required for the coherent oscillations between spin-up and down states [3], which is called by the Larmor frequency $w_L = \frac{g\mu_B B}{\hbar}$ where g is the g-factor, μ_B is the Bohr magneton and B is the amplitude of the static magnetic field. The direction of the AC magnetic field is perpendicular to the static magnetic field direction. The coherent rotations can be performed around any vector in x-y plane of Bloch sphere, the rotation axis can be determined by the phase of the AC magnetic field. The angular frequency of the rotations is given by the Rabi frequency:

$$\Omega = \frac{g^* \mu_B B_{AC}}{2\hbar}$$

where g* is the effective electron g-factor and B_{AC} is the amplitude of the AC magnetic field.

For the spin qubits operating with two electrons [4], the two states for operation are singlet and triplet states. In an external magnetic field, the triplet state with spin 1 is split into three spin states:

$$S = \frac{|\uparrow\downarrow\rangle - |\downarrow\uparrow\rangle}{\sqrt{2}}$$

$$T_0 = \frac{|\uparrow\downarrow\rangle + |\downarrow\uparrow\rangle}{\sqrt{2}},\ T_+ = |\uparrow\uparrow\rangle,\ T_- = |\downarrow\downarrow\rangle.$$

The common choice for logical qubit is combination of the S and T_0 states because the S and T_0 states with 0 magnetic quantum number are not influenced by the fluctuation of the static magnetic field, making sure that the leakage into other triplet states is minimized. The singlet-triplet qubit can show the coherent oscillations around the z-axis due to the exchange

energy J (the energy difference between S and T_0). For universal qubit control, qubit rotations around a second axis are needed, and can be realized by the local magnetic field gradient between the two electrons generated by the stray field of micro-magnet or the local nuclei.

1.1.5. GaAs heterostructures and device for the formation of the quantum dots

In solid states physics, quantum dots are usually referred as semiconductor particles with a few nanometers in size, having discrete energy levels due to quantum mechanical effects. In the early days of the quantum dot research, the quantum dots were fabricated using etching technique to form physical confinements in all directions. However, this technique have disadvantages in tunability for quantum dots formation. The method using electrical gates to form quantum dots emerged as a promising technique where electrical gates form confinement potential in xy-plane and confinement in z-axis is provided by 2DEG of semiconductor materials.

GaAs/AlGaAs heterostructures grown by molecular beam epitaxy (MBE) are suitable systems to form gate-defined quantum dots. They provide confinement potential in z-axis by a band engineering as shown in Fig. 4(a). At low temperature, 2DEG is formed at the interface between AlGaAs with larger band gap and GaAs with smaller band gap. Si delta doping layer supplies free electrons in 2DEG and the spacer can reduce the events of scattering of electrons occurred by inhomogeneous electric potential induced by Si dopant atoms.

Fig. 4(b) shows the platform where the quantum dots can be formed, showing a schematic of a semiconductor quantum dot device [5]. Nano gates are fabricated on the surface through a nano fabrication and a voltage is applied to the gate in order to create an electrical potential well in the two-dimensional electron layer. By controlling the gate voltage, the desired quantum dots array is formed. In order to measure the state of the qubit, for

example, single spin qubit, a current should flow near the qubit. The information we can obtain by flowing an electric current is, in fact, information about the entry and exit of electrons into quantum dots. In other words, whenever an electron goes out and enters a quantum dot, the change in current flow can be detected. This can be enabled by $Q = CV$ where Q is charge, C is capacitance between qubit and senor, and V is effective voltage applied to sensor, which is the relationship between the capacitive-coupled quantum dot and the sensor. Since the C value is very small in the nano device, the entry and exit of one electron from the quantum dot can lead to applying the effective voltage to the neighboring sensor, resulting in measurable change in current through the sensor.

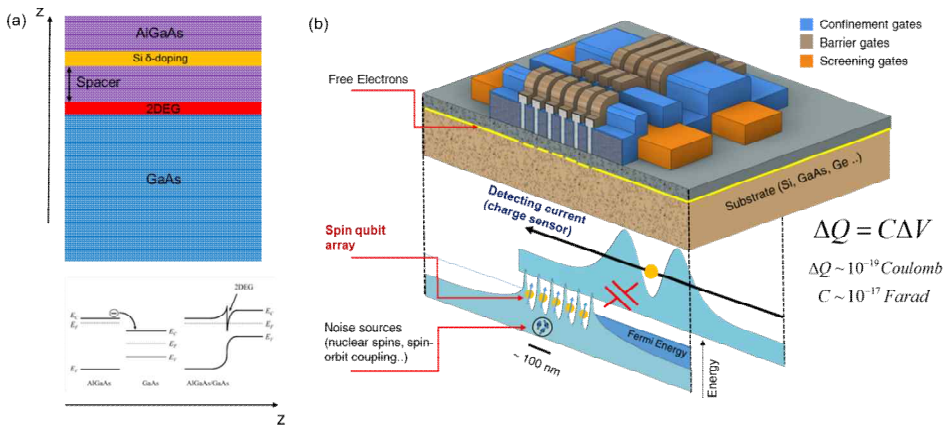

Fig. 4. (a) Cross section of GaAs/AlGaAs heterostructure, showing the formation of quantum well at the interface between GaAs and AlGaAs. (b) Schematic structure of the quantum dot device where spin qubit array and charge sensor are located in the potential well in 2DEG.

1.1.6. Energy diagram for singlet-triplet qubit in double quantum dots [6]

In this section, energy diagram for singlet-triplet qubit is shown in Fig. 5 and why the diagram is drawn that way will be explained in a qualitative way. In Fig. 5, labeling (m,n) means the absolute number of electrons

confined on the (left dot, right dot) in the ground state. When the total number of electrons is fixed as 2, (2,0) and (1,1) charge states are focused for operating the singlet-triplet qubit. Figure 5 shows the energy diagram for singlet-triplet qubit as a function of detuning ε that is the relative energy difference between the (2,0) and (1,1) charge states. For $\varepsilon < 0$, the charge configuration in the ground energy is (2,0) where singlet spin state has lower energy than triplet states because symmetric triplet states should have anti-symmetric spatial part which makes one electron occupy orbital state with higher energy, whereas, for $\varepsilon > 0$, the ground charge configuration is (1,1) where four spin states are accessible: the singlet, denoted S, and three triplets, denoted T_-, T_0, and T_+, corresponding to magnetic quantum number -1, 0, and +1, respectively.

In the absence of interdot tunneling and an external magnetic field, the singlet and triplet spin states in the (1,1) charge configuration are degenerate. At a finite external magnetic field, T_+ and T_- states are split by the Zeeman energy from the T_0 state. When interdot tunneling is present, the (2,0) and (1,1) charge states hybridize, resulting in an exchange splitting $J(\varepsilon)$ between S and T_0 together with forming an anti-crossing at $\varepsilon = 0$. With decreasing detuning from zero detuning, $J(\varepsilon)$ increases exponentially. For large positive detuning, exchange splitting vanished, and S(1,1) and T_0(1,1) states become degenerate. However, inhomogeneous magnet field in double quantum dots induced by GaAs nuclei spin makes S(1,1) and T_0(1,1) states mix through the hyperfine interaction, resulting in eigenstates being $|\uparrow\downarrow\rangle$ and $|\downarrow\uparrow\rangle$ at large positive detuning.

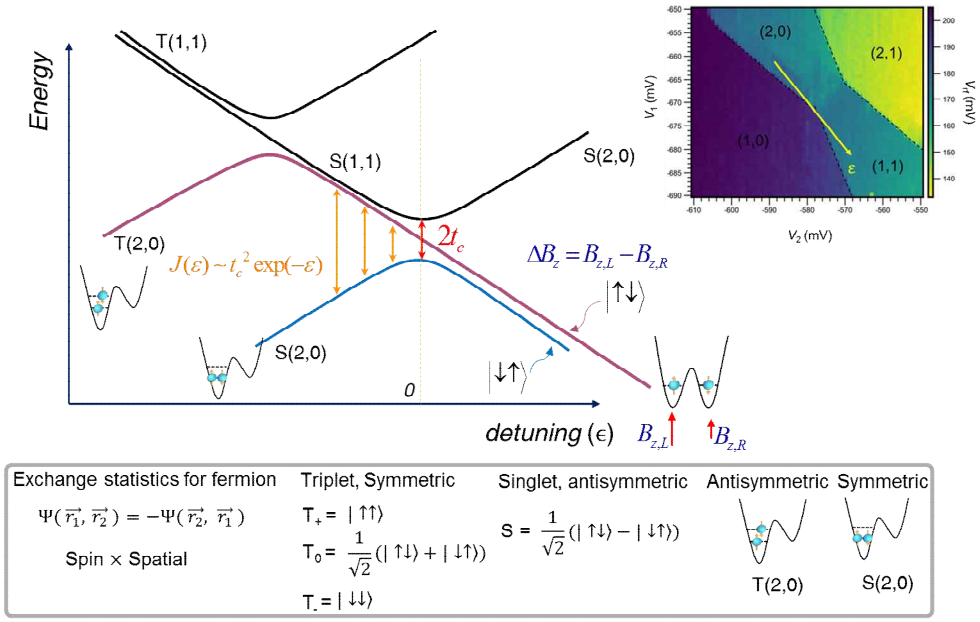

Fig. 5. Energy diagram for singlet-triplet qubit as a function of detuning ε with the presence of interdot tunnel coupling and inhomogeneous magnetic field. Upper right figure is a charge stability diagram including the region of interest. Lower box shows the symmetry of singlet and triplet spin parts, and their spatial parts.

1.2. References

[1] S. Hong, V. Diep, S. Datta, and Y. P. Chen, *Modeling potentiometric measurements in topological insulators including parallel channels*, Phys. Rev. B **86,** 085131 (2012).

[2] J. E. Moore, *The birth of topological insulators*, Nature **464,** 194 (2010).

[3] Rabi, II, *Space quantization in a gyrating magnetic field*, Physical Review **51,** 0652 (1937).

[4] J. Levy, *Universal quantum computation with spin-1/2 pairs and Heisenberg exchange*, Phys. Rev. Lett. **89,** 3 (2002).

[5] N. P. de Leon *et al.*, *Materials challenges and opportunities for quantum computing hardware*, Science **372,** 253 (2021).

[6] J. R. Petta, A. C. Johnson, J. M. Taylor, E. A. Laird, A. Yacoby, M. D. Lukin, C. M. Marcus, M. P. Hanson, and A. C. Gossard, *Coherent manipulation of coupled electron spins in semiconductor quantum dots*, Science **309,** 2180 (2005).

Chapter 2. Electrical detection of surface spin polarization of candidate topological Kondo insulator SmB_6

Jehyun Kim[1†], Chaun Jang[2†], Xiangfeng Wang[3], Johnpierre Paglione[3], Seokmin Hong[2], Jekwan Lee[4], Hyunyong Choi[4] and Dohun Kim[1*]

[1]*Department of Physics and Astronomy, and Institute of Applied Physics, Seoul National University, Seoul 08826, Korea*

[2]*Center for Spintronics, Korea Institute of Science and Technology, Seoul 02792, Korea*

[3]*Center for Nanophysics and Advanced Materials, Department of Physics, University of Maryland, College Park, MD 20742-4111, USA*

[4]*School of Electrical and Electronic Engineering, Yonsei University, Seoul 03722, Korea*

[†]*These authors contributed equally to this work.*

**Corresponding author: dohunkim@snu.ac.kr*

This work was published in "Physical Review B"

2.1. Abstract

The Kondo insulator compound SmB_6 has emerged as a strong candidate for the realization of a topologically nontrivial state in a strongly correlated system, a topological Kondo insulator, which can be a novel platform for investigating the interplay between nontrivial topology and emergent correlation-driven phenomena in solid state systems. Electronic transport measurements on this material, however, so far showed only the robust surface-dominated charge conduction at low temperatures, lacking evidence of its connection to the topological nature by showing, for example, spin polarization due to spin–momentum locking. Here, we find evidence for surface state spin polarization by electrical detection of a current-induced spin chemical potential difference on the surface of a SmB_6 single crystal. We clearly observe a surface-dominated spin voltage, which is proportional

to the projection of the spin polarization onto the contact magnetization, is determined by the direction and magnitude of the charge current and is strongly temperature-dependent due to the crossover from surface to bulk conduction. We estimate the lower bound of the surface state net spin polarization as 25% based on the quantum transport model providing direct evidence that SmB_6 supports metallic spin helical surface states.

2.2. Introduction

Recent theoretical study identifies SmB_6 as a member of a newly classified family of strong topological insulators, topological Kondo insulators [1-4], in which topologically protected surface states reside in the bulk Kondo band gap at low temperatures due to strong spin–orbit coupling. Following the measurement of the robust surface conduction below several Kelvin [5-7] superimposed with bulk insulating behaviour with a *d–f* hybridization induced gap in the range of 10–20 meV at intermediate temperatures below 300 K, many experimental efforts have been designed to probe the topological nature of the surface conducting states in this material [8-12].

While the two-dimensional nature of the surface band and surface spin polarization has been confirmed by surface-sensitive probes such as photoemission [11,13], and most recently, the magnetic resonance induced spin pumping technique showed the possibility to inject a non-equilibrium spin current into the surface of SmB_6 [12], direct electrical measurement of surface current-induced spin–momentum locking, the unique feature of topological insulators, has not been performed in a simple transport geometry.

2.3. Results

2.3.1. Principle of potentiometric spin measurement

Figure 1(a) shows the simplified spin–momentum relation in SmB_6 near the Fermi energy revealed by recent photoemission studies [11] for both $\bar{X}$ and $\bar{\Gamma}$ high-symmetry points. When the electrons are placed under an electrochemical potential difference, for example, in the x-direction, the electrons moving to the right (red arrow) have higher occupation than the electrons going to the left (blue arrow), which leads to a difference between the electrochemical potentials for spin up $\mu_{\uparrow}$ and down $\mu_{\downarrow}$. This momentum asymmetry leads to a spin polarized current in the y-direction due to spin–momentum locking, thus the presence of the spin–momentum locking property in the SmB_6 surface state can be shown electrically by detecting the spin polarized current generated by the electrochemical potential difference. We note that the surface bands in SmB_6 exhibit spin–momentum relation, hence the sign of the expected spin voltage [14-16], opposite to other topological insulators like Bi_2Se_3 [4,17], as we discuss below.

Here, we use a specially designed potentiometric geometry, as shown in Fig. 1(c), to probe the aforementioned spin-dependent chemical potential difference induced by momentum imbalance. A bias current flows through a non-magnetic contact on the SmB_6 surface with the (100) crystallographic plane in the x-direction, and the transverse voltage V_{xy} is measured between a permalloy magnetic contact (Py) and a reference non-magnetic contact. Figure 1(d) shows the electrochemical potential for spin up $\mu_{\uparrow}$ and down electrons $\mu_{\downarrow}$ as a function of the SmB_6 channel position. The ferromagnetic contact can detect spin-dependent electrochemical potentials according to its magnetization direction, and the spin voltage corresponding to the difference between the electrochemical potentials for spin up and down can be expressed as follows, based on the quantum transport model [18,19].

$$\Delta V_{xy} = V_{xy}(\boldsymbol{M}) - V_{xy}(-\boldsymbol{M}) = |I_b| R_B P_{FM} (\boldsymbol{p} \cdot \boldsymbol{M}_u), \quad (1)$$

where ΔV_{xy} is the spin voltage defined as the difference of the measured electrochemical potential V_{xy} between the opposite detector magnetization $\boldsymbol{M}$ controlled by the external magnetic field $\vec{H}_{ext}$, and ΔV_{xy} is proportional to the magnitude of the bias current $|I_b|$, ballistic resistance of the channel R_B, spin polarization of the ferromagnetic detector P_{FM}, and inner product between the spin polarization of the TI surface $\boldsymbol{p}$ and unit vector $\boldsymbol{M}_u$ along the magnetization of the ferromagnetic detector. As Eqn. 1 indicates, we measure ΔV_{xy} as a function of the experimental parameters such as the direction and magnitude of I_b, $\boldsymbol{M}$ and temperature T and confirm the current-induced spin polarization on the surface of SmB_6.

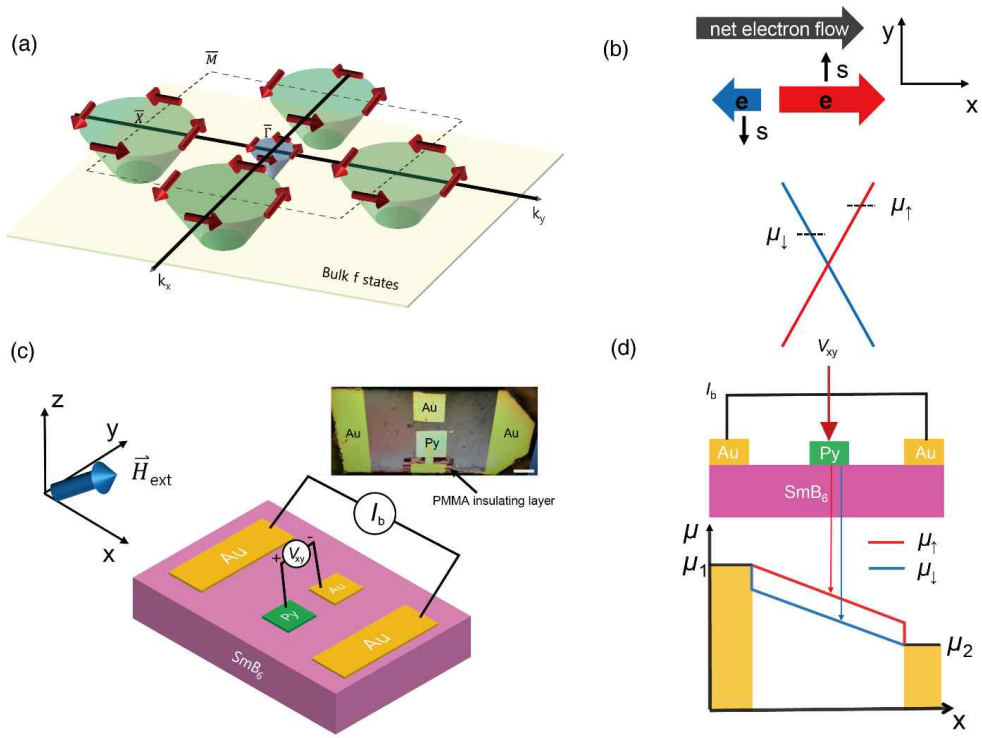

Fig. 1. Surface spin texture and potentiometric spin measurement in SmB_6. (a) Anti-clockwise spin texture for the surface band in SmB_6 near the Fermi energy shown by spin and angle resolved photoemission spectroscopy and first-principles calculations [2,11]. (b) Degree of electrons occupation in channel and spin-dependent electrochemical potential under electrochemical bias. The length of the

red and blue arrows indicates the degree of moving electrons with spin $\boldsymbol{S}$. (c) Measurement configuration for detecting spin voltage. Inset: optical microscope image of the device. The scale bar is 100 μm. (d) Electrochemical potential with respect to the position of the channel, illustrating concepts of the potentiometric spin measurement.

2.3.2. Measurement of the current-induced spin polarization

We first show that an electrochemical potential bias can induce a spin polarization that is reflected in a non-zero ΔV_{xy} measured by the magnetic detector. As shown in Fig. 2(a), V_{xy} is measured by sweeping an external magnetic field in the y-axis H_y to control the detector magnetization direction while applying I_b along the x-axis. Figures 2(b) and 2(c) show representative spin voltage data recorded with I_b of +100 μA and −100 μA, respectively. As the current is applied in the +x (−x) direction, where the momenta of the electrons are in the −x (+x) direction, the direction of the current-induced spin polarization is parallel to the –y (+y) axis due to the anti-clockwise spin texture (see the insets of Fig. 2(b) and 2(c) for the detailed directions of the electron momentum $\boldsymbol{I}_e$, $\boldsymbol{p}$, and $\boldsymbol{M}$). In both Fig. 2(b) and 2(c), a high (low) voltage is measured when the $\boldsymbol{M}$ of the ferromagnet is parallel (antiparallel) to $\boldsymbol{p}$ [14,20] (see 2.3.2.S1), consistent with the spin–momentum relation in SmB_6 [2,4]. The measured voltage switches near the coercive field of Py (see 2.3.2.S2), which can be explained by the fact that the sign of $\boldsymbol{p}\cdot\boldsymbol{M}_u$ in Eqn. 1 changes when the direction of the magnetization is switched. Moreover, the polarity of the hysteresis loop in Fig. 2(b) and 2(c) is the opposite reflecting the fact that the current-induced spin polarization direction is dependent on the direction of I_b. More specifically, the measured ΔV_{xy}, which is a difference between V_{xy} ($\boldsymbol{M}$//y-axis) and V_{xy} ($\boldsymbol{M}$//-y-axis), is shown in Fig. 2(d) as a function of I_b and exhibits a clearly linear response. Therefore, the measured ferromagnetic spin voltage as a function of the magnitude and direction of $\boldsymbol{M}$ and I_b strongly indicates

electrical measurement of the current-induced spin polarization on the surface of SmB_6. Additionally, we find spin-to-charge conversion in the SmB_6 surface state through a reciprocal geometry measurement consistent with the Onsager reciprocal relation (see 2.3.2.S3). In section 2.3.2.S4, we further discuss the degradation of ΔV_{xy} in the non-linear transport regime at high $|I_b|$ due to Joule heating and subsequent bulk carrier population [21].

The second equality in Eqn. 1 provides a quantitative estimation of the degree of surface ensemble spin polarization $|\boldsymbol{p}|$. We estimate $|\boldsymbol{p}|$, extracted from the slope of $\Delta V_{xy}(I_b)$ dependence (see Fig. 2(d)), as ~ 25%, based on the following experimental conditions and assumptions: $1/R_B$ is given by q^2/h times the number of modes $k_F W/\pi$, where $W = 500\,\mu m$ is the width of the current channel, the total Fermi wave number k_F (0.67 $Å^{-1}$) [13] can be determined as $k_{F\alpha}+2k_{F\beta}$, where $k_{F\alpha}$ and $k_{F\beta}$ are the Fermi wave numbers of the α and β bands in the first Brillouin zone, respectively, and the P_{FM} of Py at low temperatures is 0.38 [22]. We note that this is a conservative estimation of $|\boldsymbol{p}|$ since we assume 100% single-surface-dominated conduction, as well as perfect operation of ferromagnetic detector. The inclusion of experimental imperfections, such as the current path through not only the top but also the bottom surface [6], possible (although small) current leakage through bulk or imperfect detection efficiency of the ferromagnetic detector, will only make the estimation of $|\boldsymbol{p}|$ higher, so that our estimation sets the lower bound of the surface current-induced ensemble spin polarization of SmB_6.

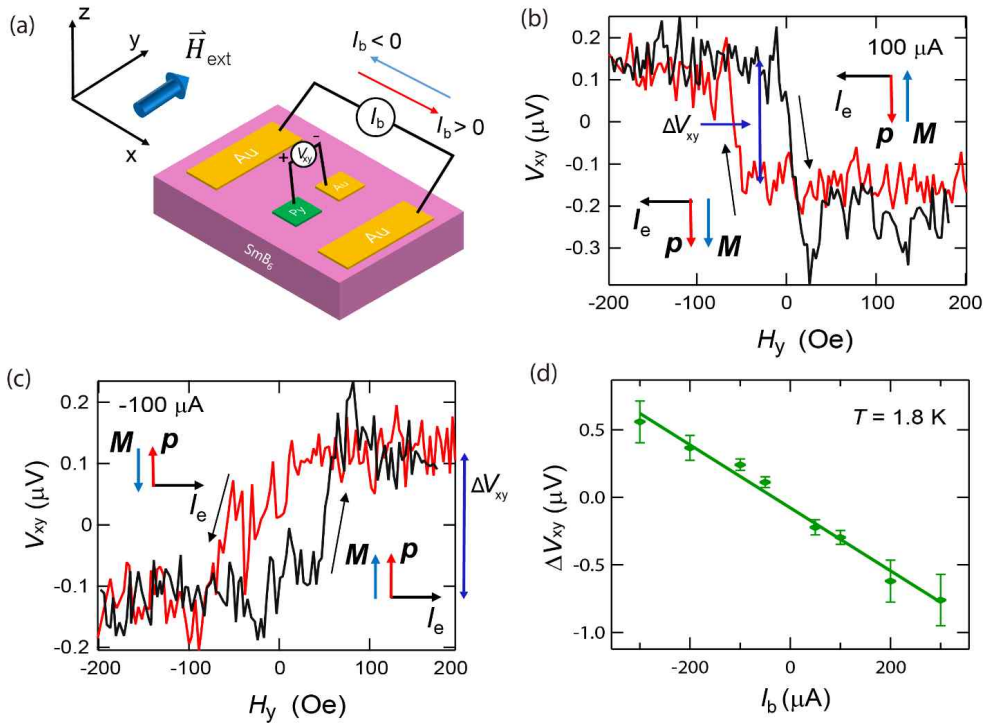

Fig. 2. Measurement of current-induced surface channel spin polarization. (a) Schematic of the transport measurements. A constant current I_b is applied in the x-direction while sweeping a magnetic field in the y-direction, which is orthogonal to the bias current direction (co-linear with the spin polarization direction). (b), (c) Magnetic field dependence of the voltage measured at the ferromagnetic contact for I_b of (b), +100 μA and (c), −100 μA. Inset: black, red and blue arrows indicate the direction of the electron momentum $\boldsymbol{I}_e$, $\boldsymbol{p}$ and $\boldsymbol{M}$ respectively. (d) Dependence of spin voltage ΔV_{xy} on I_b measured at 1.8 K.

2.3.2.S1. Principle of spin-dependent electrochemical potential detection

Figure 2.S1 shows schematics of density of state of 4s and 3d electrons in ferromagnetic detector and spilt electrochemical potential for spin up and down under positive I_b in the SmB_6 channel. Left (right) schematic density of state is corresponding to ferromagnetic detector whose $\boldsymbol{M}$ is parallel to the –y (y) direction and its majority spin direction points in the y (−y) direction due to the negative charge of electron. When the current is applied in the x direction, split electrochemical potential for spin up (y-direction)

and down (−y-direction) is depicted in the middle of two density of states. Typical ferromagnet metals like Fe, Co, and Ni have strongly minority-dominated bands near the Fermi energy so one would expect minority spin of ferromagnet is mainly connected to the TI channel. But due to the tunneling process involved in the structure the s-like electrons with a lighter effective mass contribute more compared to d-like electrons which are expected to decay rapidly into a barrier. Since the s-like electrons tend to have opposite spin in sign, the dominant spin direction in the tunneling process is parallel to majority spin direction of ferromagnet. Consequently, ferromagnetic detector can mainly read out electrochemical potential for spin whose direction is parallel to its 3d majority spin direction [16]. Therefore, in case of positive I_b, when $\boldsymbol{M}$ points to the y (−y) direction, ferromagnetic detector measures electrochemical potential for spin down (up), as a result, low (high) voltage is observed when $\boldsymbol{M}$ is parallel to the y (−y) direction because measured voltage sign is opposite to the sign of electrochemical potential.

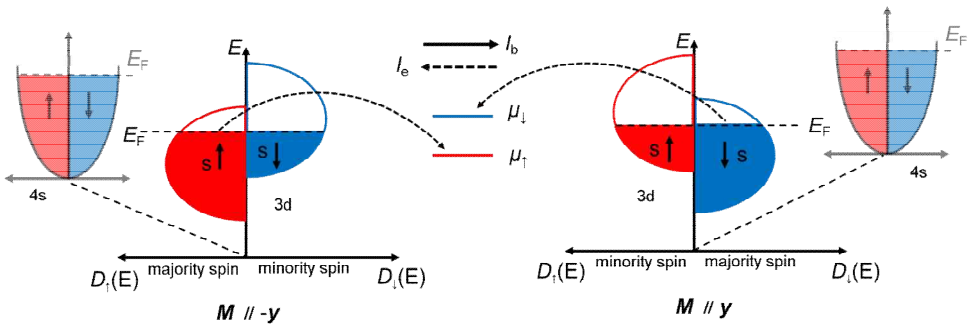

Fig. 2.S1. Schematics for principle of spin-dependent electrochemical potential detection. The schematics express the situation same with the situation of Fig. 2(b).

2.3.2.S2. Magneto-optic Kerr effect (MOKE) for ferromagnetic detector

The magnetic characteristics of the ferromagnetic detector were confirmed by using MOKE [23]. As shown in Fig. 2.S2(a), y-component of magnetization of Py can be measured by detecting elliptically polarized light reflecting from Py layer when linearly polarized light whose spot size is

about 2 μm is focused on Py layer. Kerr signal proportional to y-component of the magnetization is obtained from elliptically polarized light at room temperature while sweeping an external magnetic field in the y axis as shown in Fig. 2.S2(b). Abrupt change of Kerr signal at about ±5 Oe indicates that the direction of the magnetization is switched in the magnetic easy axis by magnetic domain wall motion and this small coercive field is due to thermal assist switching at room temperature. At low temperature, coercive field can increase [24], which can explain ~ 50 Oe coercive field of Fig. 2(b) and (c).

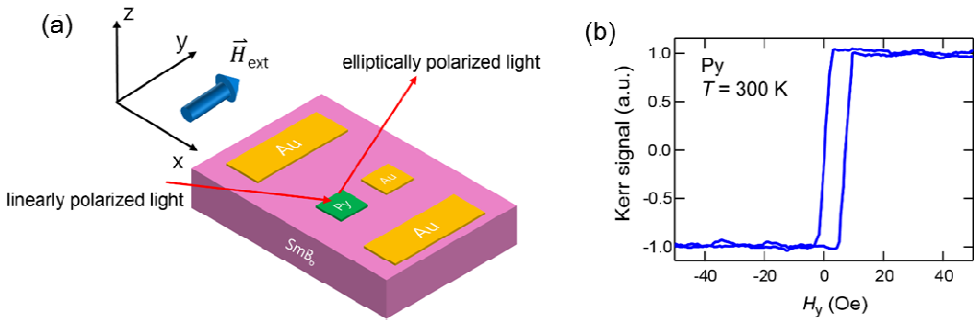

Fig. 2.S2. MOKE signal from ferroamagnet detector (Py). **(a)** Schematic of MOKE measurement. **(b)** Kerr signal with respect to an external magnetic field along the y-direction.

2.3.2.S3. Onsager reciprocal relation

Potentiometric measurement in the main text shows that charge-to-spin conversion occurs in SmB_6 surface channel due to spin-momentum locking property. Conversely, measurement that shows spin-to-charge conversion is also possible using reciprocal measurement geometry [19,25]. As shown in Fig. 2.S3(a), a bias current flows from magnetic contact Py to non-magnetic contact and transverse voltage V_{yx} is measured between non-magnetic contacts positioned along the x-axis while sweeping an external magnetic field along the y-axis. Figure 2.S3(b) shows the measured V_{yx} recorded with I_b of 100 μA which has Onsager reciprocal relation with the result of Fig. 4(b). This result demonstrates that charge-to-spin and spin-to-charge

conversion are reversible each other.

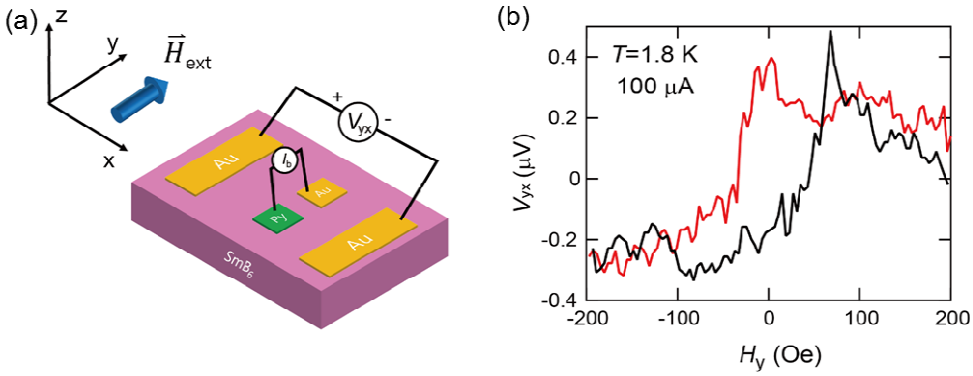

Fig. 2.S3. Reciprocal measurement. **(a)** Schematic of reciprocal measurement. **(b)** V_{yx} measured by sweeping an external magnetic field in the y-axis under I_b of 100 μA at 1.8 K.

2.3.2.S4. Joule heating effect

When current sufficient to cause energy dissipation through Joule heating is applied, thermally activated bulk carriers are generated, eventually, carriers through surface state decline [21]. The local increase in SmB_6 temperature by current was measured using an additional temperature detector near the surface of SmB_6 in Ref. [21]. The Cernox thermometer was used as an additional temperature detector and N greased cigarette paper was placed between the Cernox thermometer and the SmB_6 surface to make sure thermal anchoring and electrical insulation. Thus, because only carriers in surface state have helical spin texture, applying high current can degrade spin voltage signal [16,26]. Figure 2.S4(a) shows 2 point voltage V_{xx} measured by changing I_b, and its differential (Fig. 2.S4(b)) indicates that highly non-linear behavior with I_b exceeding 1 mA. As shown in Fig. 2.S4(c), V_{xy} is measured by sweeping an external magnetic field in the y-axis while applying 1 mA current in the x-axis, which is same measurement configuration with Fig. 2. When 1 mA current is applied, hysteresis loop of V_{xy} shown in Fig. 2 completely disappear, which we attribute to increasing bulk carriers due to local Joule heating by current. The result provides

another evidence that the measured spin voltage in the main text in the linear regime originate from surface dominated conduction.

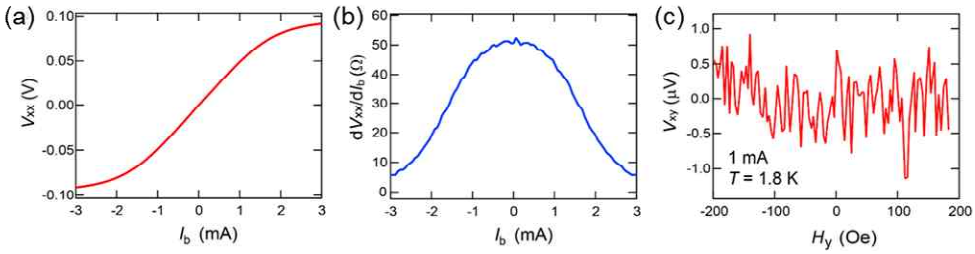

Fig. 2.S4. Joule heating effect on spin voltage. **(a)** 2 point voltage V_{xx} with varying I_b. **(b)** Differential resistance as a function of I_b. **(c)** V_{xy} measured by sweeping an external magnetic field in the y-axis under $|I_b|$ of 1 mA at 1.8 K.

2.3.2.S5. Reproducibility of spin voltage

Same measurement presented in Fig. 2 was carried out in another SmB_6 device. Figure 2.S5(a) (2.S5(b)) shows V_{xy} meaured in another device with applying I_b of +150 μA (−150 μA) at 1.8 K. As discussed in the main text, the non zero the ΔV_{xy} and opposite polarity of hysteresis in Fig. 2.S5(a) and (b) reflects current-induced spin polarization in similarly prepared SmB_6 crystal. The exact magnitude and switching field strongly depends on the detailed condition at SmB_6 /Al_2O_3/Py interface. Nevertheless, the result shows the robustness of spin voltage detection scheme performed in the present manuscript.

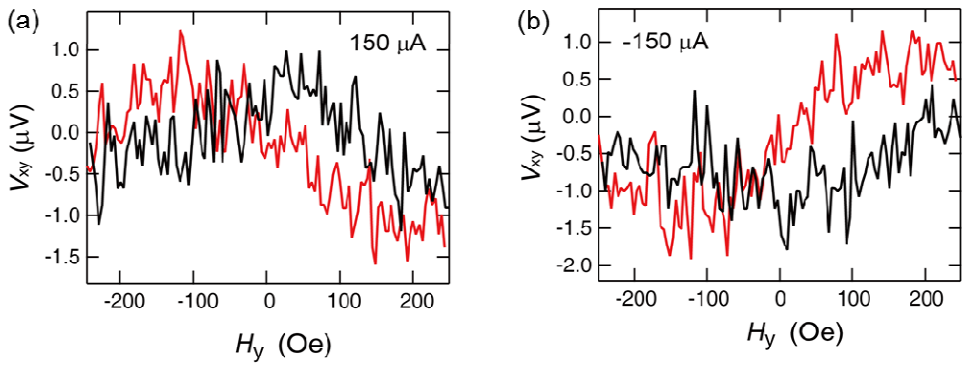

Fig. 2.S5. Spin voltage in similarly prepared SmB_6 device. **(a)**, **(b)** Magnetic field dependence of V_{xy} measured at the ferromagnetic contact under I_b of **(a)**, 150 μA and **(b)**, −150 μA.

2.3.3. Exclusion of possible artifacts

To further confirm the origin of V_{xy}, in particular to exclude the possibility that the hysteresis loops of V_{xy} in Fig. 2 could be due to spurious effects such as the planar Hall effect from the fringe field of the ferromagnetic detector [27], we perform a control experiment by applying $\vec{H}_{ext}$ in the x-direction, where $\boldsymbol{M}$ is orthogonal to $\boldsymbol{p}$. Figures 3(a) and 3(b) show the results of the V_{xy} when applying $\vec{H}_{ext}$ in the y-direction and x-direction, respectively, and the insets show the direction of $\boldsymbol{I}_e$, $\boldsymbol{p}$ and $\boldsymbol{M}$ like shown in Fig. 2(b) and (c). Compared to Fig. 3(a), when the magnetic field is swept in the x-direction, we do not observe the spin chemical potential difference ΔV_{xy} at high positive or negative H_x, reflecting that the measured ΔV_{xy} clearly follows the current-induced spin polarization origin, as $\boldsymbol{p}\cdot\boldsymbol{M}_u$ term in the Eqn. 1 indicates. The intermittent non-zero signal in Fig. 3(b) likely stems from the magnetic domain, whose transient magnetization direction has some y-axis component. The result shows that the measured ΔV_{xy} depends on the projection of the spin polarization onto the detector magnetization direction consistent with the spin-texture model of SmB_6.

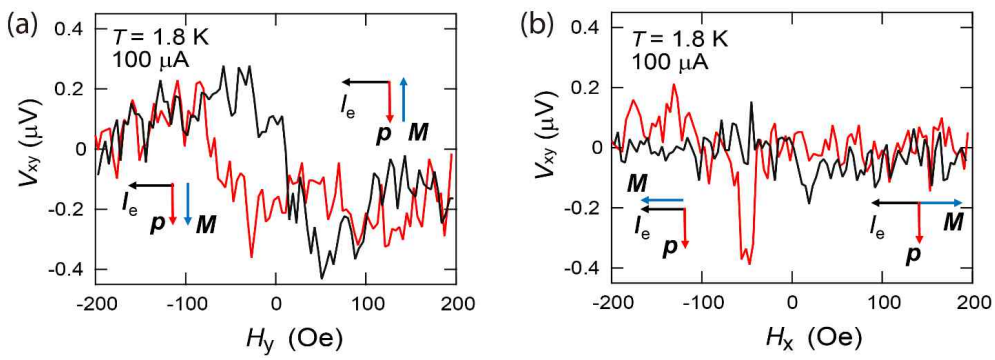

Fig. 3. Magnetization orientation dependence of spin voltage. (a), (b) V_{xy} as a function of an external magnetic field swept (a), in the y-direction, and (b), in the x-direction under I_b of 100 μA at 1.8 K. Inset: black, red and blue arrows show the direction of the electron momentum $\boldsymbol{I}_e$, $\boldsymbol{p}$ and $\boldsymbol{M}$ respectively. Detector

magnetization ***M*** is aligned (a), in the y-direction (perpendicular to current) and (b), in the x-direction (parallel to current).

2.3.4. Temperature dependence of the spin voltage

We now turn to discussing the surface origin of the measured spin voltage. The potentiometric measurement performed at 1.8 K already shows evidence of spin polarization in the surface-dominated transport regime. We further confirm this by investigating the temperature dependence of ΔV_{xy} with the concurrently measured temperature-dependent charge conduction. As shown in Fig. 4(a), the temperature-dependent electrical resistance R(T) of SmB_6 exhibits thermally activated behaviour at intermediate temperatures below 12 K, before saturating at an approximately temperature-independent value below several Kelvin, typically 4 K, strongly supporting the model of the insulating bulk with metallic surface states, as previously probed by other techniques [5,7]. Performed at temperatures ranging from 1.8 to 4.5 K (marked by red dots in Fig. 4(a)), Fig. 4(b)–4(g) show V_{xy} as a function of H_y under $|I_b|$ of 100 μA. Strong temperature dependence is observed with vanishing ΔV_{xy} at ~ 4 K, which closely follows the crossover from surface- to bulk-dominated charge conduction around the same temperature (see the inset to Fig. 4(a)). Moreover, when we consider parallel two channels combined with surface channel resistance independent of temperature and bulk channel resistance dependent on temperature, the ratio between current flowing through surface channel at different temperature is determined by the ratio between total resistance at different temperature. From 1.8 to 4 K, the overall resistance is reduced by 60%, while ΔV_{xy} nearly completely vanishes, which indicates that the additional spin polarization reduction such as spin flip scattering between the surface and bulk conduction channels or spin current cancellation between opposite spin polarization of the surface and bulk spin Hall effect may be important to understand net spin polarization at elevated temperatures. Overall, the results not only

confirm that the measured ΔV_{xy} indeed originates from a surface-dominant effect, but also show that bulk SmB_6 does not exhibit spin–momentum locking.

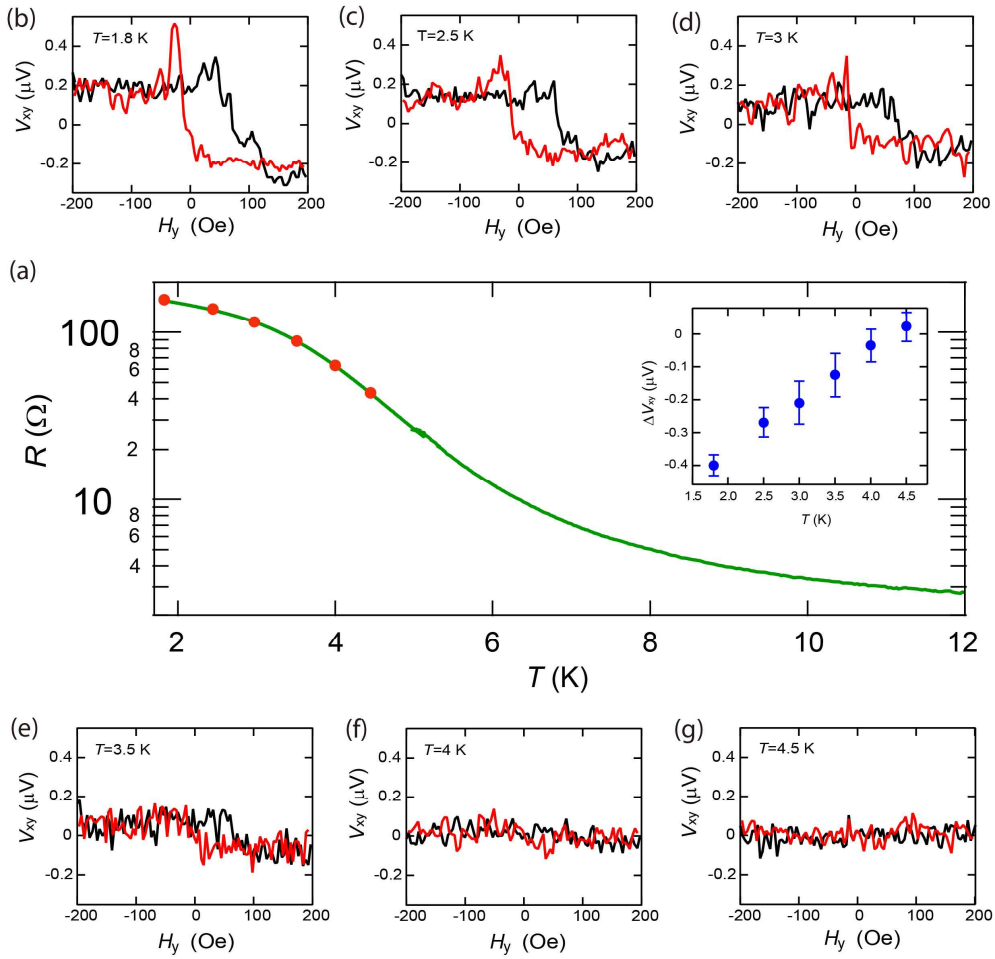

Fig. 4. Temperature dependence of the spin voltage and resistance of SmB_6. (a) Electrical resistance of SmB_6 as a function of temperature. Inset: spin voltage ΔV_{xy} as a function of temperature. (b)-(g) V_{xy} measured by sweeping $\vec{H}_{ext}$ parallel to the y-axis under a bias current of 100 μA at different temperatures, 1.8 K (b), 2.5 K (c), 3 K (d), 3.5 K (e), 4 K (f) and 4.5 K (g).

2.3.5. Magnetic field angle dependence of the spin voltage

The fact that the surface-dominated ΔV_{xy} shows a clear in-plane anisotropy with respect to the directions of I_b and $\boldsymbol{M}$ provides strong

evidence for a spin–momentum locked surface spin polarization in SmB_6. However, the described measurements alone do not distinguish the in-plane vs. out-of-plane nature of the spin polarization in SmB_6. We finally discuss this by showing an angle-resolved spin voltage measurement. We apply 2 T of $|\vec{H}_{ext}|$ to ensure saturation of $\boldsymbol{M}$ to the direction of $\vec{H}_{ext}$ and rotate the field in the y-z plane as shown in Fig. 5(a), where γ is the angle between the direction of $\boldsymbol{M}$ and the y-axis. $|I_b|$ of 300 μA is applied in the +x or −x direction, and γ-dependent V_{xy} is recorded at 2 K. For an accurate spin voltage analysis, the Hall voltage with sin γ dependence (proportional to the z-component of an external magnetic field), as well as higher-order magneto-resistance components were excluded from the raw V_{xy} data (see 2.3.5.S1). Figure 5(b) shows the resulting ΔV_{xy} (γ) in polar coordinates normalized to the maximum spin voltage $\Delta V_{xy,\ max}$. The vanishing spin voltage in the out-of-plane configuration (γ = 90° or 270°), while $\Delta V_{xy,\ max}$ occurs near γ = 0° and 180°, clearly indicates an overall in-plane ensemble spin polarization on the surface of SmB_6 within the experimental error of the field angle calibration of several degrees. We note that the actual angular distribution of ΔV_{xy} in SmB_6 may have a richer structure than a simple cosine function (compare Fig. 5(b), the data and the fit represented by the solid line), which may stem from the non-atomically flat surface morphology of the polished SmB_6 crystal or, possibly, from the combined effects of multiple conduction surface bands in SmB_6. However, more precise determination of ΔV_{xy} (γ) is not possible with the signal-to-noise ratio of the current experiment, and we leave it for the future work.

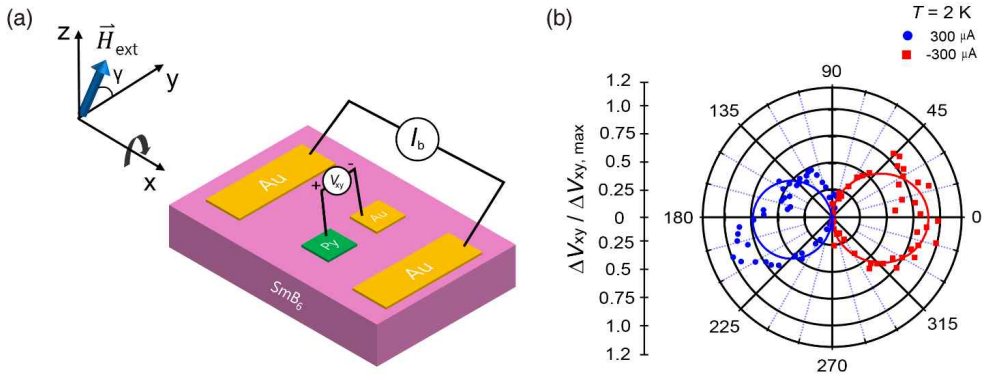

Fig. 5. Angle-resolved current-induced spin polarization. (a) Schematic measurement configuration for potentiometric measurement with rotating magnetic field in the y-z plane, where γ is angle between the applied external magnetic field and the y-axis. (b) Polar plot of normalized ΔV_{xy} as a function of γ showing the in-plane character of the current-induced spin polarization in SmB_6.

2.3.5.S1. Hall voltage and higher order magneto-resistance component removal from angle resolved spin voltage data

To explain the procedure for attaining angle resolved current-induced polarization in Fig. 5(b), raw data for γ angle dependent V_{xy} (γ) is shown in Fig. 5.S1(a), (b) which can be approximately expanded as follow.

$$V_{xy}(\gamma) = \Delta V_{Hall} \sin\gamma + V_{4fold} \cos 4\gamma + V_{spin} \cos\gamma \qquad \text{(S1)}$$

There are three main terms which contribute to V_{xy} (γ) : normal Hall (ΔV_{Hall} sin γ), four fold magneto-resistance (V_{4fold} cos 4γ) and current-induced spin polarization (V_{spin} cos γ) contributions. At first, amplitude of Hall voltage ΔV_{Hall} is determined by difference between V_{xy} at 90° and 270° in Fig. 5.S1(a), (b). After removing Hall voltage from Fig. 5.S1(a), (b), we get results containing both four fold magneto-resistance term with which similar four fold symmetry in measured voltage has been reported previously in SmB_6 [28,29] and current-induced spin polarization term as shown in Fig. 5.S1(c), (d). Using difference in symmetry between cos 4 γ and cos γ terms, we can get spin voltage by using following equation.

$$\Delta V_{xy}(\gamma) = V_{xy}(\gamma) - V_{xy}(\gamma+180^\circ) = 2V_{spin} \cos\gamma \qquad \text{(S2)}$$

In this way, spin voltage $\Delta V_{xy}(\gamma)$ can be obtained as cosine function, which is presented as the solid fit in Fig. 5(b).

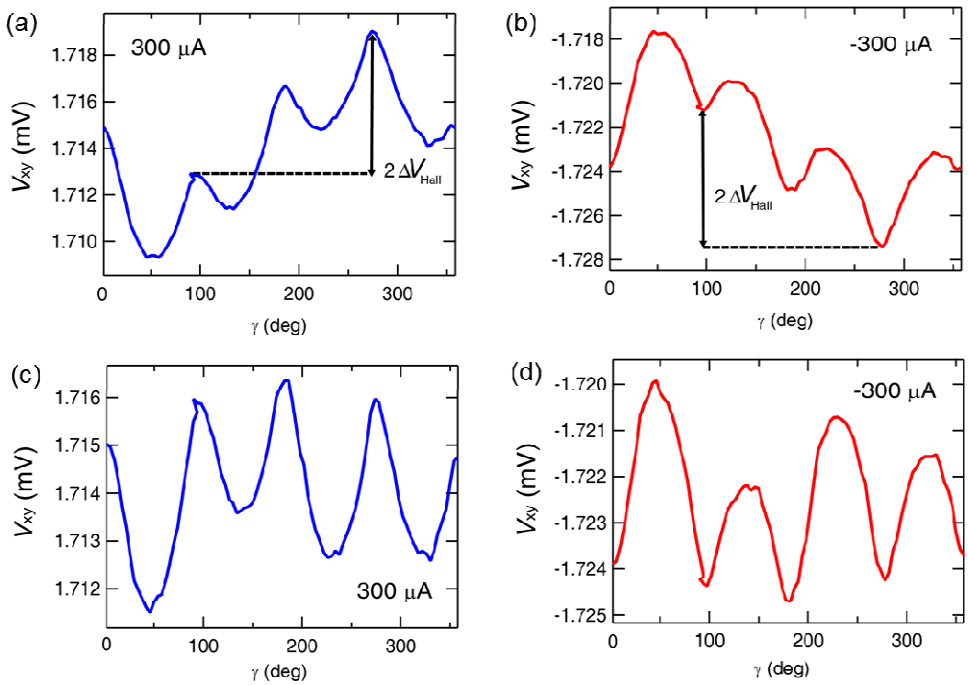

Fig. 5.S1. Raw data for γ angle dependent V_{xy}. **(a)**, **(b)** Raw data for γ angle dependent V_{xy} for I_b of **(a)**, +300 μA and **(b)**, −300 μA along the x-axis. **(c), (d)** γ angle dependent V_{xy} after subtracting normal Hall voltage from **(c)**, Fig. 5.S1(a) and **(d)**, Fig. 5.S1(b).

2.4. Methods

2.4. Methods

2.4.1. Material growth

Single crystals of SmB_6 were grown with Al flux, starting from elemental Sm and B with the stoichiometry of 1 to 6 in a ratio of SmB_6 : Al = 1 : 200–250. The initial materials were placed in an alumina crucible and loaded in a tube furnace under Ar atmosphere. The assembly was heated to 1250–1400 °C and maintained at that temperature for 70–120 hours, then cooled at −2 °C/hr to 600–900 °C, followed by faster cooling. The SmB_6 samples were put into sodium hydroxide to remove the residual Al flux.

2.4.2. Device fabrication

An Al layer of 2 nm was deposited on the polished (100) surface of SmB_6 by using electron beam evaporation followed by oxidizing on a hotplate in ambient conditions (see Supplementary Information S7 and S8). The resulting thin Al oxide layer prevents direct contact of the ferromagnetic electrode with SmB_6. Standard e-beam lithography was used to make electrode patterns. A permalloy (Py) layer was used as a ferromagnetic detector for spin chemical potential measurement, with the lateral size of 150 x 150 μm^2 and thickness of 20 nm deposited and capped with 15 nm of Au using electron beam evaporation. Non-ferromagnetic contacts used for the source, drain and reference electrodes were formed by e-beam lithography patterning and Al oxide etching with a buffered oxide etchant followed by depositing Ti at 5 nm/Au 80 nm using electron beam evaporation. For the Au electrode acting as the wire bonding pad for the ferromagnetic contact, additional insulating layer was made below the metal layer by an overdosing electron beam on electron beam resist (PMMA 950A6) with a dose of 10000 $\mu C/cm^2$ (see the inset to Fig. 1(c)).

2.4.2.S1. Sample preparation and RMS roughness

Raw crystal of SmB_6 shown in the Fig. 2.S1(a) was polished with Al_2O_3 polishing pads whose Al_2O_3 particle size was 50 nm. The polished crystal in the Fig. 2.S1(b) was subsequently dipped into the buffered oxide etchant (BOE) for 20s to remove possible oxide on the surface. The RMS roughness for polished crystal is 904 pm as shown in the Fig. 2.S1(c), which is about four times larger than 250 pm, the RMS roughness of SiO_2, which is often available. Nevetheless, we could detect the spin voltage, which imply that SmB_6 may have a topological surface state protected by time reversal symmety.

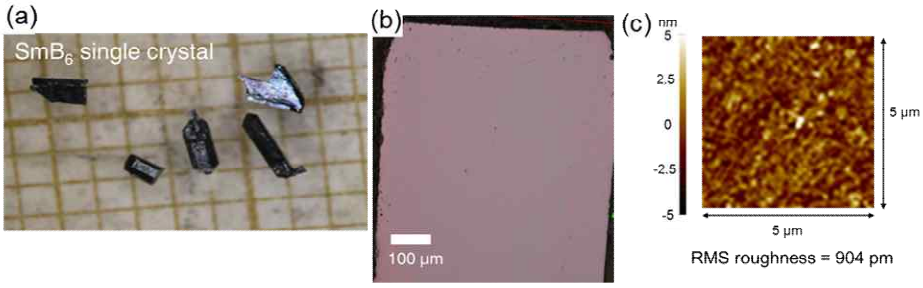

Fig. 2.S1. SmB_6 single crystal and its RMS roughness. **(a)** Raw crystal of SmB_6 without polishing. **(b)** Polished crystal of SmB_6 using Al_2O_3 polishing pads. **(c)** RMS roughness for polished crystal measured by atomic force microscope.

2.4.2.S2. Current-voltage characteristics in Al/Al oxide/Al junction

In order to measure the quality of Al oxide in the main text, Al/Al oxide/Al junction was made. First, the horizontally oriented Al was made to be 30 nm thickness, and then oxidized on a hotplate 150°C for 10 minutes in ambient conditions, which is the same way that the Al oxide of the main text was made. The device was then completed by making the longitudinal Al with 30 nm thickness as shown in the Fig. 2.S2(a). 2 point current-voltage characteristics in Al/Al oxide/Al junction were measured using Keithley 2400 at 1.5 K and 300 K and corresponding results are shown in the Fig. 2.S2(b) and (c), respectively. The current-voltage characteristics exhibit a non-linear behavior, showing typical tunneling transport. As temperature changed from 300 K to 1.5 K, the junction resistance increased by a factor of 6, implying a uniform pinhole free Al oxide.

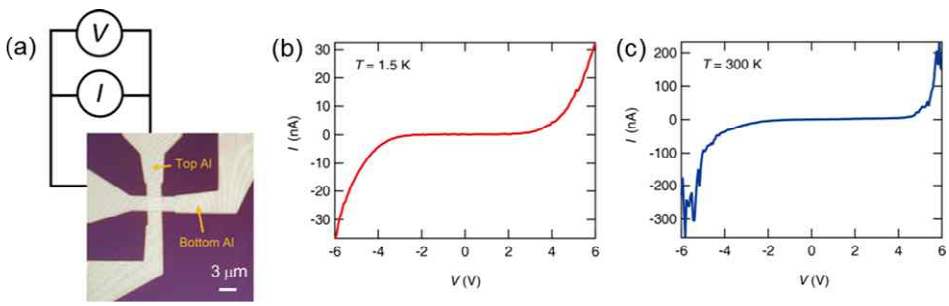

Fig. 2.S2. 2 point measurement in Al/Al oxide/Al junction. **(a)** Schematic of measurement and optical microscope image for Al/Al oxide/Al device. **(b), (c)** Current-voltage characteristics measured at temperature **(b)**, 1.5 K and **(c)**, 300 K.

2.4.3. Transport measurements

The device was placed in a Quantum Design PPMS variable temperature cryostat for low-temperature electrical measurements. For current-induced spin polarization measurement, both DC and AC type four-point probe measurements were performed. A DC (AC) current was applied through the SmB_6 surface channel from the non-magnetic contact source to drain using Keithley 2400 (Keithley 6221) instruments, and a Keithley 2182 nanovoltmeter (Stanford Research Systems SR830 Lock-in amplifier) was used for detecting a voltage difference between the Py and reference Au contact.

2.5. Conclusion

A simple potentiometric geometry with a ferromagnetic contact enables direct electrical measurement of spin chemical potential in the proposed topological Kondo insulator SmB_6. Unlike the situation in conventional topological insulators like Bi_2Se_3 [30,31], the location of the Fermi energy, pinned near the hybridization-induced gap due to the Kondo mechanism, guarantees surface-dominated transport in SmB_6 at low temperatures, thereby allowing clear surface spin voltage measurement even without extrinsic chemical doping [32] or gating technique [33,34] conventionally used for non-ideal topological insulators [31]. The absence of chemical doping or surface gating makes it very likely that the SmB_6 studied here is free from surface band bending related two-dimensional electron gas [35], further confirming that the measured spin voltage mainly stems from the intrinsic surface spin polarization. However, we do not rule out, although it is estimated to be small [18], the possible contribution from the detailed spin textures of the structural-symmetry-broken Rashba surface states, the spin voltage sign of which cannot be distinguished from the topologically protected surface state in the case of SmB_6, as noted earlier, since, unlike

Bi_2Se_3, SmB_6 shows the same anti-clockwise spin texture as that of Rashba surface states in most cases [11,18]. Further systematic study on the in-plane magnetization angle dependence or high-resolution spin-resolved photoemission combined with theoretical calculation is needed to fully separate the topologically nontrivial and trivial spin polarization contributions. Nevertheless, with the ability to clearly measure the intrinsic, surface-dominated spin polarization in strongly correlated systems, this approach provides potential for both fundamental and applied spin transport studies in newly proposed topologically nontrivial states of matter.

2.5.S1. Comparision of current-induced spin polarization with other spin-to-charge conversion factor

SmB_6 has anti-clockwise spin texture for the surface state as shown in Fig. 1(a). Due to this anti-clockwise spin texture, $\boldsymbol{p}$ of SmB_6 is opposite to that of Bi_2Se_3, conventional topological insulator. This fact is consistent with our current-induced spin polarization analysis in the paragraph corresponding to Fig. 2 and is also consistent with the negative spin Hall angle of SmB_6 confirmed by spin orbit torque measurement [36]. The magnitude of $\boldsymbol{p}$ also can be compared with other spin-to- charge conversion factor such as inverse Rashba Edelstein effect length or spin Hall angle. First of all, inverse Rashba Edelstein effect (IREE) length, λ_{IREE}, can be obtained using following equation [19] to compare with the spin Hall angle, θ_{SHE}.

$$j_c = \lambda_{IREE} j_s, \ \lambda_{IREE} = \frac{p\lambda}{\pi} \tag{S3}$$

In spin-momentum locked surface, charge current density in A m^{-1}, j_c, and spin current density in A m^{-2}, j_s, are connected through λ_{IREE} that is proportional to spin polarization, $\boldsymbol{p}$, and mean free path, λ. In SmB_6, because β band electrons mainly contribute on surface conduction, λ for β band (55 nm) can be used to obtain λ_{IREE} [37]. In our case, λ_{IREE} is 2.63 nm, which is one order larger than λ_{IREE} in Bi_2Se_3, typical topological insulator. Although spin Hall effect (SHE) occurs in 3D bulk heavy metal, we can try to assume

very thin surface layer in which SHE occurs to convert λ_{IREE} to θ_{SHE}. When the interface layer thickness, t, is less than spin diffusion length, θ_{SHE} can be expressed as [38]

$$j_c = \frac{1}{2}\theta_{SHE} t j_s \tag{S4}$$

If we assume the surface layer thickness is 0.4 nm, we can get θ_{SHE} of 13.15 from $\frac{1}{2}\theta_{SHE} t = \lambda_{IREE}$, implying that there exist strong interfacial effect by topological surface state.

2.6. References

[1] M. Dzero, K. Sun, V. Galitski, and P. Coleman, *Topological Kondo Insulators*, Phys. Rev. Lett. **104,** 106408 (2010).

[2] R. Yu, H. M. Weng, X. Hu, Z. Fang, and X. Dai, *Model Hamiltonian for topological Kondo insulator SmB_6*, New J. Phys. **17,** 023012 (2015).

[3] T. Takimoto, *SmB_6: A Promising Candidate for a Topological Insulator*, J. Phys. Soc. Jpn. **80,** 123710 (2011).

[4] R. Yu, H. M. Weng, Z. Fang, and X. Dai, *Pseudospin, real spin, and spin polarization of photoemitted electrons*, Phys. Rev. B **94,** 085123 (2016).

[5] P. Syers, D. Kim, M. S. Fuhrer, and J. Paglione, *Tuning Bulk and Surface Conduction in the Proposed Topological Kondo Insulator SmB_6*, Phys. Rev. Lett. **114,** 096601 (2015).

[6] S. Wolgast, C. Kurdak, K. Sun, J. W. Allen, D. J. Kim, and Z. Fisk, *Low-temperature surface conduction in the Kondo insulator SmB_6*, Phys. Rev. B **88,** 180405 (2013).

[7] D. J. Kim, S. Thomas, T. Grant, J. Botimer, Z. Fisk, and J. Xia, *Surface Hall Effect and Nonlocal Transport in SmB_6: Evidence for Surface Conduction*, Sci. Rep. **3,** 3150 (2013).

[8] M. Neupane *et al.*, *Surface electronic structure of the topological Kondo-insulator candidate correlated electron system SmB_6*, Nat. Commun. **4,** 2991 (2013).

[9] Y. Nakajima, P. Syers, X. F. Wang, R. X. Wang, and J. Paglione, *One-dimensional edge state transport in a topological Kondo insulator*, Nat. Phys. **12,** 213 (2016).

[10] D. J. Kim, J. Xia, and Z. Fisk, *Topological surface state in the Kondo insulator samarium hexaboride*, Nat. Mater. **13,** 466 (2014).

[11] N. Xu *et al.*, *Direct observation of the spin texture in SmB_6 as evidence of the topological Kondo insulator*, Nat. Commun. **5,** 4566 (2014).

[12] Q. Song *et al.*, *Spin injection and inverse Edelstein effect in the surface states of topological Kondo insulator SmB_6*, Nat. Commun. **7,** 13485 (2016).

[13] J. Jiang *et al.*, *Observation of possible topological in-gap surface states in the Kondo insulator SmB_6 by photoemission*, Nat. Commun. **4,** 3010 (2013).

[14] C. H. Li, O. M. J. van 't Erve, J. T. Robinson, Y. Liu, L. Li, and B. T. Jonker, *Electrical detection of charge-current-induced spin polarization due to spin-momentum locking in Bi_2Se_3*, Nat. Nanotech. **9,** 218 (2014).

[15] A. Dankert, J. Geurs, M. V. Kamalakar, S. Charpentier, and S. P. Dash, *Room Temperature Electrical Detection of Spin Polarized Currents in Topological Insulators*, Nano Lett. **15,** 7976 (2015).

[16] J. F. Tian, I. Miotkowski, S. Hong, and Y. P. Chen, *Electrical injection and*

detection of spin-polarized currents in topological insulator Bi_2Te_2Se, Sci. Rep. **5,** 14293 (2015).
[17] Y. Xia *et al.*, *Observation of a large-gap topological-insulator class with a single Dirac cone on the surface*, Nat. Phys. **5,** 398 (2009).
[18] S. Hong, V. Diep, S. Datta, and Y. P. Chen, *Modeling potentiometric measurements in topological insulators including parallel channels*, Phys. Rev. B **86,** 085131 (2012).
[19] S. Sayed, S. Hong, and S. Datta, *Multi-Terminal Spin Valve on Channels with Spin-Momentum Locking*, Sci. Rep. **6,** 35658 (2016).
[20] C. H. Li, O. M. J. van 't Erve, S. Rajput, L. Li, and B. T. Jonker, *Direct comparison of current-induced spin polarization in topological insulator Bi_2Se_3 and InAs Rashba states*, Nat. Commun. **7,** 13518 (2016).
[21] D. J. Kim, T. Grant, and Z. Fisk, *Limit Cycle and Anomalous Capacitance in the Kondo Insulator SmB_6*, Phys. Rev. Lett. **109,** 096601 (2012).
[22] E. Villamor, M. Isasa, L. E. Hueso, and F. Casanova, *Temperature dependence of spin polarization in ferromagnetic metals using lateral spin valves*, Phys. Rev. B **88,** 184411 (2013).
[23] C. Daboo *et al.*, *ANISOTROPY AND ORIENTATIONAL DEPENDENCE OF MAGNETIZATION REVERSAL PROCESSES IN EPITAXIAL FERROMAGNETIC THIN-FILMS*, Phys. Rev. B **51,** 15964 (1995).
[24] W. C. Nunes, W. S. D. Folly, J. P. Sinnecker, and M. A. Novak, *Temperature dependence of the coercive field in single-domain particle systems*, Phys. Rev. B **70,** 014419 (2004).
[25] L. Q. Liu, A. Richardella, I. Garate, Y. Zhu, N. Samarth, and C. T. Chen, *Spin-polarized tunneling study of spin-momentum locking in topological insulators*, Phys. Rev. B **91,** 235437 (2015).
[26] P. K. Li and I. Appelbaum, *Interpreting current-induced spin polarization in topological insulator surface states*, Phys. Rev. B **93,** 220404(R) (2016).
[27] E. K. de Vries, A. M. Kamerbeek, N. Koirala, M. Brahlek, M. Salehi, S. Oh, B. J. van Wees, and T. Banerjee, *Towards the understanding of the origin of charge-current-induced spin voltage signals in the topological insulator Bi_2Se_3*, Phys. Rev. B **92,** 201102(R) (2015).
[28] Z. J. Yue, X. L. Wang, D. L. Wang, J. Y. Wang, D. Culcer, and S. X. Dou, *Crossover of Magnetoresistance from Fourfold to Twofold Symmetry in SmB6 Single Crystal, a Topological Kondo Insulator*, J. Phys. Soc. Jpn. **84,** 044717 (2015).
[29] F. Chen *et al.*, *Magnetoresistance evidence of a surface state and a field-dependent insulating state in the Kondo insulator SmB6*, Phys. Rev. B **91,** 205133 (2015).
[30] D. Hsieh *et al.*, *A tunable topological insulator in the spin helical Dirac transport regime*, Nature **460,** 1101 (2009).
[31] D. S. Kong *et al.*, *Rapid Surface Oxidation as a Source of Surface Degradation Factor for Bi_2Se_3*, ACS Nano **5,** 4698 (2011).
[32] D. Kim, S. Cho, N. P. Butch, P. Syers, K. Kirshenbaum, S. Adam, J. Paglione, and M. S. Fuhrer, *Surface conduction of topological Dirac electrons in bulk insulating Bi_2Se_3*, Nat. Phys. **8,** 459 (2012).
[33] J. F. Tian, S. M. Hong, I. Miotkowski, S. Datta, and Y. P. Chen, *Observation of current-induced, long-lived persistent spin polarization in a topological insulator: A rechargeable spin battery*, Sci. Adv. **3,** e1602531 (2017).
[34] J. S. Lee, A. Richardella, D. R. Hickey, K. A. Mkhoyan, and N. Samarth, *Mapping the chemical potential dependence of current-induced spin polarization in a topological insulator*, Phys. Rev. B **92,** 155312 (2015).
[35] M. Bianchi, D. D. Guan, S. N. Bao, J. L. Mi, B. B. Iversen, P. D. C. King, and P. Hofmann, *Coexistence of the topological state and a two-dimensional electron gas on the surface of Bi_2Se_3*, Nat. Commun. **1,** 128 (2010).
[36] Y. F. Li, Q. L. Ma, S. X. Huang, and C. L. Chien, *Thin films of topological Kondo*

insulator candidate SmB6: Strong spin-orbit torque without exclusive surface conduction, Sci. Adv. **4,** (2018).
[37] G. Li *et al.*, *Two-dimensional Fermi surfaces in Kondo insulator SmB6*, Science **346,** 1208 (2014).
[38] J. C. Rojas Sanchez, L. Vila, G. Desfonds, S. Gambarelli, J. P. Attane, J. M. De Teresa, C. Magen, and A. Fert, *Spin-to-charge conversion using Rashba coupling at the interface between non-magnetic materials*, Nat. Commun. **4,** (2013).

Chapter 3. Electrical detection of the inverse Edelstein effect on the surface of SmB_6

Jehyun Kim[1†], Chaun Jang[2†], Xiangfeng Wang[3], Johnpierre Paglione[3], Seokmin Hong[2], Shehrin Sayed[4], Dongwon Chun[5] and Dohun Kim[1*]

[1]*Department of Physics and Astronomy, and Institute of Applied Physics, Seoul National University, Seoul 08826, Korea*

[2]*Center for Spintronics, Korea Institute of Science and Technology, Seoul 02792, Korea*

[3]*Maryland Quantum Materials Center, Department of Physics, University of Maryland, College Park, MD 20742, USA*

[4]*Electrical Engineering and Computer Science, University of California, Berkeley, California 94720, USA*

[5]*Advanced Analysis Center, Korea Institute of Science and Technology, Seoul 02792, Korea*

[†]*These authors contributed equally to this work.*

**Corresponding author: dohunkim@snu.ac.kr*

This work was published in "Physical Review B"

3.1. Abstract

We report the measurement of spin current-induced charge accumulation, the inverse Edelstein effect (IEE), on the surface of single-crystal candidate topological Kondo insulator SmB_6. The robust surface conduction channel of SmB_6 has been shown to exhibit a large degree of spin-momentum locking, and the spin-polarized current through an external ferromagnetic contact induces spin-dependent charge accumulation on the surface of SmB_6. The dependence of the IEE signal on the bias current, an external magnetic field direction, and temperature are consistent with an anticlockwise spin texture of the SmB_6 surface band in momentum space. The direction and magnitude of this effect, compared with the normal Edelstein signal, are

clearly explained by the Onsager reciprocal relation. Furthermore, we estimate the spin-to-charge conversion efficiency, i.e., the IEE length, to be 4.46 nm, which is an order of magnitude larger than the efficiency found in other typical Rashba interfaces, implying that the Rashba contribution to the IEE signal may be small. Building upon existing reports on the surface charge and spin conduction nature of this material, our results provide additional evidence that the surface of SmB_6 supports a spin-polarized conduction channel.

3.2. Introduction

Three-dimensional (3D) topological insulators (TIs) are a newly developed class of insulators with a bulk band gap in which time-reversal symmetry-protected metallic surface states reside. The spin-momentum locking exhibited by the surface conduction channels make TIs a promising platform for exploring new physics such as Majorana quasi-particle states, and for applications in various spintronic devices [1-3]. However, in conventional 3D TIs, the Fermi level naturally resides in the bulk conduction or valence bands owing to unintentional doping, resulting in the hindrance of surface-driven phenomena by bulk carriers [4-6]. Recently, SmB_6, a Kondo insulator, has been predicted to be a member of a newly classified family of strong TIs, topological Kondo insulators (TKIs), in which the topologically protected surface states reside in the bulk Kondo band gap at low temperatures and the Fermi level is guaranteed to be inside the bulk gap [7-9]. A large degree of current-induced spin polarization on the surface of SmB_6 as well as robust surface conduction have been demonstrated in various experiments [10-19], implying that SmB_6 is a strong candidate for TKIs free from bulk effects.

Here, we report an additional demonstration that the surface of SmB_6 indeed exhibits transport phenomena consistent with a spin-momentum locked spin texture through observation of the spin current-induced charge

accumulation, the inverse Edelstein effect (IEE). Distinct from a previous spin injection experiment using microwave-induced spin pumping on the surface of SmB_6 [11], we use a near-DC electrical method to generate charge accumulation through the IEE. Charge accumulation can be generated not only by injecting spin-polarized current generated using a ferromagnetic metal into the surface of SmB_6, but also by extraction of the spin-polarized current generated from the surface of SmB_6. The resultant charge accumulation is measured as the voltage difference between two nonmagnetic contacts on the surface. The measured dependence of the charge accumulation on the direction and magnitude of the bias current, the external magnetic field direction, and the temperature are all consistent with the spin-momentum locking of the SmB_6 surface state.

3.3. Results

3.3.1. Principle of electrical measurement for IEE

The Edelstein effect is one of the well-known effects involving charge-to-spin conversion intimately related to the spin Hall effect. In materials with spin-momentum locking, the flow of a charge current produces non-equilibrium spin polarization through the Edelstein effect [20]. The Onsager reciprocal effect of the Edelstein effect is called the IEE, where a non-equilibrium spin accumulation in a two-dimensional electron gas generates charge accumulation perpendicular to its spin direction [21,22].

To detect the charge accumulation on the surface of SmB_6 arising from the IEE, a Py layer is used as a spin source to induce non-equilibrium spin accumulation on the SmB_6 surface. Figure 1(a) shows the electrical measurement configuration for the IEE, where a bias current I_b flows through Py on the SmB_6 parallel to the y axis, and the transverse voltage difference V_{yx}, defined as $V_+ - V_-$, is measured between two nonmagnetic Au contacts positioned at the ends of SmB_6 on the x axis while sweeping an external magnetic field along the y axis. The measured V_{yx} can be classified

into four cases according to the directions of I_b and the Py magnetization ($\boldsymbol{M}$).

Figures 1(b) – (e) show schematic top views of the device illustrated in Fig. 1(a), and the charge accumulation along the x axis due to the IEE where the accumulated spin-up (spin-down) electrons are depicted with red (blue) arrows parallel (anti-parallel) to the +y direction and the direction of the accumulation is shown by the grey arrows pointing to the Au voltage probes. We note that the same amount of electrons with spin anti-parallel to the accumulated spin, in a steady state, must flow in the direction toward the center of the device owing to the zero net current along the x axis in an open circuit condition. Moreover, because the direction of the Py majority spin is opposite to that of its magnetization and the majority spin of Py is mainly coupled to the SmB_6 surface channel, the contact resistance between Py and the spin-up channel of SmB_6 is larger (smaller) than that between Py and the spin-down channel of SmB_6 for $\boldsymbol{M}$ parallel to the +y (-y) direction [23,24].

In the case of injection (I_b parallel to the -y direction) in which spin-polarized electrons are injected into the surface of SmB_6, for $\boldsymbol{M}$ parallel to the +y (-y) direction, more spin-down (spin-up) electrons are accumulated on the surface of SmB_6. The accumulated electrons subsequently have net momentum in the -x (+x) direction due to the spin-momentum locking, resulting in a higher electrochemical potential at the left (right) side and, eventually, $V_{yx} < (>) 0$. On the other hand, for extraction (I_b parallel to the +y direction), where the spin-polarized electrons from SmB_6 are extracted and tunnel into Py, for $\boldsymbol{M}$ parallel to the +y (-y) direction, more spin-up (spin-down) electrons are left behind on the surface of SmB_6 owing to the high contact resistance. These electrons subsequently have net momentum in the +x (-x) direction due to the spin-momentum locking, resulting in a higher electrochemical potential at the right (left) side and, eventually, $V_{yx} > (<) 0$. We confirmed the non-zero V_{yx} induced by spin current injection/extraction using a simulation based on the semi-classical model for

charge and spin transport (see 3.3.1.S1). In summary, the expected behaviors of V_{yx} as functions of the external magnetic field H_y for injection and extraction are described in Fig. 1(f) and 1(g), respectively, where H_c is the switching field of Py and the IEE signal ΔV_{yx}, defined as V_{yx} (***M*** // +y) – V_{yx} (***M*** // -y), is negative (positive) for injection (extraction). We also define the polarities of the hysteresis loops in Fig. 1(f) and 1(g) as negative and positive, respectively.

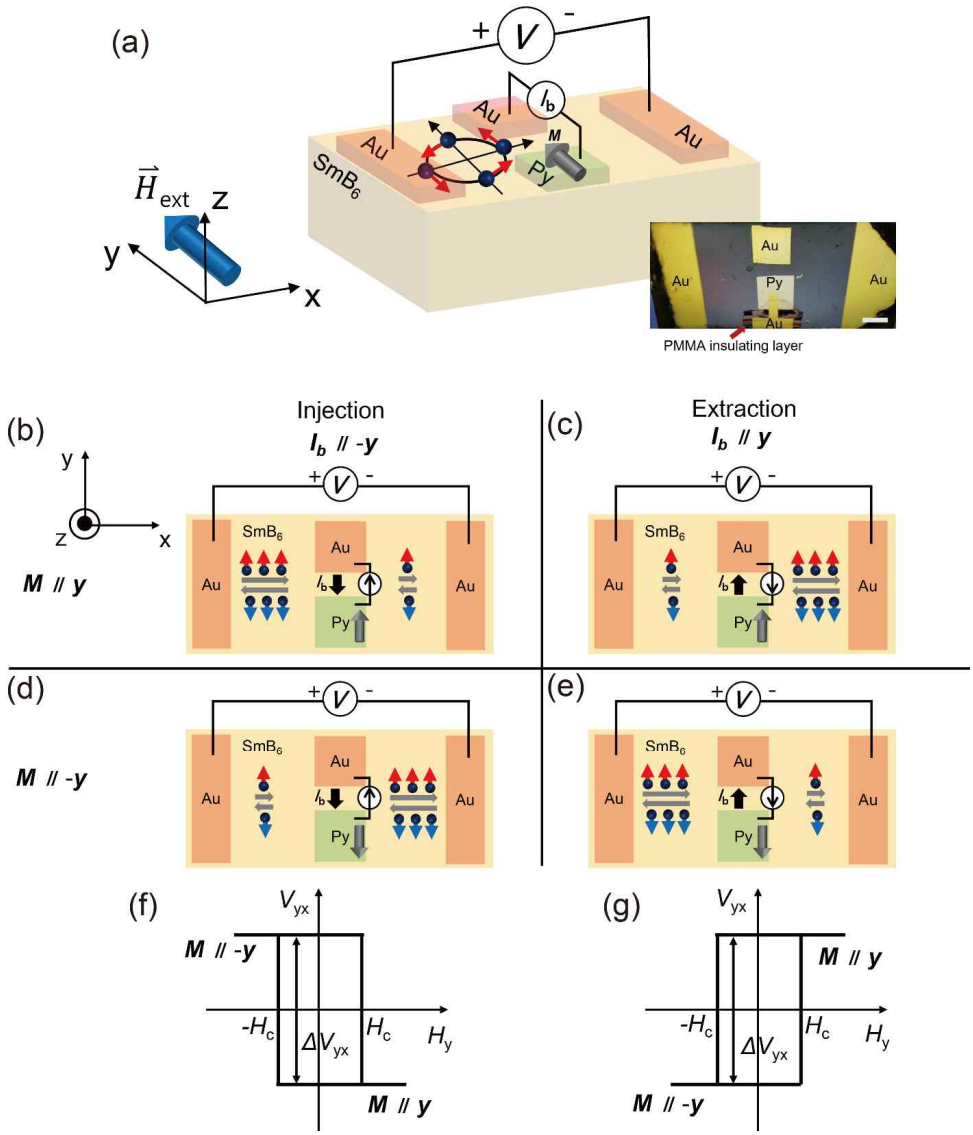

Fig. 1. Principle of electrical measurement of the Inverse Edelstein Effect (IEE). (a) Schematic of the measurement setup and anticlockwise spin texture of the surface band in SmB_6 near the Fermi energy. Inset: Optical microscope image of the device. The length of the white scale bar is 100 μm. (b) – (e) Schematic top views of the charge accumulation due to the IEE in the cases of ***M*** // +***y*** under injection (b), ***M*** // +***y*** under extraction (c), ***M*** // -***y*** under injection (d), and ***M*** // -***y*** under extraction (e). The grey arrows represent the direction in which electrons with spin-up or spin-down move. (f), (g) The expected inverse Edelstein signals for spin injection (f) and extraction (g).

3.3.1.S1. Simulation results of spin current injection/extraction onto SmB_6 based on the semi-classical model

For the given structure of Fig. 1, the current injection/extraction contacts of Py and Au can be considered as spin current injection/extraction contacts due to Py depending on the magnetization directions. Here we use the semi-classical model for charge and spin transport that was previously proposed and experimentally verified [23] to understand the present structure. As shown in Fig. 1.S1 the spin current is injected/extracted from the point contact in the middle and the charge voltage induced by the spin current develops across the x-direction. Due to spin-momentum locking in SmB_6 the injected spin current tends to move preferentially right or left directions, which eventually cancelled out by oppositely moving electrons with opposite spin directions satisfying no net charge current condition.

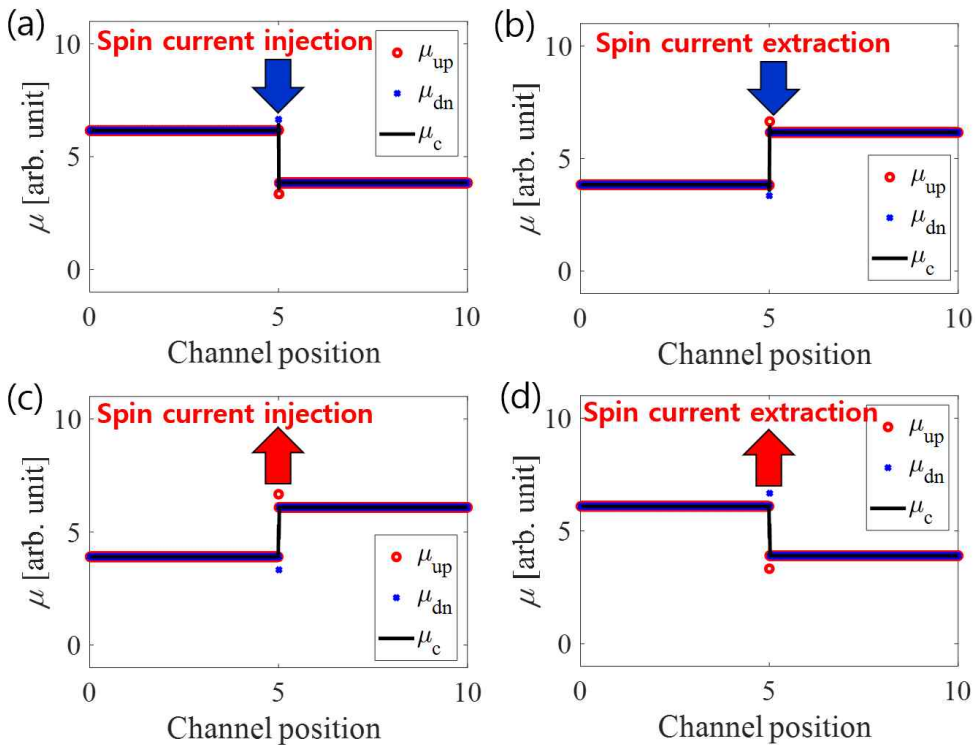

Fig. 1.S1. Simulation results of spin current injection/extraction onto SmB_6 based on the semiclassical model [23]. (a)-(d) Electrochemical potential μ_c for spin-up μ_{up} and spin-down μ_{dn} as a function of SmB_6 surface channel position along the x axis. Spin current are injected or extracted from a point contact in the middle of the sample with arrows representing the spin direction of electrons from the ferromagnetic spin source (red arrows for spin-up and blue arrows for spin-down).

3.3.2. Electrical measurement of the IEE signal

We first report the expected behavior of the aforementioned IEE signal on the surface of SmB_6, which is reflected in a non-zero ΔV_{yx}. As shown in Fig. 2(a), V_{yx} is measured by sweeping an external magnetic field along the y axis to control the magnetization direction of Py while applying I_b along the y axis. Figures 2(b) and 2(c) show representative V_{yx} values as functions of H_y recorded with I_b of +150 μA and −150 μA, respectively, at 1.8 K. For I_b of +150 μA (−150 μA), the spin extraction (injection) results in a

hysteresis loop with a positive (negative) polarity in agreement with our expectation, which is clearly consistent with the anticlockwise spin-momentum relation in SmB_6 (see 3.3.2.S1). The ΔV_{yx} extracted from the hysteresis loops under different I_b values exhibits a linear response to I_b, as shown in Fig. 2(d), implying that the current-induced spin injection and extraction lead to a non-zero ΔV_{yx}.

The IEE signal can also be analyzed quantitatively using the Onsager reciprocal relation. The Onsager reciprocal relation is a universal relation for any setup in the linear response regime. It states that the ratio of the measured voltage to the bias current does not change even when the voltage and current terminals are exchanged [24,25]. However, when a time-reversal symmetry breaking field such as $\boldsymbol{M}$ is present, the sign of the field should be reversed in the reciprocity relation. Thus, the Onsager reciprocal relation is given by

$$\frac{V_{12}(\boldsymbol{M})}{I_{34}} = \frac{V_{34}(-\boldsymbol{M})}{I_{12}}, \tag{1}$$

where V_{ab} is defined as $V_a - V_b$ and I_{cd} denotes the current that flows from terminal c to terminal d.

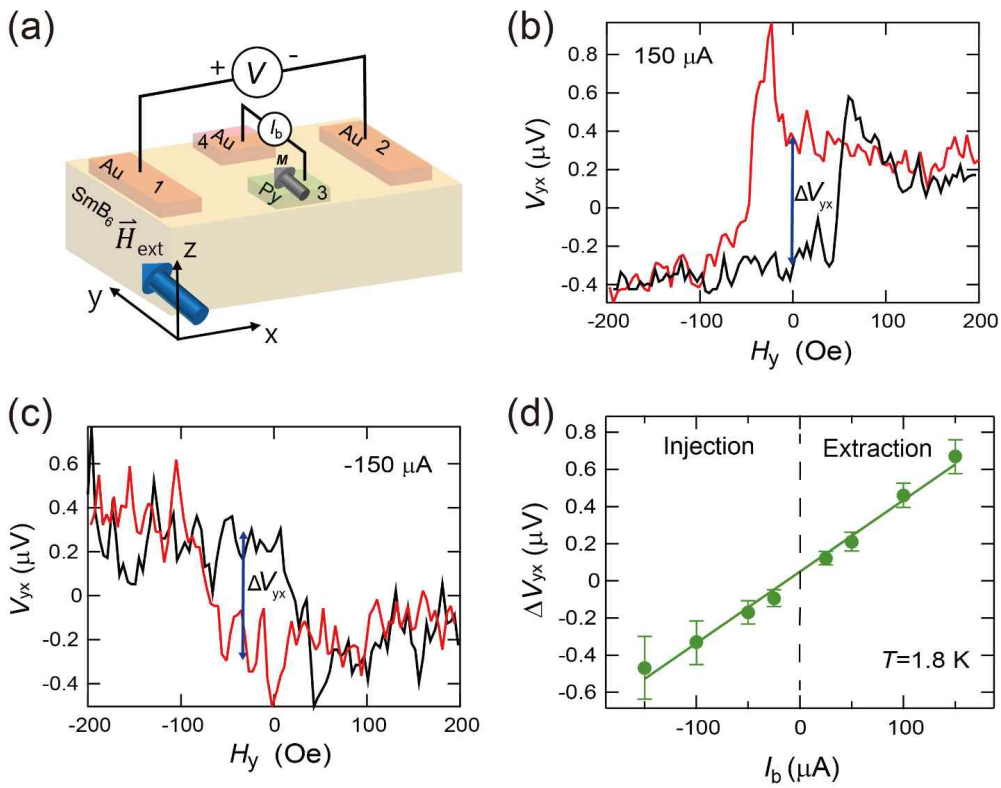

Fig. 2. Electrical measurement of the IEE signal. (a) Schematic of the electrical measurement configuration. A bias current I_b is applied along the y axis, and the voltage difference is measured between two Au contacts while sweeping a magnetic field along the y axis. (b), (c) The measured V_{yx} as a function of the y component of an external magnetic field H_y for I_b of +150 μA (b) and −150 μA (c). (d) Dependence of the IEE signal ΔV_{yx} as a function of I_b measured at 1.8 K.

3.3.2.S1. Anisotropic magnetoresistance (AMR) for ferromagnetic spin source

The magnetic characteristics of the ferromagnetic spin source (Py) can be confirmed by observing AMR signal [26,27]. Py with 20 nm thickness is deposited on SmB_6 crystal to measure AMR at different temperature. We performed 2 point measurement using the same coordinate system as the main text part and voltage difference between different two contacts was

measured while sweeping an external magnetic field in the y direction under a constant bias current 300 μA along the x direction. As shown in Fig. 2.S1, clear AMR signal is observed and it is found that the coercive field of Py layer is about 35 Oe which is almost the same value with the switching field of hysteresis loop in Fig. 2(b) and 2(c). As the temperature increases, the magnitude of AMR decreases and then disappears at 7K, which means current flowing through Py layer diminishes due to activation of bulk channel of SmB_6 with temperature increasing. The result shows clear identification of the coercive field of the Py film by transport measurement and surface-dominated transport property of SmB_6 at low temperature.

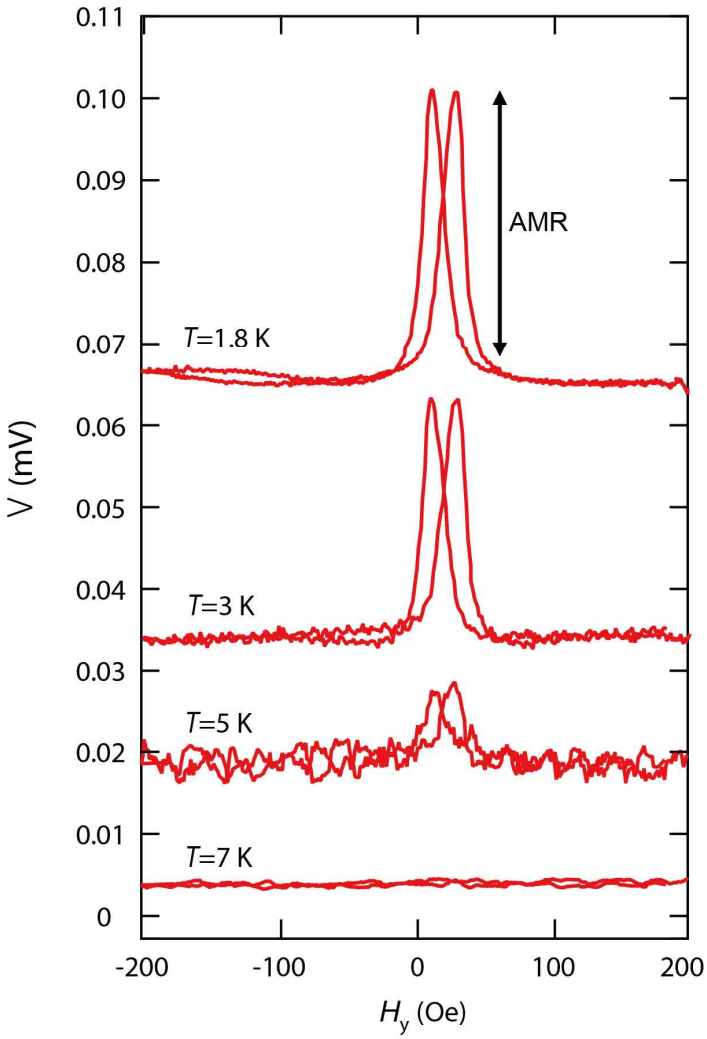

Fig. 2.S1. Temperature dependent AMR of thin Py film deposited on SmB_6 crystal.

3.3.3. Onsager reciprocal relation

Figure 3 clearly exhibits the Onsager reciprocal relation expressed by Eq. (1) between the potentiometric spin measurement, where the ferromagnetic metal is used as the spin detector, and its reciprocal measurement for the IEE, where SmB_6 is used as the spin detector. Figures 3(a) and 3(c) respectively show a schematic drawing of the potentiometric spin measurement and the corresponding V_{34} recorded with I_{12} of 100 μA at 1.8 K while sweeping an external magnetic field along the y axis. Figures 3(b) and 3(d) respectively show a schematic drawing of the IEE measurement and the corresponding V_{12} recorded with I_{34} of 100 μA at 1.8 K while sweeping an external magnetic field along the y axis. The results show a hysteresis loop with negative polarity for the potentiometric measurement and a loop with positive polarity for the IEE measurement consistent with the Onsager reciprocal relation Eq. (1). More specifically, in the potentiometric spin measurement, the spin voltage ΔV_{34} can be expressed as [28]

$$\frac{\Delta V_{34}}{I_{12}} = \frac{V_{34}(\boldsymbol{M}) - V_{34}(-\boldsymbol{M})}{I_{12}} = R_{\mathrm{B}} P_{\mathrm{FM}} (\boldsymbol{p} \bullet \boldsymbol{M}_{\mathbf{u}}), \tag{2}$$

where ΔV_{34} is the reciprocal value of ΔV_{12} in this study. ΔV_{34} is proportional to the bias current I_{12}, ballistic channel resistance R_{B}, ferromagnetic metal spin polarization P_{FM}, and the inner product between the surface channel spin polarization $\boldsymbol{p}$ under a positive bias current and the unit vector along the ferromagnetic metal magnetization $\boldsymbol{M}_{\mathrm{u}}$. Eq. (1) and Eq. (2) can be combined to yield

$$\frac{\Delta V_{12}}{I_{34}} = \frac{V_{12}(\boldsymbol{M}) - V_{12}(-\boldsymbol{M})}{I_{34}} = -R_{\mathrm{B}} P_{\mathrm{FM}} (\boldsymbol{p} \bullet \boldsymbol{M}_{\mathbf{u}}), \tag{3}$$

where the negative sign is due to the Onsager reciprocal relation. As expected in Eq. (3), the slope from the linear fitting shown in Fig. 2(d) has an opposite sign to that of the bias current dependence of the spin voltage

[19,29]. Furthermore, the magnitude of the slope in Fig. 2(d) is 2.7 mΩ, which is slightly larger than the 2.3 mΩ previously reported for a potentiometric geometry experiment [19]. This difference can be attributed to the non-linearity of the contact resistance between the ferromagnetic metal and SmB_6. As the IEE signal follows the Onsager reciprocal relation, we estimate $|\boldsymbol{p}|$ of SmB_6 to be 27% from both the inverse and normal Edelstein effect results (see 3.3.3.S1). Therefore, the IEE signal ΔV_{12} electrically measured through both spin injection and extraction supports the conclusion that SmB_6 indeed has an anticlockwise surface spin texture in momentum space.

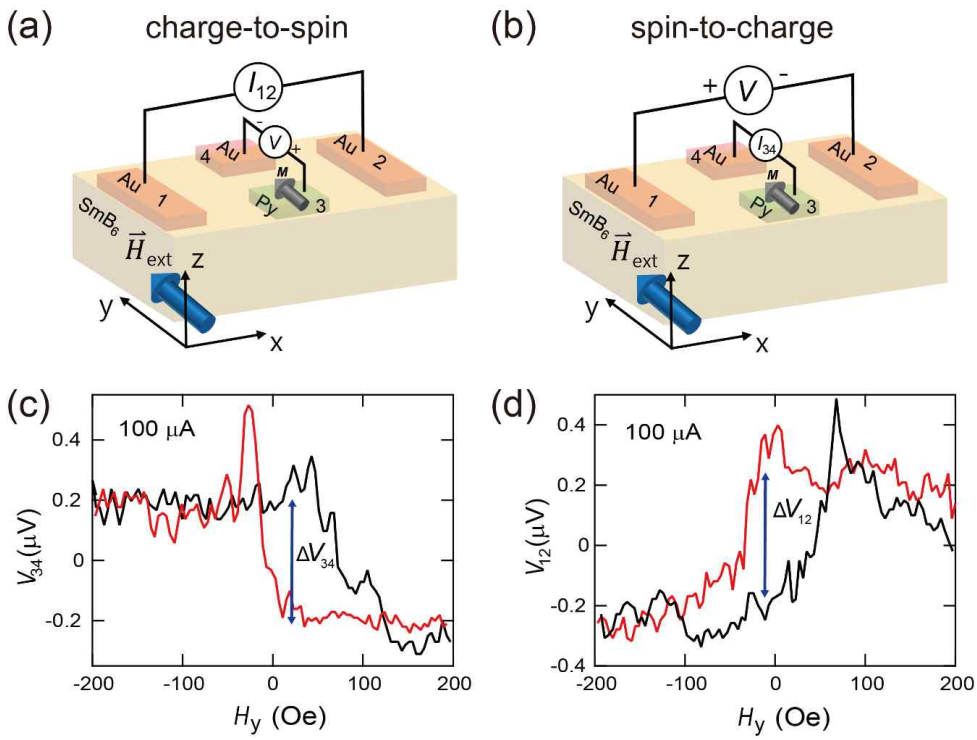

Fig. 3. The Onsager reciprocal relation. (a), (b) Schematic measurement setup for the potentiometric spin measurement (a) and its reciprocal measurement for the IEE (b). (c) V_{34}, defined as $V_3 - V_4$, as a function of an external magnetic field swept along the y axis under I_{12} of 100 μA at 1.8 K, measured in Fig. 3(a) configuration [19]. (d) V_{12}, defined as $V_1 - V_2$, as a function of an external magnetic

field swept along the y axis under I_{34} of 100 μA at 1.8 K, measured in Fig. 3(b) configuration.

3.3.3.S1. Principle of the potentiometric spin measurement and quantitative analysis for surface state spin polarization

The Edelstein effect, the reciprocal effect of IEE, involving charge-to-spin conversion can be measured through the potentiometric spin measurement. Here, we explain principle of the potentiometric spin measurement in SmB_6 and confirm Onsager reciprocal relation between the Edelstein and inverse Edelstein effect, enabling quantitative analysis for surface state spin polarization of SmB_6.

Figure 3.S1(a) shows the electrical measurement configuration for the potentiometric spin measurement, where a bias current I_b flows through a nonmagnetic Au contact on the SmB_6 along the x axis, and the transverse voltage difference V_{xy}, defined as $V_+ - V_-$, is measured between a permalloy ferromagnetic contact (Py) and a nonmagnetic Au contact while sweeping an external magnetic field along the y axis. When a bias current is applied through spin-momentum locked surface states, net electron flow with its locked spin occurs in the opposite direction to the direction of a bias current, which makes spin dependent electrochemical potential in SmB_6 surface channel split due to population imbalance between electrons with spin-up and spin-down. Figures 3.S1(b) and 3.S1(c) show schematic drawings reflecting the explanation above, where the amount of moving electrons with spin-up (spin-down) are depicted in the length of red (blue) arrow parallel (anti-parallel) to the +y direction and the electrochemical potentials for spin-up $\mu_\uparrow$ and spin-down $\mu_\downarrow$ are depicted in the red and blue line, respectively, along the SmB_6 channel. Since the direction of the majority spin of Py is opposite to that of its magnetization and the majority spin of Py is mainly coupled to the SmB_6 surface channel, the spin detector Py with $\boldsymbol{M}$ parallel to the +y (-y) direction can detect the electrochemical potential for

spin-down $\mu_{\downarrow}$ (spin-up $\mu_{\uparrow}$). Therefore, when the direction of net electron flow is parallel to the +x direction, as shown in Fig. 3.S1(b), spin detector Py with $\boldsymbol{M}$ parallel to the +y (-y) direction measures low (high) electrochemical potential, eventually, $V_{xy} > (<) 0$, which is illustrated in Fig. 3.S1(d) as a hysteresis loop with positive polarity. On the other hands, when the direction of net electron flow is parallel to the -x direction, as shown in Fig. 3.S1(c), V_{xy} as a function H_y shows a hysteresis loop with negative polarity as illustrated in Fig. 3.S1(e) due to electrochemical potential splitting reversal. This qualitative explanation has been confirmed experimentally by our previous research [19] and confirms Eq. (1) reflecting the Onsager reciprocal relation.

For quantitative calculation of $\boldsymbol{p}$, Eq. (2) and Eq. (3) can be combined to yield the following equation,

$$\frac{\Delta V_{34}}{I_{12}} - \frac{\Delta V_{12}}{I_{34}} = 2R_{\mathrm{B}}P_{\mathrm{FM}}(\boldsymbol{p}\bullet\boldsymbol{M}_{\mathbf{u}}) \tag{S1}$$

where ballistic resistance of the channel R_{B} is given by h/q^2 times $\pi/k_{\mathrm{F}}W$ (total Fermi wave number k_{F} = 0.67 Å^{-1} [10] and width of the current channel W = 500 μm), P_{FM} of Py at low temperature is 0.38 [30], and unit vector $\boldsymbol{M}_{\mathbf{u}}$ along the magnetization of Py is $\hat{y}$. In the left-hand side of the above equation, $\frac{\Delta V_{34}}{I_{12}}$ and $\frac{\Delta V_{12}}{I_{34}}$ are −2.3 mΩ and 2.7 mΩ, respectively, resulting in $\boldsymbol{p}$ = −27% $\hat{y}$, which means that the magnitude of surface state spin polarization is 27% and SmB_6 has the anticlockwise surface spin texture in the momentum space.

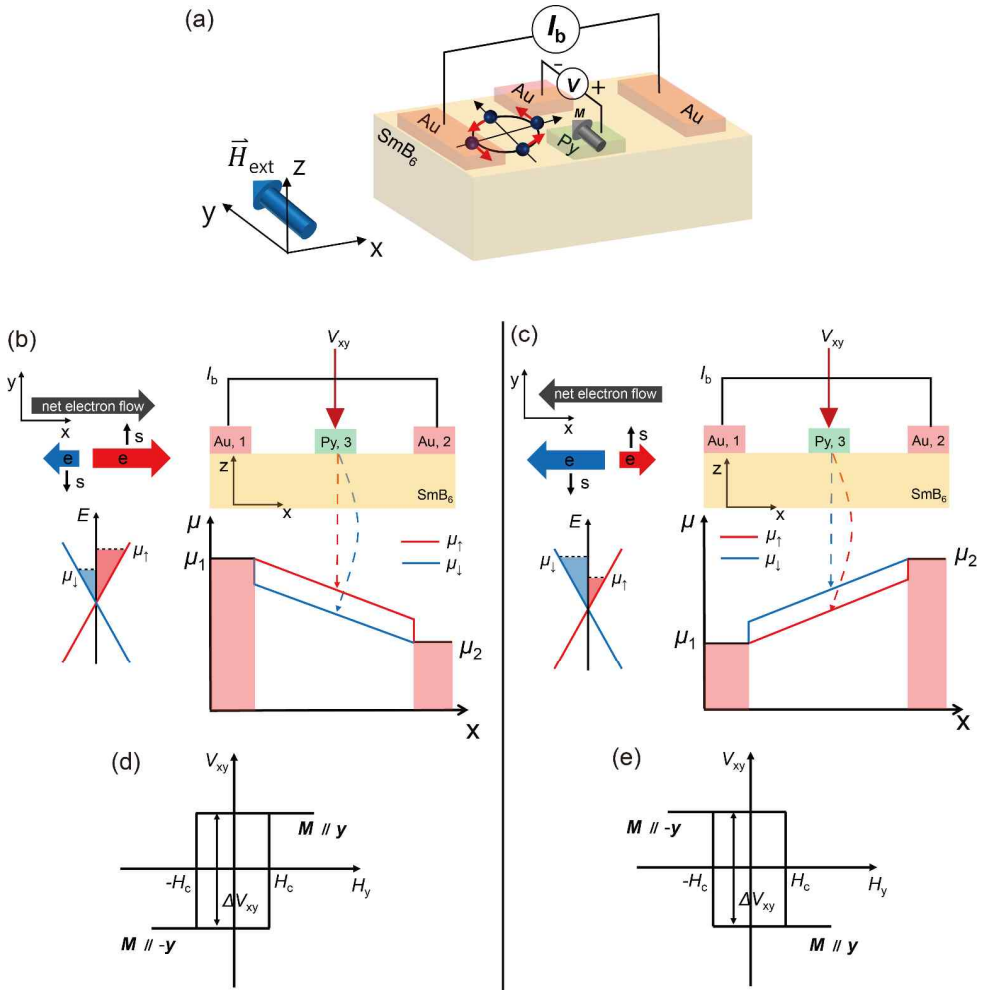

Fig. 3.S1. Principle of electrical measurement for the spin polarization of SmB_6. (a) Schematic drawing for potentiometric spin measurement setup and anticlockwise spin texture for the surface band in SmB_6 near the Fermi energy. (b), (c) Left side of the figure shows degree of electron occupation in the channel and the band structure diagram of the TI surface, and right side of the figure shows spin-dependent electrochemical potential along the SmB_6 channel in case of a bias current applied in the -x direction (b) and in the +x direction (c). (d), (e) The expected V_{xy} as a function of the y component of an external magnetic field H_y under a bias current applied in the -x direction (d) and in the +x direction (e).

3.3.4. Magnetization orientation dependence of IEE signal

To further confirm the spin-momentum relation, we study how the IEE signal depends on the magnetization orientation. Figures 4(a) and 4(b) show the schematic top views of the measurement configurations when an external magnetic field is applied along the y axis and x axis, respectively, under an I_b of 100 μA at 1.8 K. The corresponding results are shown in Fig. 4(c) and 4(d). Owing to the anticlockwise spin texture of the SmB_6 surface band, charge accumulation by spin-to-charge conversion on the surface of SmB_6 occurs along the x axis as depicted in Fig. 4(a), resulting in a measurable ΔV_{yx}, as shown in Fig. 4(c). On the other hand, we can predict that charge accumulation occurs along the y axis when $\boldsymbol{M}$ is parallel to the x axis, as depicted in Fig. 4(b), resulting in no voltage difference between the two voltage probes at high positive or negative H_x, as shown in Fig. 4(d). The intermittent non-zero signal in Fig. 4(d) is likely to be due to magnetic domains in which the transient magnetizations have some y-axis components in the process of magnetization reversal through domain wall motion [31]. Furthermore, the result in Fig. 4(d) also excludes the possibility that the measured ΔV_{yx} originates from spurious effects such as the Hall effect, where non-zero ΔV_{yx} can arise independently of the magnetization orientation owing to the fringe field of the ferromagnetic injector [32]. We also confirm that SmB_6 with all Au contacts in which the Py layer is replaced by the Au layer shows no such field dependent V_{yx}, demonstrating that the Py layer has crucial role in spin injection/extraction (see 3.3.4.S1). Therefore, the magnetization dependence of the IEE signal further offers the conclusion that the measured ΔV_{yx} clearly reflects the anticlockwise spin texture of the SmB_6 surface band.

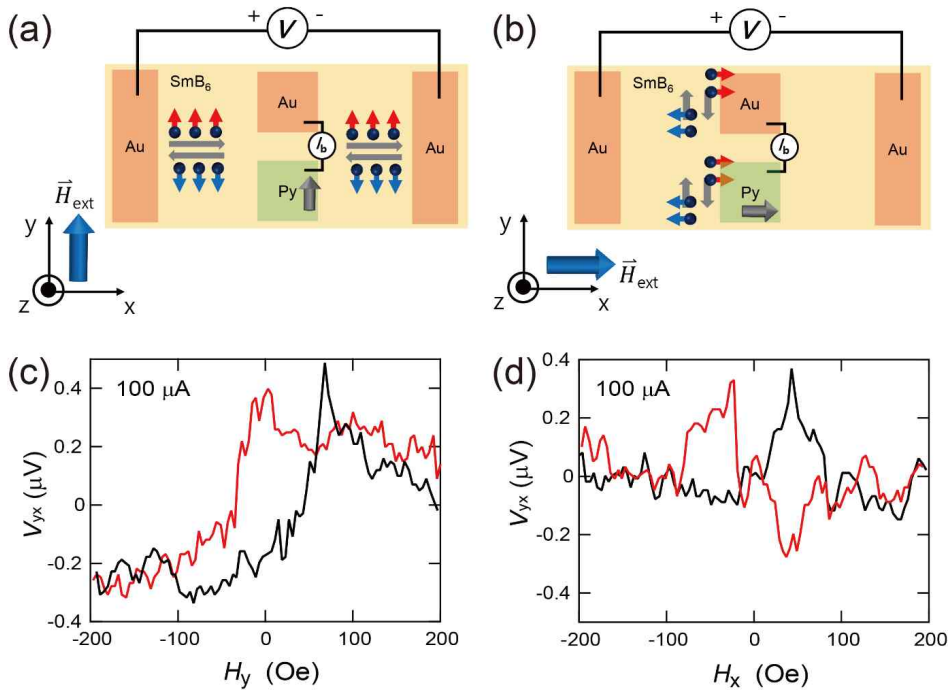

Fig. 4. Magnetization orientation dependence of the IEE signal. (a), (b) Schematic top view of the measurement configuration. An external magnetic field is swept along the y axis in (a) and along the x axis in (b). The grey arrows represent the direction in which electrons with spin-up or spin-down move. (c), (d) V_{yx} as a function of an external magnetic field swept along the y axis (c) and along the x axis (d) under I_b of +100 μA at 1.8 K. The magnetization $\boldsymbol{M}$ is parallel to the y axis (parallel to current direction) in (c) and parallel to the x axis (perpendicular to current direction) in (d).

3.3.4.S1. Contol experiment: A null effect

Control experiment was carried out using only the Au contacts on SmB_6 to measure a null effect. A null effect can be measured when the Py layer used for the spin source is replaced by the Au layer. For confirming a null effect using SmB_6 with all Au contacts, electrical measurements were performed in the measurement setup for the IEE, which is corresponding to the measurements in Fig. 2.

Figure 4.S1(a) shows optical top view of the device used for this measurement, where Au contacts with terminal number 1 to 4 are placed on SmB_6 surface. As shown in Fig. 4.S1(b), to confirm surface-dominate transport properties at low temperature, temperature-dependent electrical resistance $R(T)$ is measured by applying a bias current of 25 μA through terminal 1&2 and measuring the voltage difference between that terminals, clearly exhibiting surface-dominated conduction below 4 K. Figure 4.S1(c) shows V_{yx}, defined as V_1-V_2, measured by sweeping an external magnetic field along the y axis while applying a bias current through terminal 3&4. The result does not show any significant voltage difference between two voltage probes at high positive and negative H_y, demonstrating that the Py layer has crucial role in spin injection/extraction.

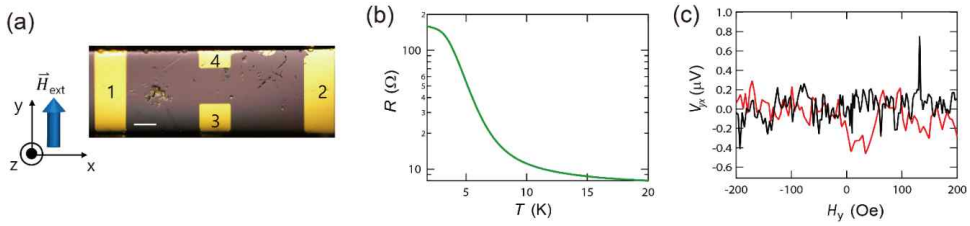

Fig. 4.S1. A null effect measurement (a) Optical microscope image of SmB_6 with all Au contacts. Yellow Au contacts with terminal number 1 to 4 are made on SmB_6 surface. The length of the white scale bar is 100 μm. (b) Electrical resistance of SmB_6 as a function of temperature under a bias current of 25 μA. (c) V_{yx} measured by sweeping an external magnetic field parallel to the y axis under a bias current of +25 μA at 1.8 K.

3.3.5. Temperature dependence of IEE signal

The surface origin of ΔV_{yx} was examined by investigating the temperature dependence of ΔV_{yx}. As shown in Fig. 5(a), the temperature-dependent electrical resistance $R(T)$ of SmB_6 diverges from 12 to 4 K, exhibiting thermally activated behavior, and starts to saturate at 4 K, exhibiting surface-dominated transport properties as confirmed previously [16-18]. Fig. 5(b) shows V_{yx} as functions of H_y under I_b of +100 μA at temperatures

ranging from 4.5 to 1.8 K (marked by red dots in Fig. 5(a)). The variation of the IEE signal ΔV_{yx} with the measurement temperature is extracted from Fig. 5(b) and summarized in Fig. 5(c). As the temperature increases, ΔV_{yx} constantly decreases and vanishes at around 4 K. This resembles the temperature dependence behavior of the SmB_6 electrical resistance, which shows a crossover from surface to bulk-dominated charge conduction at around 4 K. Moreover, although SmB_6 is a heavy metal where the spin Hall and inverse spin Hall effects can occur, the signal from the inverse spin Hall effect does not contribute to the measured ΔV_{yx} at elevated temperatures. This may be largely attributed to the thick bulk channel of SmB_6 in which the reduced spatially averaged spin current in a thicker spin detector material diminishes the inverse spin Hall signal [33]. We also note that the temperature dependence of the measured ΔV_{yx} exhibits a similar behavior to the results of previous temperature-dependent ΔV_{xy} in the potentiometric measurement configuration. This confirms that the Onsager reciprocal relation is valid at different temperatures [19]. Therefore, the temperature dependence of the measured ΔV_{yx} gives strong support for the measured ΔV_{yx} as having originated from the surface states of SmB_6, and largely excludes bulk effects such as the inverse spin Hall effect.

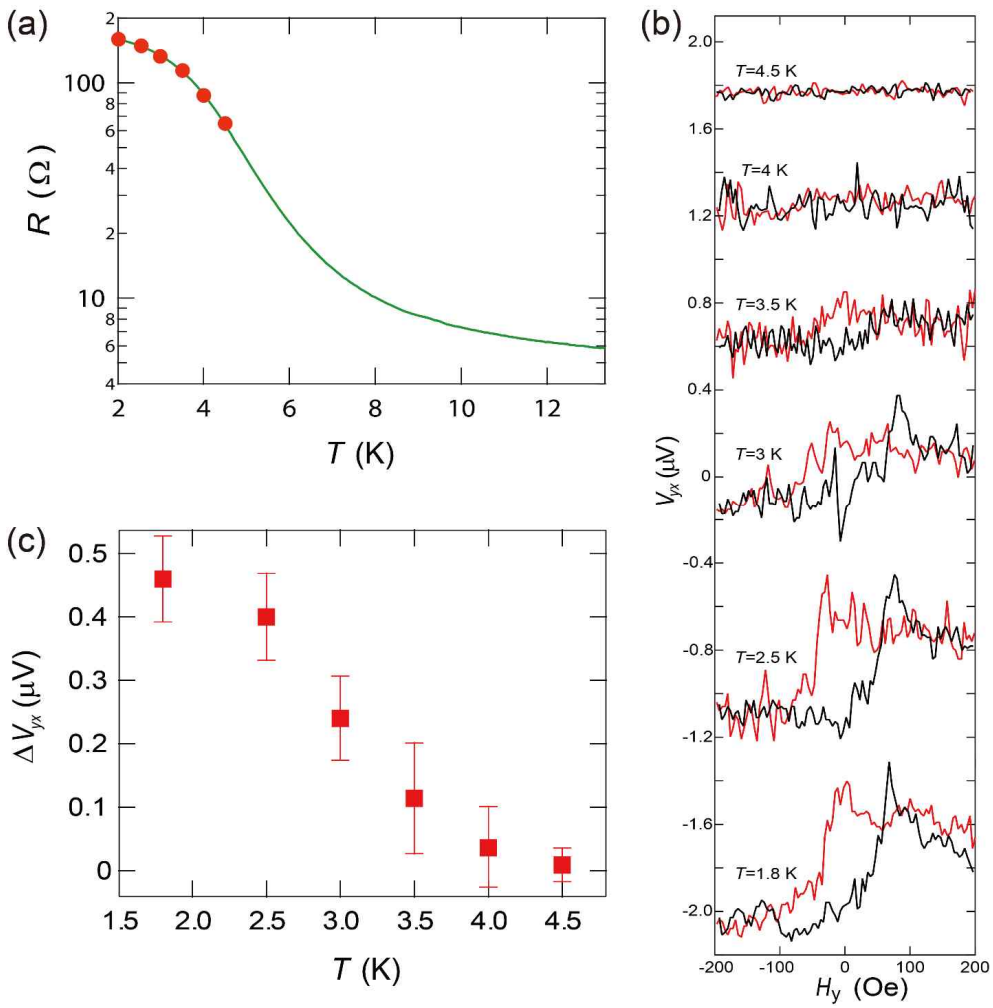

Fig. 5. Temperature dependence of the IEE signal. (a) Electrical resistance of SmB_6 as a function of temperature under a bias current of 300 μA. (b) V_{yx} measured by sweeping an external magnetic field parallel to the y axis under a bias current of +100 μA at different temperatures ranging from 1.8 to 4.5 K. Each curve is offset by 1 μV for clarity. (c) The IEE signal ΔV_{yx} extracted from Fig. 4(b) as a function of temperature.

3.4. Methods

3.4.1. Material growth

Single crystals of SmB_6 were grown with Al flux in the ratio of SmB_6 : Al = 1 : 200–250 starting from elemental Sm and B with a stoichiometry of 1 to

6. The initial materials were placed in an alumina crucible and loaded in a tube furnace under an Ar atmosphere. The assembly was heated to 1250–1400 °C and maintained at that temperature for 70–120 h, then cooled at −2 °C/ h to 600–900 °C, followed by faster cooling. The SmB_6 samples were placed in sodium hydroxide to remove the residual Al flux.

3.4.2. Device fabrication

A 2 nm thick Al layer was deposited on the polished (100) surface of SmB_6 by electron beam evaporation followed by oxidation on a hotplate under ambient conditions. The resulting thin Al oxide layer prevents direct contact of the ferromagnetic metal with SmB_6 and acts as a tunnel barrier between SmB_6 and the ferromagnetic metal. This generally enhances the spin injection and detection ratio by alleviating the conductance mismatch problem [34] (see 3.4.2.S1). Standard e-beam lithography was used to fabricate the electrodes. A permalloy (Py) layer with a lateral size of 150 × 150 μm^2 and thickness of 20 nm was used as a ferromagnetic spin source for spin injection and extraction. The layer was capped with 15 nm of Au using electron beam evaporation. Non-ferromagnetic contacts used for the source, drain, and voltage probes were formed by e-beam lithography patterning and Al oxide etching with a buffered oxide etchant followed by the deposition of 5 nm Ti/ 80 nm Au using electron beam evaporation. To avoid the direct wire bonding to the Py layer which can damage the properties of the Py layer, the Au electrode acting as the wire bonding pad for the contact with the ferromagnetic metal was made using electron beam evaporation and an additional insulating layer was made below this Au electrode by overdosing electron beam on electron beam resist (PMMA 950A6) with a dose of 10000 $\mu C/cm^2$, which enables the Au electrode to be connected directly to the Py layer, not to SmB_6 surface [see the inset to Fig. 1(a)].

3.4.2.S1. Tunneling electron microscopy (TEM) image and the

composition for Al oxide tunneling barrier

In our IEE measurement, Al oxide is used as tunneling barrier for spin injection and extraction to enhance the spin polarization of the tunneling electrons. This Al oxide on SmB_6 crystal is made by thermal oxidation of Al metal in ambient conditions. Figure 2.S1 shows TEM cross section of SmB_6/Al oxide/Py structure (upper image) and the concentration profiles of Al, Fe, Ni, O and Sm elements acquired along the red arrow in the TEM image (bottom image). The TEM image clearly shows the continuous Al oxide layer with almost 2 nm thickness grown on SmB_6. The composition of the Al oxide is analyzed by the concentration profiles obtained by energy dispersive X-ray spectroscopy (EDS) in scanning transmission electron microscopy (STEM) and revealed as AlO_3 containing more oxygen than typical Al oxide, Al_2O_3, which may be attributed to Al_2O_3 mixing with a natural oxide on SmB_6 surface such as boron oxide.

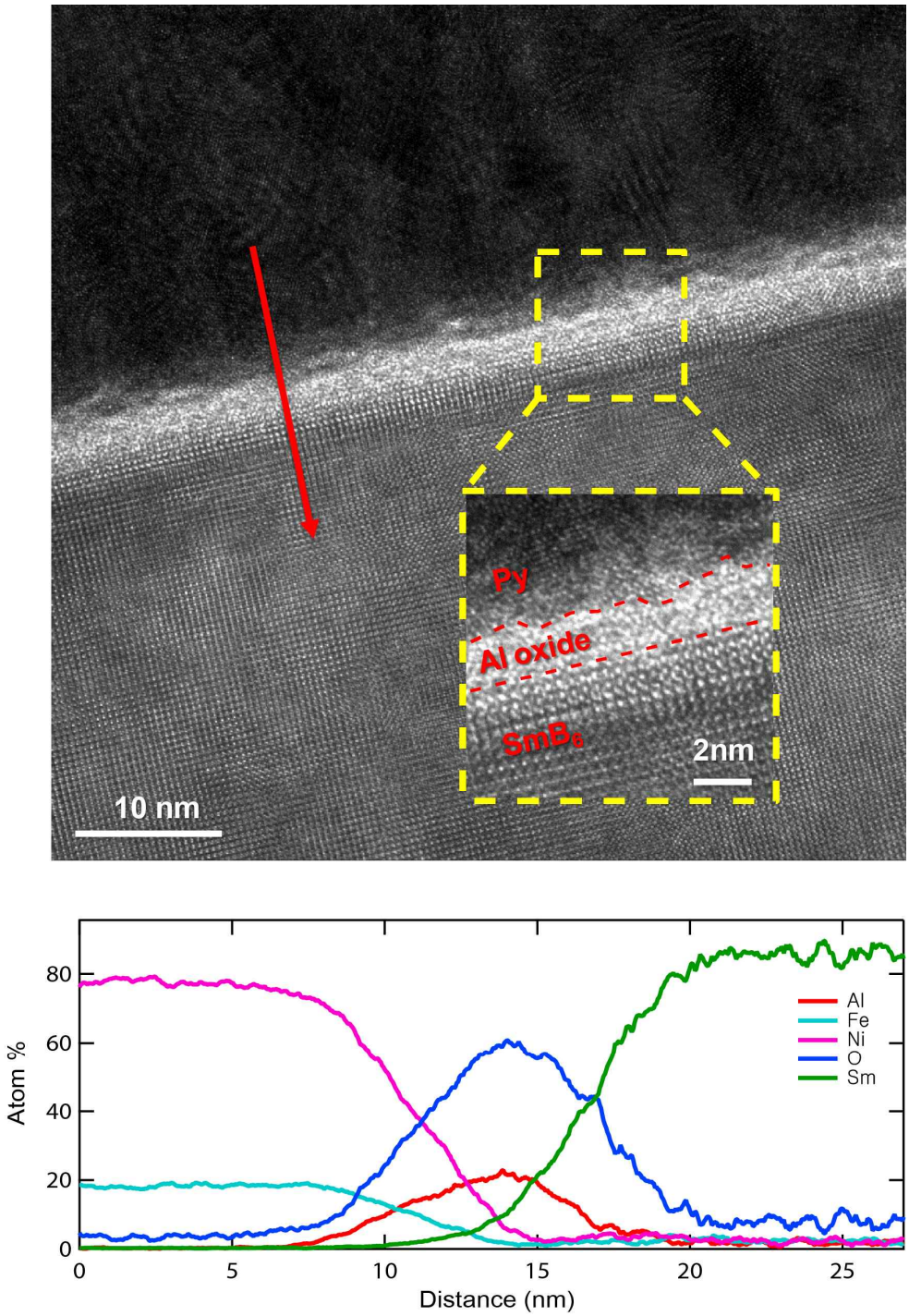

Fig. 2.S1. Transmission electron microscopy (TEM) cross section showing the Al oxide between Py and SmB_6 (top) and the concentration profiles of Al, Fe, Ni, O and Sm elements acquired along the red arrow in the upper figure (bottom).

3.4.3. Transport measurements

The device was placed in a commercial variable temperature cryostat (Quantum Design PPMS) for low-temperature electrical measurements. For all the electrical measurements, standard lock-in-based four-point probe measurements were performed. An AC current was applied through the interfacial tunnel oxide between the ferromagnetic metal Py and the SmB_6 surface using an AC current source (Keithley 6221), and a lock-in amplifier (Stanford Research Systems SR830) was used to detect the voltage difference between two Au contacts.

3.5. Conclusion

The pinning of the Fermi energy near the hybridization-induced gap due to the hybridization of localized *f* electrons with conduction electrons ensures surface-dominated transport in SmB_6 at low temperatures [17,18], thereby excluding the possibility that bulk effects such as the inverse spin Hall effect might have contributed to the measured IEE signal. However, the IEE signal can arise from both the Rashba surface states and topologically-protected surface states because spin-momentum locking is present in both types of surface states. Although it is difficult to separately measure the contributions of the Rashba and topological surfaces to the IEE signal, the measured IEE signal is very likely to consist mainly of the signal from the topological surface. We arrive at this conclusion through the analysis of the IEE length, λ_{IEE}, which is the spin-to-charge conversion efficiency given by [23,35]

$$j_C = \lambda_{IEE} j_S \,,\ \lambda_{IEE} = \frac{|\boldsymbol{p}|\lambda}{\pi} \,, \tag{4}$$

where the charge current density in A m^{-1}, j_c, and spin current density in A m^{-2}, j_s, are connected through λ_{IEE}, which is proportional to the absolute value of the spin polarization $|\boldsymbol{p}|$ and the mean free path of the channel λ. In SmB_6, because the surface conduction is mainly contributed by β band

electrons, λ for the β band (52 nm) [36] and the spin polarization (27%) are used to obtain λ_{IEE}. In our case, λ_{IEE} is 4.46 nm, which is comparable to the λ_{IEE} found in α-Sn film topological insulators without bulk effects [37]. It is

an order of magnitude larger than the λ_{IEE} found in various other Rashba interfaces with typical values of 0.1–0.4 nm owing to the compensation between the two Fermi contours of Rashba interfaces [38-42]. This implies that the Rashba contribution to the IEE signal should be small. Moreover, a large λ_{IEE} also indicates that SmB_6 is a promising candidate for spintronic devices that are potentially useful as efficient spin sources and detectors. With the recently developed technique of increasing the temperature range of surface-dominated transport in SmB_6 by applying strain [43], the material also has potential in spintronic applications at elevated temperatures. Our observation presents a route for the potential application of SmB_6 both in fundamental investigations of the interplay between nontrivial topology and electron correlation, and in applied spin transport physics in strongly correlated systems.

3.6. References

[1] A. R. Akhmerov, J. Nilsson, and C. W. J. Beenakker, *Electrically Detected Interferometry of Majorana Fermions in a Topological Insulator*, Phys. Rev. Lett. **102,** 216404 (2009).

[2] L. Fu and C. L. Kane, *Superconducting proximity effect and Majorana fermions at the surface of a topological insulator*, Phys. Rev. Lett. **100,** 096407 (2008).

[3] J. H. Han, A. Richardella, S. A. Siddiqui, J. Finley, N. Samarth, and L. Q. Liu, *Room-Temperature Spin-Orbit Torque Switching Induced by a Topological Insulator*, Phys. Rev. Lett. **119,** 077702 (2017).

[4] D. Hsieh *et al.*, *A tunable topological insulator in the spin helical Dirac transport regime*, Nature **460,** 1101 (2009).

[5] D. S. Kong *et al.*, *Rapid Surface Oxidation as a Source of Surface Degradation Factor for Bi_2Se_3*, ACS Nano **5,** 4698 (2011).

[6] D. Kim, S. Cho, N. P. Butch, P. Syers, K. Kirshenbaum, S. Adam, J. Paglione, and M. S. Fuhrer, *Surface conduction of topological Dirac electrons in bulk insulating Bi_2Se_3*, Nat. Phys. **8,** 459 (2012).

[7] R. Yu, H. M. Weng, Z. Fang, and X. Dai, *Pseudospin, real spin, and spin polarization of photoemitted electrons*, Phys. Rev. B **94,** 085123 (2016).

[8] R. Yu, H. M. Weng, X. Hu, Z. Fang, and X. Dai, *Model Hamiltonian for topological Kondo insulator SmB_6*, New J. Phys. **17,** 023012 (2015).

[9] M. Dzero, K. Sun, V. Galitski, and P. Coleman, *Topological Kondo Insulators*, Phys. Rev. Lett. **104,** 106408 (2010).
[10] J. Jiang *et al.*, *Observation of possible topological in-gap surface states in the Kondo insulator SmB_6 by photoemission*, Nat. Commun. **4,** 3010 (2013).
[11] Q. Song *et al.*, *Spin injection and inverse Edelstein effect in the surface states of topological Kondo insulator SmB_6*, Nat. Commun. **7,** 13485 (2016).
[12] N. Xu *et al.*, *Direct observation of the spin texture in SmB_6 as evidence of the topological Kondo insulator*, Nat. Commun. **5,** 4566 (2014).
[13] D. J. Kim, J. Xia, and Z. Fisk, *Topological surface state in the Kondo insulator samarium hexaboride*, Nat. Mater. **13,** 466 (2014).
[14] Y. Nakajima, P. Syers, X. F. Wang, R. X. Wang, and J. Paglione, *One-dimensional edge state transport in a topological Kondo insulator*, Nat. Phys. **12,** 213 (2016).
[15] M. Neupane *et al.*, *Surface electronic structure of the topological Kondo-insulator candidate correlated electron system SmB_6*, Nat. Commun. **4,** 2991 (2013).
[16] S. Wolgast, C. Kurdak, K. Sun, J. W. Allen, D. J. Kim, and Z. Fisk, *Low-temperature surface conduction in the Kondo insulator SmB_6*, Phys. Rev. B **88,** 180405 (2013).
[17] D. J. Kim, S. Thomas, T. Grant, J. Botimer, Z. Fisk, and J. Xia, *Surface Hall Effect and Nonlocal Transport in SmB_6: Evidence for Surface Conduction*, Sci. Rep. **3,** 3150 (2013).
[18] P. Syers, D. Kim, M. S. Fuhrer, and J. Paglione, *Tuning Bulk and Surface Conduction in the Proposed Topological Kondo Insulator SmB_6*, Phys. Rev. Lett. **114,** 096601 (2015).
[19] J. Kim, C. Jang, X. F. Wang, J. Paglione, S. Hong, J. Lee, H. Choi, and D. Kim, *Electrical detection of the surface spin polarization of the candidate topological Kondo insulator SmB6*, Phys. Rev. B **99,** 245148 (2019).
[20] V. M. Edelstein, *SPIN POLARIZATION OF CONDUCTION ELECTRONS INDUCED BY ELECTRIC-CURRENT IN 2-DIMENSIONAL ASYMMETRIC ELECTRON-SYSTEMS*, Solid State Communications **73,** 233 (1990).
[21] K. Shen, G. Vignale, and R. Raimondi, *Microscopic Theory of the Inverse Edelstein Effect*, Phys. Rev. Lett. **112,** 096601 (2014).
[22] R. Dey, L. F. Register, and S. K. Banerjee, *Modeling all-electrical detection of the inverse Edelstein effect by spin-polarized tunneling in a topological-insulator/ferromagnetic-metal heterostructure*, Phys. Rev. B **97,** 144417 (2018).
[23] S. Sayed, S. Hong, and S. Datta, *Multi-Terminal Spin Valve on Channels with Spin-Momentum Locking*, Sci. Rep. **6,** 35658 (2016).
[24] J. H. Lee, H. J. Kim, J. Chang, S. H. Han, H. C. Koo, S. Sayed, S. Hong, and S. Datta, *Multi-terminal spin valve in a strong Rashba channel exhibiting three resistance states*, Sci. Rep. **8,** 3397 (2018).
[25] P. Jacquod, R. S. Whitney, J. Meair, and M. Buttiker, *Onsager relations in coupled electric, thermoelectric, and spin transport: The tenfold way*, Phys. Rev. B **86,** 155118 (2012).
[26] M. Hayashi, L. Thomas, Y. B. Bazaliy, C. Rettner, R. Moriya, X. Jiang, and S. S. P. Parkin, *Influence of current on field-driven domain wall motion in permalloy nanowires from time resolved measurements of anisotropic magnetoresistance*, Phys. Rev. Lett. **96,** 197207 (2006).
[27] H. Corte-Leon, V. Nabaei, A. Manzin, J. Fletcher, P. Krzysteczko, H. W. Schumacher, and O. Kazakova, *Anisotropic Magnetoresistance State Space of Permalloy Nanowires with Domain Wall Pinning Geometry*, Sci. Rep. **4,** 6045 (2014).
[28] S. Hong, V. Diep, S. Datta, and Y. P. Chen, *Modeling potentiometric measurements in topological insulators including parallel channels*, Phys. Rev. B **86,** 085131 (2012).
[29] L. Q. Liu, A. Richardella, I. Garate, Y. Zhu, N. Samarth, and C. T. Chen, *Spin-polarized tunneling study of spin-momentum locking in topological insulators*, Phys. Rev. B

91, 235437 (2015).
[30] E. Villamor, M. Isasa, L. E. Hueso, and F. Casanova, *Temperature dependence of spin polarization in ferromagnetic metals using lateral spin valves*, Phys. Rev. B **88,** 184411 (2013).
[31] D. Romel, E. R. Burke, and I. D. Mayergoyz, *Magnetic imaging in the presence of external fields: Technique and applications*, Journal of Applied Physics **79,** 6441 (1996).
[32] E. K. de Vries, A. M. Kamerbeek, N. Koirala, M. Brahlek, M. Salehi, S. Oh, B. J. van Wees, and T. Banerjee, *Towards the understanding of the origin of charge-current-induced spin voltage signals in the topological insulator Bi_2Se_3*, Phys. Rev. B **92,** 201102(R) (2015).
[33] V. Castel, N. Vlietstra, J. Ben Youssef, and B. J. van Wees, *Platinum thickness dependence of the inverse spin-Hall voltage from spin pumping in a hybrid yttrium iron garnet/platinum system*, Applied Physics Letters **101,** 132414 (2012).
[34] E. I. Rashba, *Theory of electrical spin injection: Tunnel contacts as a solution of the conductivity mismatch problem*, Phys. Rev. B **62,** R16267 (2000).
[35] S. Sayed, S. Hong, and S. Datta, *Transmission-Line Model for Materials with Spin-Momentum Locking*, Physical Review Applied **10,** 054044 (2018).
[36] G. Li *et al.*, *Two-dimensional Fermi surfaces in Kondo insulator SmB6*, Science **346,** 1208 (2014).
[37] J. C. Rojas-Sanchez *et al.*, *Spin to Charge Conversion at Room Temperature by Spin Pumping into a New Type of Topological Insulator: alpha-Sn Films*, Phys. Rev. Lett. **116,** 096602 (2016).
[38] M. Matsushima, Y. Ando, S. Dushenko, R. Ohshima, R. Kumamoto, T. Shinjo, and M. Shiraishi, *Quantitative investigation of the inverse Rashba-Edelstein effect in Bi/Ag and Ag/Bi on YIG*, Applied Physics Letters **110,** 072404 (2017).
[39] W. Zhang, M. B. Jungfleisch, W. J. Jiang, J. E. Pearson, and A. Hoffmann, *Spin pumping and inverse Rashba-Edelstein effect in NiFe/Ag/Bi and NiFe/Ag/Sb*, Journal of Applied Physics **117,** 17C727 (2015).
[40] S. Sangiao, J. M. De Teresa, L. Morellon, I. Lucas, M. C. Martinez-Velarte, and M. Viret, *Control of the spin to charge conversion using the inverse Rashba-Edelstein effect*, Applied Physics Letters **106,** 172403 (2015).
[41] A. Nomura, T. Tashiro, H. Nakayama, and K. Ando, *Temperature dependence of inverse Rashba-Edelstein effect at metallic interface*, Applied Physics Letters **106,** 212403 (2015).
[42] J. C. Rojas Sanchez, L. Vila, G. Desfonds, S. Gambarelli, J. P. Attane, J. M. De Teresa, C. Magen, and A. Fert, *Spin-to-charge conversion using Rashba coupling at the interface between non-magnetic materials*, Nat. Commun. **4,** 2944 (2013).
[43] A. Stern, M. Dzero, V. M. Galitski, Z. Fisk, and J. Xia, *Surface-dominated conduction up to 240 K in the Kondo insulator SmB6 under strain*, Nat. Mater. **16,** 708 (2017).

Chapter 4. High-visibility single-shot readout of singlet-triplet qubits in a micromagnet-integrated quadruple quantum dot array

Wonjin Jang[1†], Jehyun Kim[1†], Min-Kyun Cho[1], Hwanchul Chung[2], Jaeun Eom[1], Vladimir Umansky[3], Yunchul Chung[2], and Dohun Kim[1]*

[1]*Department of Physics and Astronomy, and Institute of Applied Physics, Seoul National University, Seoul 08826, Korea*

[2] *Department of Physics, Pusan National University, Busan 46241, Korea*

[3]*Braun Center for Submicron Research, Department of Condensed Matter Physics, Weizmann Institute of Science, Rehovot 76100, Israel*

[†]*These authors contributed equally to this work*

**Corresponding author: dohunkim@snu.ac.kr*

This work was published in "npj Quantum Information"

4.1. Abstract

Fast and high-fidelity quantum state detection is essential for building robust spin-based quantum information processing platforms in semiconductors. The Pauli spin blockade (PSB)-based spin-to-charge conversion and its variants are widely used for the spin state discrimination of two-electron singlet–triplet (ST_0) qubits; however, the single-shot measurement fidelity is limited by either the low signal contrast, which depends on the charge sensor position, or the short lifetime of the triplet state at the PSB energy detuning, especially due to strong mixing with singlet states at large magnetic field gradients. Ultimately, the limited single-shot measurement fidelity leads to low visibility of quantum operations. Here, we demonstrate an alternative method to achieve spin-to-charge conversion of ST_0 qubit states using energy selective tunneling between doubly occupied quantum dots (QDs) and electron reservoirs, commonly called Elzerman type readout. We demonstrate a single-shot measurement fidelity of 93% and an S–T_0 oscillation visibility of 81% at a

field gradient of 100 mT without the necessity to convert to intermediate metastable states first; this allows single-shot readout with full electron charge signal contrast and, at the same time, long and tunable measurement time with negligible effect of relaxation even at strong magnetic field gradients. Using an rf-sensor positioned opposite to the QD array, we further apply this method to two ST_0 qubits and show that high-visibility readout of two individual single-qubit gate operations is possible with a single rf single-electron transistor sensor. We expect that our measurement scheme for two-electron spin states, analogous to single-electron spin-to-charge conversion, can be applied to various hosting materials and provides a simplified and unified route for multiple qubit state detection with high accuracy in QD-based quantum computing platforms.

4.2. Introduction

The assessment of general quantum information processing performance can be divided into that of state initialization, manipulation, and measurement. Rapid progress has been made in semiconductor quantum dot (QD) platforms, with independent demonstrations of, for example, high-fidelity state initialization of single and double QD spin qubits [1-3], high-fidelity quantum control with resonant microwaves [4-7] and non-adiabatic pulses [1,8,9], and high-fidelity state measurements using spin-to-charge conversion [10-16]. However, the high visibility of a quantum operation requires high fidelity in all stages of the quantum algorithm execution, which has been demonstrated in only a few types of spin qubits so far [4,6,9,17].

For double QD two-electron spin qubits, the Pauli spin blockade (PSB) phenomenon is typically used for discriminating spin-singlet (S) and -triplet (T_0) states where different spin states are mapped according to the difference in the relative charge occupation of two electrons inside the

double QD, which is detected by a nearby electrometer [18-20]. However, depending on the device design, the signal contrast can be small compared to the signal of one electron, especially when the charge sensor position in the device is not aligned with the QD axis. This issue is particularly problematic in recent multiple QD designs [21-23], where the charge sensor positioned opposite to the qubit array increases the range of QDs detectable by one sensor, but renders sensitive measurement of the relative electron position between nearest-neighbor dots difficult.

Moreover, the magnetic field gradient along the QD axis ΔB_z provides relaxation pathways through (1,1)T_0–(1,1)S mixing and rapid (1,1)S to (2,0)S tunneling in the PSB region, and normal PSB readout is difficult under large ΔB_z, as shown in the solid green regions in Fig. 1(a) As most QD spin qubit platforms utilize sizeable intrinsic [2,24,25] or extrinsic [26] ΔB_z to realize individual qubit addressing and high-fidelity single- and two-qubit operations [4,6,27,28], it is important to develop fast readout techniques that enable high-fidelity spin detection even at large ΔB_z. So far, high visibility of approximately 90% using PSB readout can be achieved only for small ΔB_z [12].

These limitations of conventional PSB readout have been addressed in previous works, and several variants of the PSB readout have been developed for various QD systems [13-16]. In the latched readout scheme [13], the lack of the reservoir on one side of the double QD enables spin conversion to the (1,0) or (2,1) charge state, enhancing the signal contrast. In Ref [14], singlet–triplet (ST_0) qubit readout was performed in a triple QD to isolate the middle QD from the reservoirs, and the qubit state conversion to a metastable charge state enabled robust, high-fidelity qubit readout. While these techniques enhance the signal contrast to the full electron charge, it is expected that the fast relaxation of the T_0 state at PSB detuning ε can still affect the final quantum oscillation visibility. On the other hand,

Orona, L. A. et al. [15] reported the shelving readout technique, whereby one of the qubit states is first converted to the T_+ state through fast electron exchange with the reservoir to prevent mixing with the (1,1)S state, enabling high-visibility readout of the ST_0 spin qubit. They showed explicitly that single-shot readout is possible even for ΔB_z ~ 180 mT by optimizing the shelving pulse sequence. However, the technique relies on PSB for final spin-to-charge conversion and is expected to be effective only when the charge sensor is sensitive to the relative position of electrons in the double QD.

Here, we demonstrate the energy selective tunneling (EST) readout, commonly called Elzerman readout [10], of ST_0 qubits under large ΔB_z, accomplishing both signal enhancement, due to one electron tunneling, and long measurement time, enabling a robust single-shot readout. EST readout of the two electron spin states in a single QD was performed previously [11], but the explicit application of such readout with high-fidelity coherent operation at large ΔB_z has not been reported to date. Unlike previous works, which demonstrated independent enhancement of the signal contrast and measurement time through intermediate spin or charge state conversion steps, our scheme does not require additional state conversion during the readout. Using large voltage modulation by rapid pulsing with ε ranging from the PSB-lifted (2,0) to the deep (1,1) charge regions, where the exchange coupling $J(\varepsilon)$ is turned off, we explicitly demonstrate a single-shot measurement fidelity of 93% and an S–T_0 oscillation visibility of 81% at ΔB_z ~ 100 mT, corresponding to an oscillation frequency of 500 MHz. Furthermore, we demonstrate the detection of coherent operation of two individual ST_0 qubits in a quadruple QD array with a single rf-reflectometry line. In this section, we describe the proposed EST readout method in detail, compare it with the conventional PSB readout, and suggest possible routes for its further optimization.

4.3. Results

4.3.1. Energy levels and device platform

The blue rectangular regions in Fig. 1(a) show the position of ε and the energy level configuration used for EST state initialization and readout. At this readout point, the PSB is lifted, and both S and T_0 levels can first occupy the (2,0) charge state, the energies of which are separated by ST_0 splitting typically in the order of ~20–30 GHz [29], depending on the dot-confining potential. Near the (1,0) - (2,0) electron transition, the electrochemical potential of the reservoir resides between these states, which enables the EST of the ST_0 qubits. As discussed in detail below, we observe the single-shot spin-dependent tunneling signal where one electron occupying an excited orbital state of the (2,0)T_0 state tunnels to the reservoir to form the (1,0) charge state, leading to an abrupt change in the sensor signal, and predominantly initializes back to the energetically favorable (2,0)S state. In contrast, no tunneling occurs for the (2,0)S state (see Fig. 1(a), blue right panel).

We study a quadruple QD array with an rf single-electron transistor (rf-set) sensor consisting of Au/Ti metal gates on top of a GaAs/AlGaAs heterostructure, where a 2D electron gas (2DEG) is formed approximately 70 nm below the surface (Fig. 1(b)). A 250 nm-thick rectangular Co micromagnet with large shape anisotropy was deposited on top of the heterostructure to generate stable ΔB_z for ST_0 qubit operation [26,30-32] (see methods section for fabrication details). The device was placed on a plate in a dilution refrigerator at ~20 mK and an in-plane magnetic field $B_{z,ext}$ of 225 mT was applied. To demonstrate the EST readout in the experiment, we independently operated and readout two ST_0 qubits (Q_L and Q_R) in the non-interacting regime by blocking Q_L–Q_R tunneling using appropriate gate voltages. We monitored the rf-reflectance of the rf-set

sensor (Fig. 1(b), yellow dot) for fast single-shot charge occupancy detection in the μs time scale [33,34]. The intra qubit tunnel couplings for both Q_L and Q_R were tuned above 8 GHz to suppress unwanted Landau–Zener–Stuckelberg interference under fast ε modulation, and we estimated the electron temperature to be approximately 230 mK (see 4.3.1.S1).

We first locate appropriate EST readout points in the charge stability diagrams. Figure 1(c) (1(d)) shows the relevant region in the stability diagram for the Q_L (Q_R) qubit operation as a function of two gate voltages V_1 (V_3) and V_2 (V_4). We superimpose the cyclic voltage pulse, sequentially reaching I – W – O – W – R points in the stability diagram (see Fig. 1(c) and 1(d)) with a pulse rise time of 200 ps. During the transition from the point W to point O stage, the pulse brings the initialized (2,0)S state to the deep (1,1) region non-adiabatically, and the time evolution at point O results in coherent S-T_0 mixing due to ΔB_z. The resultant non-zero T_0 probability is detected at the I/R point. For this initial measurement, the duration of each pulse stage was not strictly calibrated, but the repetition rate was set to 10 kHz. The resulting 'mouse-bite' pattern inside the (2,0) charge region (Fig. 1(c), boundary marked by the red dashed line) implies the (1,0) charge occupancy within the measurement window, which arises from the EST of the ST_0 qubit states averaged over 100 μs. For comparison, we note that the PSB readout signal with a similar pulse sequence is not clearly visible in the main panel of Fig. 1(c) in the time-averaged manner due to fast relaxation, as described above. The inset in Fig. 1(c) shows the PSB readout signal measured by gated (boxcar) integration (see 4.3.1.S2), where an approximately 100 ns gate window was applied immediately after the pulse sequence. This difference in the available range of measurement time scale clearly contrasts two distinct readout mechanisms for the spin-to-charge conversion of ST_0 qubits.

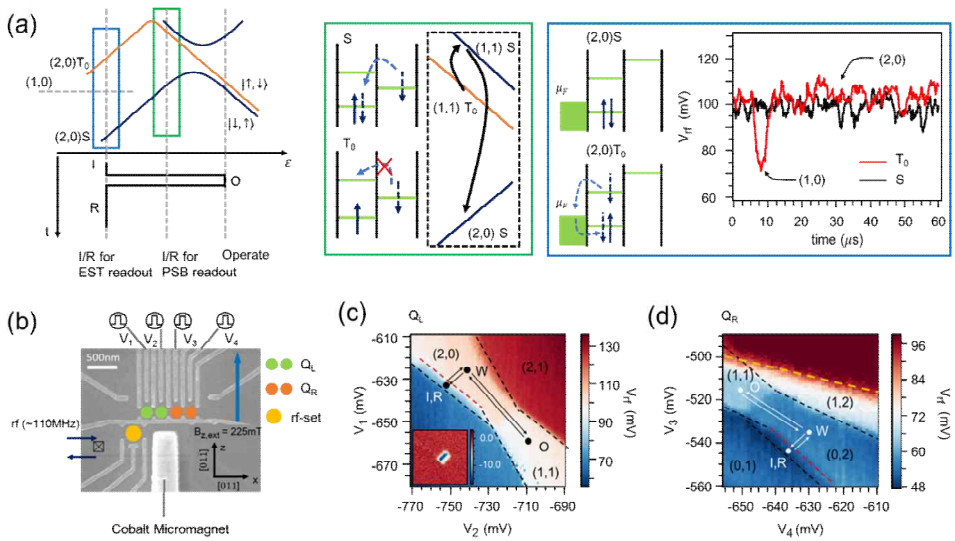

Fig. 1. Energy levels and device platform. (a) Schematic of the singlet–triplet (ST_0) qubit energy levels as a function of detuning ε with energy selective tunneling (EST, blue boxes)- and Pauli spin blockade (PSB, green boxes)-based readout schemes. Green panel: At the PSB readout point, the (1,1)S state tunnels into the (2,0) charge state while the tunneling from the $(1,1)T_0$ state is blocked. The relative charge position is observed to determine the spin state of the qubit. $(1,1)T_0$–(1,1)S mixing under the finite magnetic field gradient ΔB_z provides a relaxation pathway for the $(1,1)T_0$ state. Blue panel: Energy level configuration and a single-shot readout signal at the EST readout point. The Fermi level resides between the (2,0)S and $(2,0)T_0$ states, which enables EST. The triplet state (red) tunnels out to the (1,0) state and initializes to the (2,0)S state, while no tunneling occurs for the S state. (b) Scanning electron microscopy image of the device. Green (orange) dots indicate the position of the left (right) ST_0 qubit Q_L (Q_R), and the yellow dot indicates the rf single-electron transistor (rf-set) position. The blue arrow indicates the external magnetic field direction. (c) ((d)) Double QD charge stability diagram for Q_L (Q_R) operation with the 100 μs-period pulse cycling I – W – O – W – R points superimposed with raster scanning gate voltages. The red dashed line shows the boundary of the (2,0) charge stability region inside which the EST readout is appropriate. The inset of (c) shows the PSB readout signal for the same gate voltage area observed by gated (boxcar) integration. The yellow line in (d) shows the electron transition signal of the QD coupled to V_2.

4.3.1.S1. Electron temperature and intra-qubit tunnel coupling calibration

Electron temperature, and the tunnel coupling strength of the left double quantum dot are measured using the standard lock-in technique. dV_{rf}/dV_2 is observed by modulating V_2 gate voltage with 337Hz frequency. With proper adjustment of dot-reservoir tunnel rates less than 1 MHz and setting minimal modulation amplitude, the electron temperature $T_e \sim 230$mK is determined by fitting the heterodyne detected single electron transition line to the equation $\frac{dV_{rf}}{dV_2}(V_1) = A_{offset} - \frac{A\alpha}{k_B T}\frac{\exp(\alpha(V_1 - V_{offset})/k_B T)}{(1+\exp(\alpha(V_1 - V_{offset})/k_B T))^2}$, which is the derivative of the typical Fermi-Dirac distribution (Fig. 1.S1(a)). Here $\alpha = 0.035$ is the lever-arm of the V_1 gate obtained from the Coulomb diamond measurement, k_B is the Boltzmann constant, and A_{offset} and V_{offset} are the dV_{rf}/dV_2 offset and the offset V_1 voltage in the $dV_{rf}/dV_2 - V_1$ plot, respectively. The intra-qubit tunnel coupling strength t_c was obtained in the similar manner, by sweeping the gate voltage through the inter-dot transition line in the stability diagram for example shown in Fig. 1(c). The broadening is fitted using the same equation described above, with the broadening width $2t_c$ instead of $k_B T$ where the t_c represents the tunnel coupling strength. The resultant $2t_c/h$ is 16 GHz where h is the Plank's constant.

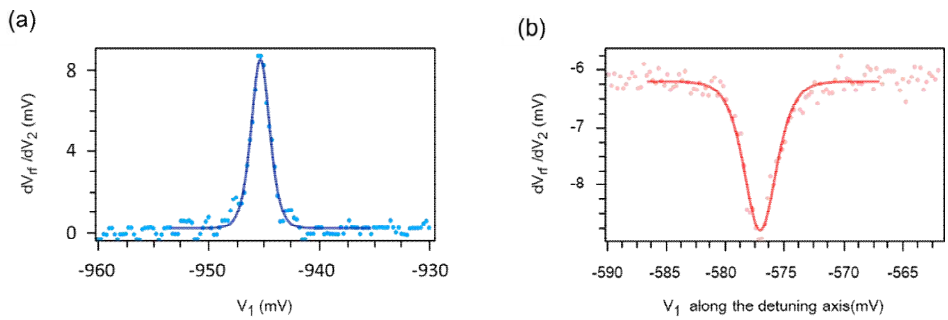

Fig. 1.S1. System parameter calibration. (a) Electron temperature measurement. (b) tunnel coupling strength measurement using the heterodyne detection scheme.

Typical lock-in measurement was performed to obtain the broadening of the single electron transition due to thermal broadening and the intra-qubit tunneling. Electron temperature $T_e \sim 230$ mK, and tunnel coupling $t_c/h \sim 8$GHz were obtained from the fitting. When obtaining (b) both V_1, and V_2 were swept through the inter-dot transition line in Fig. 1(c), but only the V_1 gate voltage is shown in the x-axis.

4.3.1.S2. Correlated double sampling (CDS)

By resampling the demodulated rf-signal with the boxcar integrator, we enable the real-time single-shot event counting without the use of field-programmable gate arrays (FPGA) programming. As shown in Fig. 1.S2, the boxcar integrator subtracts the 100 ns-averaged baseline signal from the gate signal which are separated by 5 μs in the time domain to yield a pseudo-time derivative signal of the single-shot trace with 200 kHz sampling rate. CDS converts the falling (rising) edge to the positive (negative) peak and the peaks are detected by the external photon counter (Stanford Research Systems SR400) as shown in Fig. 1.S2(a). This allows the separate detection of tunneling in / out event in real-time without post-processing which may reduce the experimental overhead in the analysis step. By counting the tunneling out events, we have observed the coherent singlet-triplet qubit (ST_0 qubit) oscillations in the energy selective tunneling (EST) readout point. For single-shot readout, the boxcar integrator is operated with average number set to 1 (no averaging).

When averaged, however, the CDS technique can also be utilized to observe short-lived T_0 signal for Pauli Spin Blockade (PSB) readout, which enable measurement bandwidth of 33MHz in time averaged manner (see also the inset to Fig. 1(c)). By setting the ~ 0.1 μs gate window right after the spin-mixing pulse comes back to the PSB region, and the ~ 0.1 μs baseline gate window before the next pulse start as shown in Fig. 1.S2(b), the demodulated signal is effectively sampled for short time where

the portion of the T_0 signal is sufficiently large to be observed with sufficient periodic average.

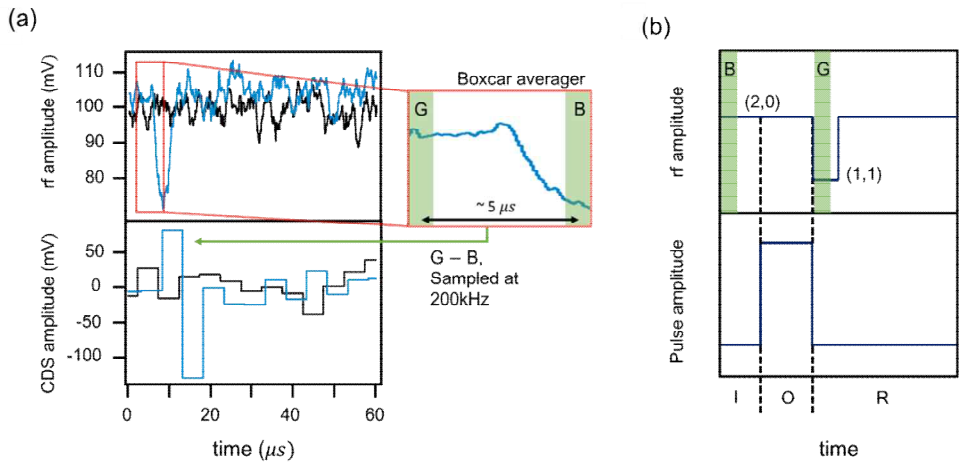

Fig. 1.S2. Correlated double sampling schematics. (a) Correlated double sampling for tunneling out / in event detection. Boxcar integrator resamples the bare demodulated rf signal by subtracting the ~ 100 ns averaged baseline (B) signal from the gate (G) signal every 5 μs . This resampling process converts the falling edge signal of the rf signal to a positive peak with removing dc background and produces pulse signal robust to background drift. (b) CDS scheme for short T_0 signal detection in PSB readout. Pulse mixes the S and T_0 states in the operation (O) sequence, and when returning to the readout (R) step, the T_0 quickly relaxes to (2,0) charge state under large magnetic field gradient. The boxcar integrator in this case is operated in averaging mode where sampled signal G of the rf-signal for short period time after the pulse sequence are subtracted by the B signal and averaged about 5000 times to increase signal to noise ratio.

4.3.2. Time-resolved relaxation measurements and fidelity analysis

The PSB and EST readouts are systematically compared through time-resolved relaxation measurements, which also serve as calibration of the readout parameters for EST readout visibility optimization. Fig. 2(a) (2(b)) shows the relaxation of the sensor signal as a function of waiting time τ before reaching the measurement stage, using the pulse sequence shown in the inset of Fig. 2(a) (2(b)) near the PSB (EST) readout position for Q_L. The

corresponding measurement results for Q_R are described in 4.3.2.S1. As expected, the lifetime T_1 of the T_0 state at the PSB region is in the order of 200 ns, indicating strong spin state mixing and subsequent charge tunneling due to the large ΔB_z produced by the micromagnet (see 4.3.2.S2 for ΔB_z simulation). However, at large negative ε, the PSB is eventually lifted, and the absence of rapid spin mixing as well as the insensitivity of the (2,0)T_0 – (2,0)S spin splitting to charge fluctuations ensures the long lifetime of the T_0 state. The evolution time at O is varied in the EST relaxation time measurement in Fig. 2(b), and the amplitude decay of the coherent oscillation is probed to remove background signals typically present for long pulse repetition periods. The resultant T_1 of 156 μs is three orders of magnitude longer than that in PSB readout. Note that this T_1 is taken at ε near (1,1)T_0 – (2,0)T_0 anti-crossing; thus, an even longer T_1 is expected at the actual ε measurement position selected for EST readout, which is difficult to measure due to the limitation of the low frequency cut off of the bias tee in the order of 1 kHz. Without fast ε modulation, a long T_1 exceeding 2.5 ms has been reported in GaAs QDs [35].

Next, we discuss the calibration of the tunnel rates for single-shot readout and the optimization of the readout fidelity and visibility with the given experimental parameters. While for time-averaged charge detection we use a minimum integration time of 30 ns in the signal demodulation setup, corresponding to a measurement bandwidth of 33 MHz, we set the integration time to 1 μs for single-shot detection to increase the signal to noise ratio, and we typically tune the tunneling rates to less than 1 MHz. Fig. 2(c) shows time-resolved tunnel out events triggered by the end of the pulse sequence from which we measure the tunneling out rate $\nu_{out} \sim \tau_{out}^{-1} = (16\mu\text{s})^{-1}$, extracted from the fit to an exponentially decaying function. The rate is within our measurement bandwidth. Also note that the ratio T_1 / τ_{out} is at least 10, which is reasonable to perform high-fidelity

measurements. Fig. 2(d) shows the resultant histogram showing a separation of the mean value of the S and T_0 signal levels of more than 8 times the standard deviation, confirming the high fidelity of single-shot spin state detection with 1 μs integration time. We also find good agreement between the experimental and numerically simulated single-shot histograms[3] generated using the measured tunneling rates and signal to noise ratio.

After the rf demodulation stage, we further apply correlated double sampling (CDS) [14] to the single-shot traces to simplify the state discrimination and measurement automation. Using a fast boxcar integration with two gate windows that are 5 μs apart in the time domain, a dc background-removed pseudo-time derivative of the single-shot traces is generated, enabling separate detection of tunneling out/in events with an external pulse counter (Stanford Research Systems, SR400 dual gated photon counter) and time-correlated pulse counting with a multichannel scaler (Stanford Research Systems, SR430 multichannel scaler) without the need for customized field-programmable gate array (FPGA) programming [36,37] (see 4.3.1.S2 for details of the CDS scheme). While this scheme was successful, the electronic measurement bandwidth was further reduced to 200 kHz for single-shot detection, which resulted in a relatively long readout time requiring relatively slow tunneling rates. To simulate realistic measurement conditions, we applied the numerical CDS filter to the simulated single-shot traces (Fig. 2(e)) and reproduced the measurement fidelity and visibility (see 4.3.2.S3 for measurement fidelity analysis). The resulting theoretical measurement fidelity of the left qubit is 93%, corresponding to a visibility of 86%, confirming that high-fidelity single-shot detection is possible at the given experimental conditions (see 4.3.2.S1 for right qubit analysis). Moreover, in section 4.3.2.S4, we show through numerical simulation that FPGA-based single-shot detection, which we plan to perform in the future, will yield a measurement fidelity (visibility) of 97% (93%) at the same experimental condition through faster and more

accurate peak detection. Thus, we conclude that the measurement fidelity and visibility obtained in this study, while showing the highest values for ST_0 qubit operation at large ΔB_z, are mainly limited by the CDS technique used and can be improved in a straightforward manner in the future.

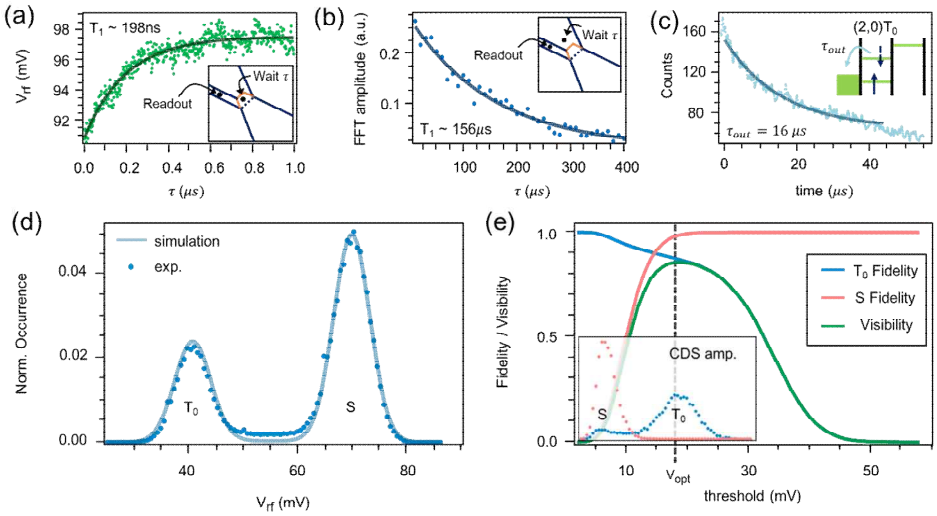

Fig. 2. Time-resolved relaxation measurements and fidelity analysis of Q_L. (a) Relaxation time measurement at PSB readout. The time-averaged rf-demodulated signal V_{rf} is recorded as a function of the waiting time τ at the ε denoted in the inset. $T_1 \sim 200$ ns is extracted from the fitting data to the exponential decay curve. (b) Relaxation time measurement near EST readout. The decay of the coherent oscillation is observed along the waiting time τ near the PSB-lifted $(1,1)T_0$–$(2,0)T_0$ excited anti-crossing position denoted in the inset. $T_1 \sim 156\,\mu s$ is extracted, while even longer T_1 in the actual EST readout ε is expected. (c) Histogram of the tunneling out events triggered by the end of the manipulation pulse as a function of time. (d) Histogram of the experimental and simulated rf-demodulated single-shot traces with the application of π pulses for EST readout showing a mean value separation of more than 8 times the standard deviation. (e) Measurement fidelity and visibility calculated from the CDS peak amplitude histogram shown in the inset. Maximum visibility of ~86% and a corresponding measurement fidelity of 93% are estimated at the optimal threshold voltage V_{opt}.

4.3.2.S1. Right qubit measurement fidelity

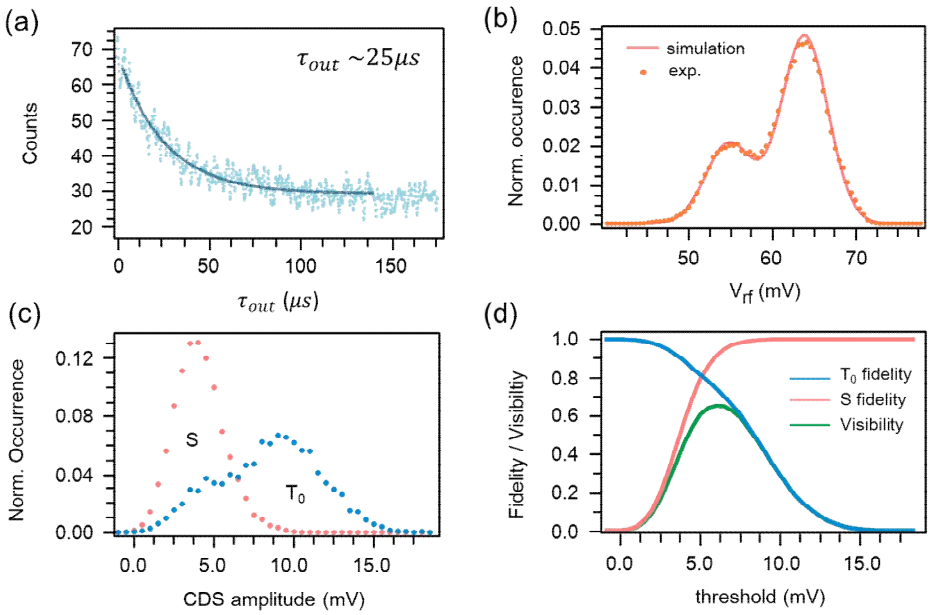

Fig. 2.S1. Right qubit readout fidelity analysis. (a) Tunneling out rate of the right qubit Q_R at the EST readout point. Tunneling out events were recorded as a function of the tunneling time, and the exponential fit to the curve yields $\tau_{out} \sim 25\mu s$. (b) Experimental, and simulated rf single-shot traces of the Q_R with the π pulse applied. (c) Histogram of the CDS amplitude of the S (red) and T_0 (blue) states. The histograms in (b) and (c) are normalized to generate the probability density plot. (d) The measurement fidelity and visibility of the Q_R. The maximum fidelity / visibility is 83% / 65% which is in good agreement with the experimentally acquired visibility shown in Fig. 3.

4.3.2.S2. Magnetic field gradient simulation

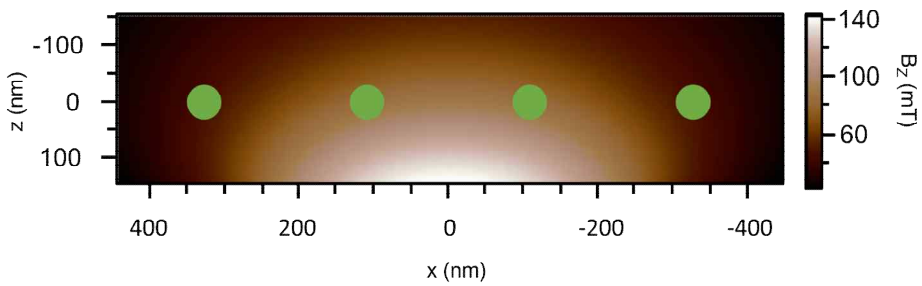

Fig. 2.S2. Simulation of the magnetic field by the micromagnet. The z-component

of the magnetic field around the quantum dots in our device is simulated using the boundary integral method with RADIA [38,39] package. Green dots indicate the quantum dot positions. The fast ΔB_z oscillations shown in Fig. 3 is up to 500MHz corresponding to ΔB_z of 100 mT, and we ascribe this higher-than-expected-ΔB_z to the displacement of the electrons from the expected positions by the confining potential in the few electron regime.

4.3.2.S3. Measurement fidelity analysis

Single-shot traces were numerically simulated following the Morello, A. et al [3], using the experimentally acquired parameters including the tunneling out / in rates, and rf signal contrast. T_1 relaxation time is also taken into account by calculating the relaxation probability $P_{relax} = 1 - \exp(-t_{out} / T_1)$. By varying the amplitude of the numerical noise filter applied to the simulated single-shot traces the numerical simulation reproduce the experimental histogram as shown in Fig. 2(d). As we have detected the events by thresholding CDS amplitude described above, for the readout fidelity analysis the simulated single-shot traces are further processed with the same CDS filter condition. To find the optimal threshold for maximum readout fidelity / visibility the single-shot traces corresponding to the singlet and triplet states were prepared respectively, and histograms were constructed with the peak values of the CDS traces (see inset to Fig. 2(e)). After normalizing the histogram to generate a histogram of probability density, the singlet, and triplet fidelities (F_S, and F_T) were acquired by the following integrations,

$$F_T = \int_{V_T}^{\infty} p_T(V)\,\mathrm{dV}$$

$$F_S = \int_{-\infty}^{V_T} p_S(V)\,\mathrm{dV}$$

and the visibility is defined by $V = F_T + F_S - 1$. $p_T(V)$, and $p_S(V)$ are the probability density of the triplet and singlet outcomes at V which can be obtained from the CDS histogram. By optimizing the threshold voltage V_T we acquire the maximum measurement fidelity and visibility.

4.3.2.S4. Expected fidelity with direct peak detection

The measurement fidelity and visibility are calculated for the direct peak detection scheme to explicitly show that the use of FPGA rather than CDS technique may extend the measurement fidelity and visibility with the same experimental parameters. Following the Morello et al[3], single-shot traces were first simulated with the experimental parameters, and instead of passing through additional numerical CDS filter, the peak value (the minimum value) from each rf single-shot trace is sampled for 10,000 traces to construct the histogram shown in Fig. 2.S4(a) and 2.S4(c). Because the short peaks or the full signal contrast cannot be perfectly detected with the CDS due to its limited bandwidth, the histograms of the S and T_0 are more clearly separated in Fig. 2.S4, which naturally leads to higher fidelity and visibility as in Fig. 2.S4(b), and 2.S4(d) respectively for Q_L and Q_R. The measurement fidelities (97% for Q_L, and 93% for Q_R) are limited by the T_1 relaxation time, which we claim to be a rather conservative calculation since we use the T_1 time measured at ε near (1,1)T_0-(2,0)T_0 anti-crossing. The tunneling rates may be tuned faster in the case where the CDS is not utilized, and it will be less likely for the relaxation to take place before tunneling events, which will extend the fidelity further. Experimentally, direct peak detection described above is possible with the usage of FPGA, where the peak value from a single-shot trace can be detected by setting appropriate threshold levels.

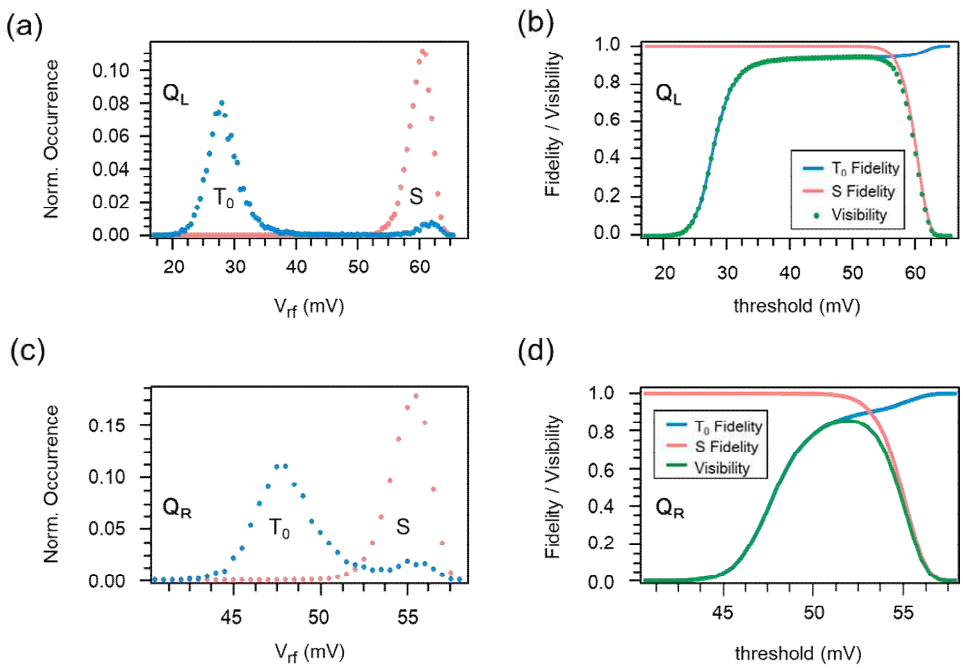

Fig. 2.S4. (a) ((c)) Histogram constructed directly from the peak values of the Q_L (Q_R) single-shot traces without the CDS. The histograms are normalized to yield the probability density histogram. (b) ((d)) Fidelity and visibility acquired from the histogram (a) ((c)). The maximum measurement fidelity / visibility of the Q_L (Q_R) can reach 97% / 94% (93% / 86%), by optimizing the thresholding voltage.

4.3.3. High-visibility two-axis control of two ST_0 qubits

We now demonstrate high-visibility coherent qubit operations with the EST single-shot readout. The panels in Fig. 3 show the high-visibility two-axis control of Q_L (Figs. 3(a)–(c)) and Q_R (Figs. 3(d)–(f)) under large ΔB_z recorded with a single rf-set. For the ΔB_z oscillations (Figs. 3(a), 3(d)), the I – W – O – W – R with the period of 150 μs (Fig. 3(a), top panel) was applied, and the evolution time at O was varied from 0 to 10 ns. Each trace in Figs. 3(a) and 3(d) is the average of 50 repeated measurements with 2000 shots per point, which takes over 5 min; thus, we expect an ensemble-averaged coherence time of ST_0 qubit oscillation T_2* in the order of 15 ns

[1], limited by nuclear bath fluctuation. We clearly observe coherent oscillations of Q_L (Q_R) with ~81% (~64%) visibility, which is consistent with the results of the numerical simulation reported in Fig. 2(e). Under the large ΔB_z of 100 (80) mT, corresponding to an oscillation frequency of 500 (400) MHz, we expect the control fidelity of the π pulse to reach up to 99.63% (99.23%) for Q_L (Q_R) assuming gaussian decay, even with the ensemble-averaged T_2* ~ 15 ns; thus, one can neglect the effect of the limited control fidelity on the visibility. As discussed above, with the experimental conditions considered in this study, the visibility for both Q_L and Q_R is limited by the electronic bandwidth owing to the CDS technique used. For Q_R, tuning to an even longer τ_{out} of 25 μs was necessary to account for the reduced rf-set sensor's signal contrast to farther QDs, for which the final visibility is approximately 64%. However, as shown in section 4.3.2.S4, the visibility of the further QDs can be easily enhanced to more than 85% by simply improving the electronics of the measurement system, for example, with FPGA programming.

To acquire the 2D plots shown in Figs. 3(b) and 3(e), the typical Ramsey pulse sequence of I – W – O ($\pi/2$) – A_{ex} – O ($\pi/2$) – W – R (Fig. 3(b), top panel) was applied, and the detuning amplitude A_{ex} and evolution time τ_{ex} at the exchange step were varied. The figures show high-visibility quantum oscillation as well as continuous evolution of rotation axis on the Bloch sphere as A_{ex} is varied over different regimes, where T_2* is limited by the charge noise for $J(\varepsilon) > \Delta B_z$ or by fluctuations in ΔB_z for $J(\varepsilon) \sim 0$. The fast Fourier transform (FFT) of the exchange oscillations along the exchange detuning axis (Figs. 3(c) and 3(f)) confirms the control of the ST_0 qubit over the two axes on the Bloch sphere for both Q_L and Q_R, which is consistent with the expected qubit energy splitting (Fig. 3(c), top panel). We emphasize that the measurement of two qubits is possible with one

accompanied rf-set, which can be useful for the linear extension of the ST_0 qubits because the charge sensor does not need to be aligned with the QD array. In this work, we focused on independent two single-qubit gate operation; nevertheless, we expect that long T_1 at EST readout will allow the sequential measurement of two qubit states for a given quantum operation, which, in turn, will allow two qubit correlation measurement, enabling full two qubit state and process tomography in the future. Characterization of the two qubit interaction of ST_0 qubits in the current quadruple dot array, for example by dipole coupling [6,9] or exchange interaction [32], is the subject of current investigations.

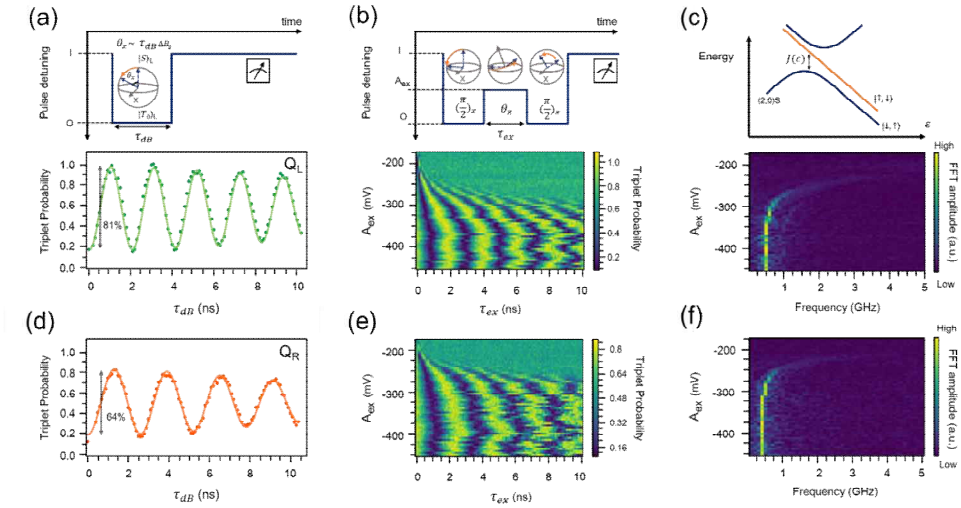

Fig. 3. High-visibility two-axis control of two ST_0 qubits. (a) ((d)) Coherent ST_0 oscillation of Q_L (Q_R) under large ΔB_z. Electronic bandwidth-limited 81% (64%) quantum oscillation visibility is defined by the oscillation amplitude. (b) ((e)) Coherent exchange oscillation and two-axis control of Q_L (Q_R) on the Bloch sphere. The top panel of (b) shows the Ramsey pulse sequence where the first $\pi/2$ pulse induces equal superposition of S and T_0 spin states, and the phase evolution under non-zero $J(\varepsilon)$ is probed by the second $\pi/2$ pulse. By varying the pulse amplitude A_{ex} and the evolution time τ_{ex} at the exchange step, the high-resolution rotation axis evolution and an energy spectrum consistent with the

expected functional form of $J(\varepsilon)$ [29], the schematic of which is shown in the top panel of (c), are confirmed by the fast Fourier transform (FFT) plots in (c) ((f)).

4.4. Methods

4.4.1. Device Fabrication

The quadruple QD device was fabricated on a GaAs/AlGaAs heterostructure with a 2DEG formed 73 nm below the surface. The transport property of the 2DEG shows mobility $\mu = 2.6\times10^{6} cm^{2}V^{-1}s^{-1}$ with electron density $n = 4.6\times10^{11} cm^{-2}$ and temperature T = 4 K. Mesa was defined by the wet etching technique to eliminate the 2DEG outside the region of interest. Ohmic contact was formed through metal diffusion to connect the 2DEG with the electrode on the surface. The depletion gates were fabricated on the surface using standard e-beam lithography and metal evaporation. The QD array axis was oriented parallel to the [011] crystallographic direction of GaAs. Subsequently, the micromagnet was patterned perpendicular to the QD array using standard e-beam lithography, and a Ni 10 nm/Co 200 nm/Au 5 nm was deposited using metal evaporation.

4.4.2. Measurement

The experiments were performed on a quadruple QD device placed on the 20 mK plate in a commercial dilution refrigerator (Oxford instruments, Triton-500). Rapid voltage pulses generated by Agilent M8195A arbitrary waveform generator (65 GSa/s sampling rate) and stable dc voltages generated by battery-operated voltage sources (Stanford Research Systems SIM928) were applied through bias-tees (picosecond Pulselabs 5546) in the dilution refrigerator before applying the metal gates. An LC-resonant tank circuit was attached to one of the ohmic contacts near the rf-set with a resonance frequency of ~110 MHz for homodyne detection. The reflected

rf-signal was first amplified at 4 K with a commercial cryogenic amplifier (Caltech Microwave Research, CITLF2) and then further amplified at room temperature with home-made low-noise amplifiers. Signal demodulation was performed with an ultra-high-frequency lock-in amplifier (Zurich instrument UHFLI), and the demodulated amplitude was processed using a boxcar integrator built in the UHFLI for CDS. The CDS peaks were counted with an external photon counter (Stanford Research, SR400). The pulse parameters could be rapidly swept via a hardware looping technique, which enabled fast acquisition of the ΔB_z oscillations. In section 4.4.2.S1, we show the details of the measurement setup, CDS technique, and signal analysis.

4.4.2.S1. Measurement setup

A rf-single electron transistor (rf-set) sensor is operated to detect the charge states of the ST_0 qubits in our device. For the rf-reflectometry, impedance matching tank circuit as shown in Fig. 2.S1 is attached to the rf-ohmic contact of the device, and the 100 pF capacitor is connected in series to the other ohmic contact (depicted on the micromagnet) to serve as a rf-ground. With the inductor value L = 1500 nH and the parasitic capacitance C_p = 1.4 pF of the circuit board, the resonance frequency is about 110MHz, and the impedance matching occurs at rf-set sensor resistance approximately 0.5 h/e^2 where h is Plank's constant and e is the electron charge. A commercial high frequency lock-in amplifier (Zurich Instrument, UHFLI) is used as the carrier generator, rf demodulator for the homodyne detection, and further signal processing such as gated integration and timing marker generation. Carrier power of -40dBm power is generated at room temperature and attenuated through the attenuators and the directional coupler by -50 dB in the input line. The reflected signal is first amplified by 25 dB with commercial cryogenic amplifier (Caltech Microwave Research Group, CITLF2), and further amplified by 50 dB at room temperature using

a home-made low-noise rf amplifier. Demodulated signal is acquired with a data acquisition card (National Instruments, NI USB-9215A) for raster scanning and also boxcar-averaged with the gated integrator module in the UHFLI for the correlated double sampling described above. For single-shot readout, the CDS output is counted with a high-speed commercial photon counter (Stanford Research Systems, SR400 dual gated photon counter). A commercial multichannel scalar (Stanford Research Systems, SR430 multichannel scaler & average) is also used for time correlated pulse counting for tunneling rate calibration.

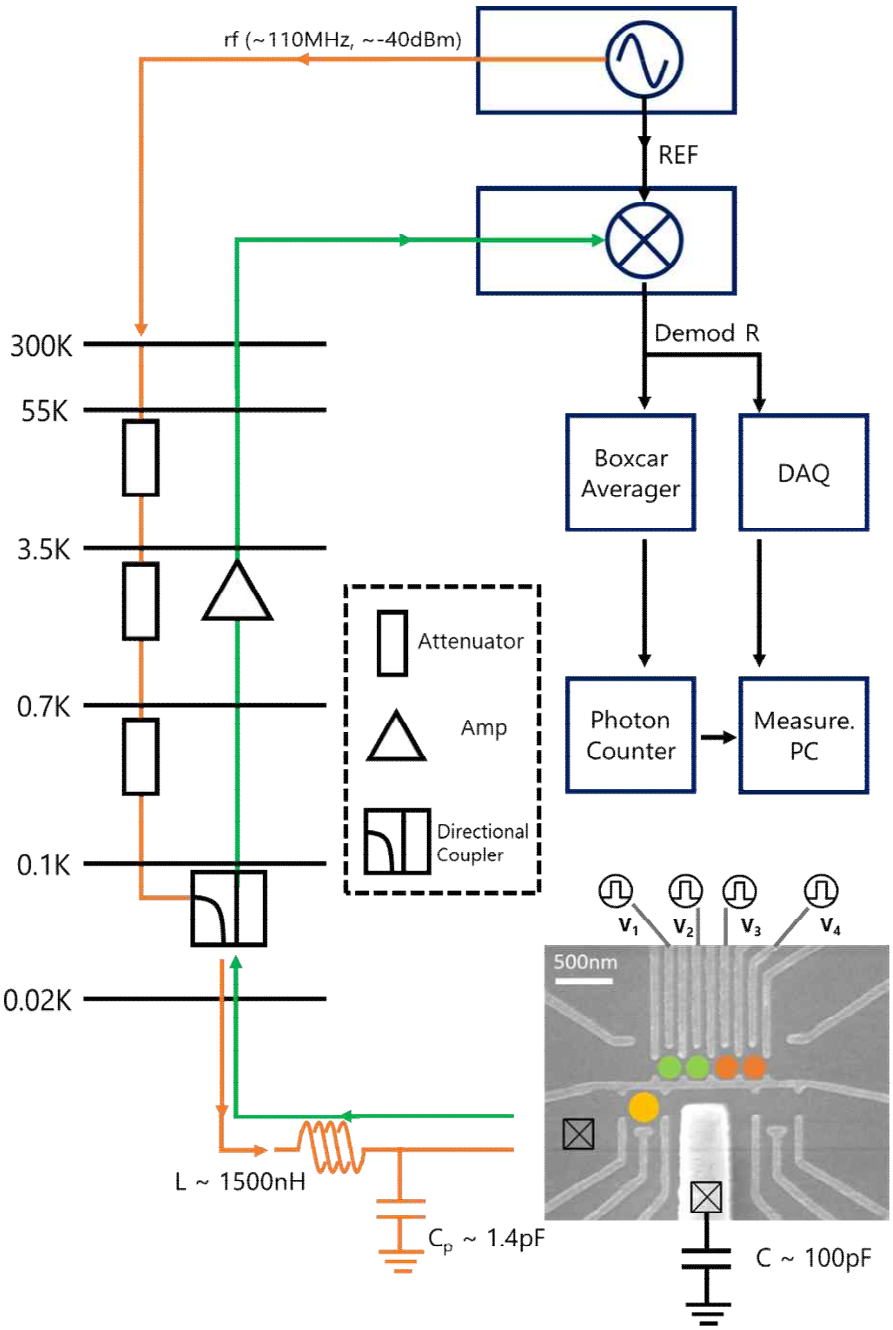

Fig. 2.S1. The measurement setup for radio frequency (rf)-reflectometry, and the signal block diagram. Impedance matching tank-circuit (L~1500 nH, C_p ~ 1.4pF) is attached to the rf-set sensor Ohmic contact for homodyne detection. Orange (green) line indicates the input (reflected) signal. Reflected signal is demodulated and processed for single-shot event counting as shown in the block diagram.

4.5. Conclusion

High-visibility readout of the ST_0 qubit at large ΔB_z is necessary for high-fidelity ST_0 qubit operations [6,36]. We performed high-visibility single-shot readout of two adjacent ST_0 qubits at ΔB_z of 100 mT by direct EST with one rf-set. No mixing between T_0 and (1,1)S state was observed at the EST readout point, which would allow sequential readout of multiple arrays of qubits due to the long T_1. Full one-electron signal difference discriminates the S and T_0 states compared to other readout methods where the dipolar charge difference is measured to readout the ST_0 qubit states [12,15]. This feature can be especially useful for scaling up the ST_0 qubits for the following reasons: 1) the large signal contrast can result in high visibility and low measurement error, and 2) the sensor does not need to be aligned along the QD array. Especially for GaAs spin qubits, high-visibility ST_0 qubit readout allows fast nuclear-spin fluctuation measurements, which will enable accurate feedback/stabilization of the nuclear spin bath for high-fidelity qubit control [2,25,36]. Furthermore, our method does not require additional metastable states [14,16,40] or pulsing sequences for high-fidelity measurements at large ΔB_z [13,15], showing that the experimental complexity is greatly reduced. EST readout of ST_0 qubits in nuclear spin-free systems, including Si, may also enhance the measurement fidelity by providing even longer T_1 for electron spins [7,41,42].

Because the highest bandwidth potential of rf-reflectometry cannot be fully exploited with the CDS technique used in this study, we expect that the use of FPGA to detect the peaks from the bare rf demodulated single-shot traces will enhance the visibility to at least 93% (86%) for Q_L (Q_R). The use of FPGA programming will also allow faster nuclear environment Hamiltonian learning [36], which can be useful in, for example, studying the time-correlation of nuclear spin bath fluctuations at different QD sites. We

roughly estimated the thermal excitation arising from the relatively high electron temperature of 230 mK (see 4.3.1.S1), and the colored low-frequency electronic noise present in the current setup [43] reduced the visibility by a few percent, which can explain the slight disagreement between the experimental and calculated visibility. In the future, we plan to improve the performance by adopting an FPGA-based customized measurement, reducing electron temperature, and further optimizing the electronic signal path. However, even with the current limitations, the achieved visibility of 81% for ST_0 qubits at large ΔB_z shows potential to realize high-fidelity quantum measurements in scalable and individually addressable multiple QD arrays in semiconductors.

4.6. References

[1] J. R. Petta, A. C. Johnson, J. M. Taylor, E. A. Laird, A. Yacoby, M. D. Lukin, C. M. Marcus, M. P. Hanson, and A. C. Gossard, *Coherent manipulation of coupled electron spins in semiconductor quantum dots*, Science **309,** 2180 (2005).

[2] S. Foletti, H. Bluhm, D. Mahalu, V. Umansky, and A. Yacoby, *Universal quantum control of two-electron spin quantum bits using dynamic nuclear polarization*, Nat. Phys. **5,** 903 (2009).

[3] A. Morello *et al.*, *Single-shot readout of an electron spin in silicon*, Nature **467,** 687 (2010).

[4] D. M. Zajac, A. J. Sigillito, M. Russ, F. Borjans, J. M. Taylor, G. Burkard, and J. R. Petta, *Resonantly driven CNOT gate for electron spins*, Science **359,** 439 (2018).

[5] D. Kim, D. R. Ward, C. B. Simmons, D. E. Savage, M. G. Lagally, M. Friesen, S. N. Coppersmith, and M. A. Eriksson, *High-fidelity resonant gating of a silicon-based quantum dot hybrid qubit*, Npj Quantum Information **1,** 6 (2015).

[6] J. M. Nichol, L. A. Orona, S. P. Harvey, S. Fallahi, G. C. Gardner, M. J. Manfra, and A. Yacoby, *High-fidelity entangling gate for double-quantum-dot spin qubits*, Npj Quantum Information **3,** 5 (2017).

[7] J. Yoneda *et al.*, *A quantum-dot spin qubit with coherence limited by charge noise and fidelity higher than 99.9%*, Nat. Nanotech. **13,** 102 (2018).

[8] D. Kim *et al.*, *Quantum control and process tomography of a semiconductor quantum dot hybrid qubit*, Nature **511,** 70 (2014).

[9] M. D. Shulman, O. E. Dial, S. P. Harvey, H. Bluhm, V. Umansky, and A. Yacoby, *Demonstration of Entanglement of Electrostatically Coupled Singlet-Triplet Qubits*, Science **336,** 202 (2012).

[10] J. M. Elzerman, R. Hanson, L. H. W. van Beveren, B. Witkamp, L. M. K. Vandersypen, and L. P. Kouwenhoven, *Single-shot read-out of an individual electron spin in a quantum dot*, Nature **430,** 431 (2004).

[11] T. Meunier, K. J. Tielrooij, I. T. Vink, F. H. L. Koppens, H. P. Tranitz, W. Wegscheider, L. P. Kouwenhoven, and L. M. K. Vandersypen, *High fidelity measurement of singlet-triplet state in a quantum dot*, Physica Status Solidi B-Basic Solid State Physics **243,**

3855 (2006).
[12] C. Barthel, D. J. Reilly, C. M. Marcus, M. P. Hanson, and A. C. Gossard, *Rapid Single-Shot Measurement of a Singlet-Triplet Qubit*, Phys. Rev. Lett. **103,** 4 (2009).
[13] P. Harvey-Collard *et al.*, *High-Fidelity Single-Shot Readout for a Spin Qubit via an Enhanced Latching Mechanism*, Physical Review X **8,** 11 (2018).
[14] T. Nakajima *et al.*, *Robust Single-Shot Spin Measurement with 99.5% Fidelity in a Quantum Dot Array*, Phys. Rev. Lett. **119,** 6 (2017).
[15] L. A. Orona, J. M. Nichol, S. P. Harvey, C. G. L. Bottcher, S. Fallahi, G. C. Gardner, M. J. Manfra, and A. Yacoby, *Readout of singlet-triplet qubits at large magnetic field gradients*, Phys. Rev. B **98,** 5 (2018).
[16] M. A. Broome, T. F. Watson, D. Keith, S. K. Gorman, M. G. House, J. G. Keizer, S. J. Hile, W. Baker, and M. Y. Simmons, *High-Fidelity Single-Shot Singlet-Triplet Readout of Precision-Placed Donors in Silicon*, Phys. Rev. Lett. **119,** 5 (2017).
[17] T. F. Watson *et al.*, *A programmable two-qubit quantum processor in silicon*, Nature **555,** 633 (2018).
[18] A. C. Johnson, J. R. Petta, C. M. Marcus, M. P. Hanson, and A. C. Gossard, *Singlet-triplet spin blockade and charge sensing in a few-electron double quantum dot*, Phys. Rev. B **72,** 7 (2005).
[19] A. C. Johnson, J. R. Petta, J. M. Taylor, A. Yacoby, M. D. Lukin, C. M. Marcus, M. P. Hanson, and A. C. Gossard, *Triplet-singlet spin relaxation via nuclei in a double quantum dot*, Nature **435,** 925 (2005).
[20] J. R. Petta, A. C. Johnson, A. Yacoby, C. M. Marcus, M. P. Hanson, and A. C. Gossard, *Pulsed-gate measurements of the singlet-triplet relaxation time in a two-electron double quantum dot*, Phys. Rev. B **72,** 4 (2005).
[21] C. Volk *et al.*, *Loading a quantum-dot based "Qubyte" register*, Npj Quantum Information **5,** 8 (2019).
[22] A. R. Mills, D. M. Zajac, M. J. Gullans, F. J. Schupp, T. M. Hazard, and J. R. Petta, *Shuttling a single charge across a one-dimensional array of silicon quantum dots*, Nat. Commun. **10,** 6 (2019).
[23] F. Martins, F. K. Malinowski, P. D. Nissen, S. Fallahi, G. C. Gardner, M. J. Manfra, C. M. Marcus, and F. Kuemmeth, *Negative Spin Exchange in a Multielectron Quantum Dot*, Phys. Rev. Lett. **119,** 5 (2017).
[24] J. R. Petta, J. M. Taylor, A. C. Johnson, A. Yacoby, M. D. Lukin, C. M. Marcus, M. P. Hanson, and A. C. Gossard, *Dynamic nuclear polarization with single electron spins*, Phys. Rev. Lett. **100,** 4 (2008).
[25] H. Bluhm, S. Foletti, D. Mahalu, V. Umansky, and A. Yacoby, *Enhancing the Coherence of a Spin Qubit by Operating it as a Feedback Loop That Controls its Nuclear Spin Bath*, Phys. Rev. Lett. **105,** 4 (2010).
[26] J. Yoneda *et al.*, *Robust micromagnet design for fast electrical manipulations of single spins in quantum dots*, Applied Physics Express **8,** 4 (2015).
[27] T. Ito *et al.*, *Four single-spin Rabi oscillations in a quadruple quantum dot*, Applied Physics Letters **113,** 5 (2018).
[28] A. J. Sigillito, J. C. Loy, D. M. Zajac, M. J. Gullans, L. F. Edge, and J. R. Petta, *Site-Selective Quantum Control in an Isotopically Enriched Si-28/Si0.7Ge0.3 Quadruple Quantum Dot*, Physical Review Applied **11,** 6 (2019).
[29] O. E. Dial, M. D. Shulman, S. P. Harvey, H. Bluhm, V. Umansky, and A. Yacoby, *Charge Noise Spectroscopy Using Coherent Exchange Oscillations in a Singlet-Triplet Qubit*, Phys. Rev. Lett. **110,** 5 (2013).
[30] S. Chesi, Y. D. Wang, J. Yoneda, T. Otsuka, S. Tarucha, and D. Loss, *Single-spin manipulation in a double quantum dot in the field of a micromagnet*, Phys. Rev. B **90,** 12 (2014).
[31] M. Pioro-Ladriere, T. Obata, Y. Tokura, Y. S. Shin, T. Kubo, K. Yoshida, T. Taniyama, and S. Tarucha, *Electrically driven single-electron spin resonance in a slanting Zeeman field*, Nat. Phys. **4,** 776 (2008).

[32] A. Noiri *et al.*, *A fast quantum interface between different spin qubit encodings*, Nat. Commun. **9,** 7 (2018).
[33] D. J. Reilly, C. M. Marcus, M. P. Hanson, and A. C. Gossard, *Fast single-charge sensing with a rf quantum point contact*, Applied Physics Letters **91,** 3 (2007).
[34] C. Barthel, M. Kjaergaard, J. Medford, M. Stopa, C. M. Marcus, M. P. Hanson, and A. C. Gossard, *Fast sensing of double-dot charge arrangement and spin state with a radio-frequency sensor quantum dot*, Phys. Rev. B **81,** 4 (2010).
[35] R. Hanson, L. H. W. van Beveren, I. T. Vink, J. M. Elzerman, W. J. M. Naber, F. H. L. Koppens, L. P. Kouwenhoven, and L. M. K. Vandersypen, *Single-shot readout of electron spin states in a quantum dot using spin-dependent tunnel rates*, Phys. Rev. Lett. **94,** 4 (2005).
[36] M. D. Shulman, S. P. Harvey, J. M. Nichol, S. D. Bartlett, A. C. Doherty, V. Umansky, and A. Yacoby, *Suppressing qubit dephasing using real-time Hamiltonian estimation*, Nat. Commun. **5,** 6 (2014).
[37] E. Kawakami *et al.*, *Gate fidelity and coherence of an electron spin in an Si/SiGe quantum dot with micromagnet*, Proceedings of the National Academy of Sciences of the United States of America **113,** 11738 (2016).
[38] P. Elleaume, O. Chubar, and J. Chavanne, in *17th Particle Accelerator Conference*Vancouver, Canada, 1997), pp. 3509.
[39] O. Chubar, P. Elleaume, and J. Chavanne, *A three-dimensional magnetostatics computer code for insertion devices*, Journal of Synchrotron Radiation **5,** 481 (1998).
[40] S. A. Studenikin, J. Thorgrimson, G. C. Aers, A. Kam, P. Zawadzki, Z. R. Wasilewski, A. Bogan, and A. S. Sachrajda, *Enhanced charge detection of spin qubit readout via an intermediate state*, Applied Physics Letters **101,** 3 (2012).
[41] W. Huang *et al.*, *Fidelity benchmarks for two-qubit gates in silicon*, Nature **569,** 532 (2019).
[42] E. Kawakami *et al.*, *Electrical control of a long-lived spin qubit in a Si/SiGe quantum dot*, Nat. Nanotech. **9,** 666 (2014).
[43] W. Jang, M. K. Cho, M. Lee, C. Hong, J. Kim, H. Jung, Y. Chung, V. Umansky, and D. Kim, *Fast raster scan multiplexed charge stability measurements toward high-throughput quantum dot array calibration*, Applied Physics Letters **114,** 5 (2019).

Chapter 5. Approaching ideal visibility in singlet-triplet qubit operations using energy selective tunneling-based Hamiltonian estimation

Jehyun Kim[1†], Jonginn Yun[1†], Wonjin Jang[1†], Hyeongyu Jang[1], Jaemin Park[1], Youngwook Song[1], Min-Kyun Cho[1], Sangwoo Sim[1], Hanseo Sohn[1], Hwanchul Jung[2], Vladimir Umansky[3], and Dohun Kim[1]*

[1]*Department of Physics and Astronomy, and Institute of Applied Physics, Seoul National University, Seoul 08826, Korea*

[2] *Department of Physics, Pusan National University, Busan 46241, Korea*

[3]*Braun Center for Submicron Research, Department of Condensed Matter Physics, Weizmann Institute of Science, Rehovot 76100, Israel*

[†]*These authors contributed equally to this work.*

**Corresponding author:* dohunkim@snu.ac.kr

This work was published in "Physical Review Letters"

5.1. Abstract

We report energy-selective tunneling readout-based Hamiltonian parameter estimation of a two-electron spin qubit in a GaAs quantum dot array. Optimization of readout fidelity enables a single-shot measurement time of 16 μs on average, with adaptive initialization and efficient qubit frequency estimation based on real-time Bayesian inference. By triggering the operation sequence conditional on the frequency detected in the probe step, we observed a 40-fold increase in coherence time without resorting to dynamic nuclear polarization. We also demonstrate active frequency feedback with quantum oscillation visibility, single-shot measurement fidelity, and state initialization fidelity up to 97.7%, 99%, and over 99.7%, respectively. By pushing the sensitivity of the energy-selective tunneling-based spin-to-charge conversion to the limit, the technique is useful for advanced quantum control protocols such as error mitigation schemes,

where fast qubit parameter calibration with a large signal-to-noise ratio is crucial.

5.2. Introduction

The efficient and precise characterization of a quantum system is important for building scalable quantum technologies that are robust to noise stemming from a fluctuating environment [1,2]. Estimating Hamiltonian parameters faster than the characteristic noise fluctuation time scale is essential, where knowledge gained from the measurement is used for correcting, for example, control errors due to unknown qubit frequencies [2-4]. Active measurement-based feedback for example is used to enhance quantum sensing [5,6]. For semiconductor quantum dot (QD)-based spin qubit platforms, Hamiltonian parameter estimation applied to GaAs has shown that the effect of quasi-static nuclear spin fluctuation can be strongly suppressed for both single spin [7] and singlet-triplet qubits [2]. While the development of spin qubits in nuclear noise-free group-IV materials such as ^{28}Si shows impressive progress in increasing single spin qubit coherence times [8,9], two-qubit control fidelity is often impeded by charge noise, which is also often sufficiently non-Markovian [10] and hence suppressible. Thus, fast Hamiltonian learning methods are expected to be used for a wide range of materials in noisy intermediate-scale quantum systems.

The fast single-shot measurement of qubits with high fidelity is a prerequisite for enabling Hamiltonian estimation. Semiconductor spin qubit devices mostly utilize a nearby charge sensor, where spin states are distinguished via spin to charge conversion mechanisms such as energy selective tunneling (EST) [11,12] or Pauli spin blockade (PSB) [13]. While both mechanisms are applicable for the detection of single spin [11], singlet-triplet (ST_0) [13], and exchange only qubits [14], PSB-based readout has been predominantly used for real-time Hamiltonian estimation owing to its

deterministic readout time and fast initialization capability, providing a repetition period down to a few μs [15]. Depending on the device geometry and relaxation time scale, however, direct application of PSB often suffers from small signal contrast due to sub-optimal sensor position relative to double quantum dot (DQD) or fast relaxation at the readout condition due to large magnetic field difference-induced singlet state tunneling or the effect of spin-orbit coupling [16]. Variants of PSB-based readout have been developed using electron latching mechanisms in sufficiently isolated quantum dots [17,18] or by mapping fragile triplet-zero states to the states outside the qubit space [19], circumventing some of the PSB-readout's known disadvantages. For Si devices, high readout visibility has been demonstrated using both PSB and EST readout owing to relatively long relaxation time compared to that of GaAs devices [20-22]. However, so far the experiments using GaAs devices showed intermediate quantum oscillation visibility below 80% using PSB readout.

The EST-based single-shot readout, on the other hand, guarantees a signal contrast corresponding to a full electron charge and long relaxation time [23,24]. As the Hamiltonian learning efficiency is directly affected by the ideality of the likelihood function, the large signal-to-noise ratio (SNR) of the EST readout at a given sensor integration time can potentially be used for real-time Hamiltonian parameter estimation. Because the EST readout suffers from the intrinsically probabilistic nature of electron tunneling, requiring a longer waiting time than the PSB readout [25], it is important to determine whether the current state-of-the-art sensitivity of the RF-charge sensor can provide an EST-based readout that is sufficiently fast and simultaneously has a large SNR to enable efficient qubit frequency estimation on the fly.

In this study, we demonstrate real-time Hamiltonian parameter estimation by EST-based single-shot readout with sub-MHz accuracy in qubit frequency verified by observing over a 40-fold increase in coherence time

T_2* compared with bare evolution which is known to be on the order of 20 ns in GaAs [13]. With real-time frequency selection and active frequency feedback, the single-qubit operation performance in terms of initialization, manipulation, and measurement fidelity is one of the best figures reported thus far for semiconductor spin qubits, providing a promising route for applying the EST-based single-shot readout method to various qubit operations.

5.3. Results

5.3.1. Introduction of Bayesian estimator for qubit measurement

The quantum system that we study is an ST_0 qubit with a basis state singlet $|S\rangle$ and triplet-zero $|T_0\rangle$, which is formed by two gate-defined lateral QDs. Fig. 1(a) shows a scanning electron microscope image of a quadruple quantum dot device similar to the one we measured. Au/Ti gate electrodes were deposited on top of the GaAs/AlGaAs heterostructure, where a 2D electron gas is formed $70\ \text{nm}$ below the surface. Focusing on the DQD denoted by green circles in Fig. 1(a), high-frequency voltage pulses combined with DC voltages through bias tees are input to gates V_1, V_2, and V_M to control the chemical potential and inter-dot tunnel rates, while the gates that are irrelevant to this experiment are grounded. Fast RF-reflectometry was performed by injecting a carrier frequency of ≈ 125 MHz with an estimated power of -100 dBm at the Ohmic contacts and monitoring the reflected power through homodyne detection. The device was operated in a dilution refrigerator with base temperature ≈ 7 mK and at 0.5 to 0.7 T of an external magnetic field H_{ext} applied in the direction shown in Fig. 1(a). The measured electron temperature is ≈ 72 mK (see 5.3.1.S1).

The qubit Hamiltonian is given by $H = \frac{J(\varepsilon)}{2}\sigma_z + \frac{\Delta B_z}{2}\sigma_x$, where $J(\varepsilon)$ is the exchange splitting between states $|S\rangle$ and $|T_0\rangle$ controlled by

potential detuning ε, $\sigma_{i=x,y,z}$ is the Pauli matrix, and ΔB_z is the magnetic field difference between QDs set by the hyperfine interaction with the host Ga and As nuclei. We adopted units where $g^*\mu_B/h$ = 1, in which $g^* \approx -0.44$ is the effective gyromagnetic ratio in GaAs, μ_B is the Bohr magneton, and h is Planck's constant. With the quantum control provided by rapidly turning on and off $J(\varepsilon)$, the main task is to estimate ΔB_z, which varies randomly in time owing to statistical fluctuations of the nuclei. The basic idea of the Bayesian inference is to update one's knowledge about Hamiltonian parameter (update of the probability distribution) by comparing the measurement results with the qubit's expected phase oscillation behavior for a certain evolution time under the known Hamiltonian form (likelihood function). Based on the single-shot projective measurement of the time evolution of the qubit around the x-axis on the Bloch sphere for evolution time $t_k = 4k$ ns (Larmor oscillation), Bayesian inference is performed by the following rule up to a normalization constant [2]:

$$P(\Delta B_z | m_N, m_{N-1}, \ldots m_1) = P_0(\Delta B_z)\prod_{k=1}^{N}\frac{1}{2}[1 + r_k(\alpha + \beta\cos(2\pi\Delta B_z t_k))] \quad (1)$$

where N is the number of single-shot measurements per Hamiltonian estimation, $P_0(\Delta B_z)$ is the uniform initial distribution, r_k =1(-1) for measurement result $m_k = |S\rangle(|T_0\rangle)$, and α (β) is the parameter determined by the axis of rotation on the Bloch sphere (oscillation visibility). After the Nth single-shot measurement and estimation, the Bayesian estimator finds the value of ΔB_z where the posterior distribution $P(\Delta B_z | m_N, m_{N-1}, \ldots m_1)$ is the maximum.

In the likelihood function $\frac{1}{2}[1 + r_k(\alpha + \beta\cos(2\pi\Delta B_z t_k)]$, ideally, α =0 and β=1. Fig. 1(b) shows the simulation results of the Bayesian estimator's performance, which is evaluated by the root mean squared error between the

true and estimated ΔB_z. Compared to the low-visibility case ($\beta = 0.5$), corresponding to a large measurement error due to, for example, a small SNR or fast state relaxation, the high-visibility case ($\beta = 0.9$) shows a large improvement in the rate of convergence to the true ΔB_z, reaching sub-MHz accuracy in less than $N = 70$. To date, Bayesian estimations of quantum dot spin qubits have been performed with intermediate visibility ($\beta \sim 0.7$) [2,3] requiring $N > 120$ for practical Hamiltonian estimation. Below, we show that the EST readout indeed provides β reaching unity enabling efficient frequency detection and feedback.

By dividing the experimental sequence into probe and operation steps, Fig. 1(c) shows a schematic block diagram and an example scope trace. We set the integration time of the RF demodulator $t_{\mathrm{int}} = 200$ ns, at which SNR = 9.2 (see 5.3.1.S2). The single-shot measurement time was set to 15 μs, during which the dot-to-reservoir tunnel rate tuned to the order of 1 MHz ensures that a tunnel-out event occurs for the state $|T_0\rangle$. For the probe sequence, we diabatically pulse the charge configuration from (2,0) to (1,1), corresponding to rapidly turning off J. In addition, the calculation time according to Eq. (1) is $\approx 10\ \mu s$ after the kth measurement. For the operation, there are two types of modes. The first is heralded mode where the operation is conditionally triggered only when the estimated qubit frequency in the probe step falls within a preset tolerance $\delta(\Delta B_z)_{\mathrm{set}}$ around the target frequency $\Delta B_{z.t}$, resulting in an estimated qubit frequency in the range of $\Delta B_{z,t} \pm \delta(\Delta B_z)_{\mathrm{set}}$. Once a short operation on the order of 20 shots is finished, one has to wait for the next $\Delta B_{z,t} \pm \delta(\Delta B_z)_{\mathrm{set}}$ to happen where waiting time can be long if $\delta(\Delta B_z)_{\mathrm{set}}$ is, for example, less than a few MHz. This operation mode is conceptually similar to Ref. [26] where the main purpose of the Bayesian estimator-based heralding was to effectively suppress thermally induced initialization error. The second is the active

feedback mode where resonant modulation of $J(\varepsilon)$ (Rabi oscillation) is performed using the frequency obtained from the probe step. Here, $\delta(\Delta B_z)_{\mathrm{set}}$ is typically set to more than 70 MHz and the control frequency is actively adjusted so that the waiting time is minimized. For both the probe and operation sequences, we apply an adaptive initialization step [26,27] where the controller triggers the next experiment provided that the last sampled signal value is below the preset threshold value, that is, if the state is $|S\rangle$. Including all the latency components, the repetition period for one probe (operation) step is approximately 26 (16) μs on average (see 5.3.1.S3). Fig. 1(d) shows typical histograms of ΔB_z obtained by repeatedly running the probe step only at different H_{ext}, showing fluctuation about a non-zero mean value. Note that the average ΔB_z depends on H_{ext}. While the exact origin of this is not well understood to date, numerous previous studies in GaAs quantum dot report similar behavior [28,29], and we adjust H_{ext} to set the most probable ΔB_z about 30 MHz (110 MHz) for the heralded (active feedback) mode.

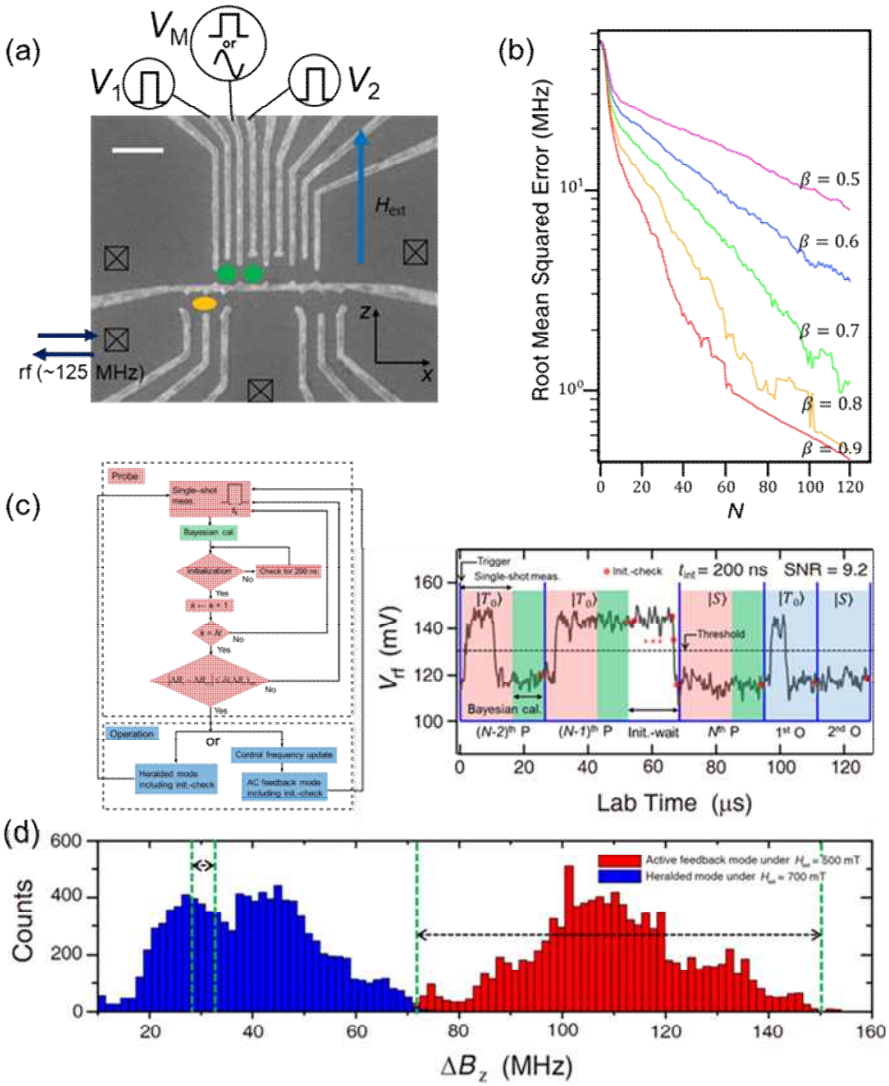

Fig. 1. (a) Scanning electron microscopy image of a device similar to the one used in the experiment. Green (yellow) circles indicate the position of quantum dots for the ST_0 qubit (RF single-electron transistor). An external magnetic field H_{ext} ranging from 0.5 to 0.7 T is applied to the z-axis as indicated by the blue arrow. The scale bar is 500 nm. (b) Root mean squared error of the Bayesian estimator as a function of the number of single-shot measurements N and visibility β. (c) Left panel: block diagram of the experimental procedure including the probe and operation step, where the latter is performed either in heralded or active feedback mode. Right panel: example scope trace of the charge sensor signal during the probe and operation steps. Gray trace: RF-demodulated sensor signal with a signal-to-noise ratio (SNR) = 9.2 at the integration time t_{int} =200 ns. Blue trace: trigger

signals marking the start timings of each probe and operation step. The red dots show the timings of the initialization check sequences. For example, the trace after $(N\text{-}1)^{\text{th}}$ probe shows a rare case that the state initialization by electron tunneling-in event happens to take over 10 μs. (d) Histograms of the qubit frequency ΔB_z obtained by running the probe step 10000 times at two different H_{ext}. For the heralded (active feedback) mode, $\delta(\Delta B_z)_{\text{set}}$ on the order of 1 MHz (few tens of MHz) around an average ΔB_z of 30 (110) MHz was chosen. Green dashed lines indicate a tolerance window $2\delta(\Delta B_z)_{\text{set}}$.

5.3.1.S1. Charge stability diagram and electron temperature

Fig. 1.S1(a) shows the charge stability diagram as a function of gate voltages V_1 and V_2 showing the relevant region for the EST-Bayesian of our ST_0 qubit, where initialization/read-out points in (2,0) and the operation point in (1,1) are depicted as black circles. Fig. 1.S1(b) shows the normalized charge transition signal of the last electron in the left quantum dot as a function of V_1 at the mixing chamber temperature T_{mixing} = 7 mK. This data is fitted to the Fermi-Dirac distribution curve given by $P_e(V_1) = \frac{1}{e^{a(V_1-\text{b})}+1}$, $a = \frac{\alpha}{k_B T_e}$, where a and b are fitting parameters, α is the lever-arm for V_1, k_B is the Boltzmann constant, and T_e is the electron temperature. The $1/a$ extracted at several different T_{mixing} is converted to T_e using $\alpha = 0.0497$ meV/mV obtain from the linear relationship for T_{mixing} > 100 mK as shown in Fig. 1.S1(c) [30]. From a power law $T_e(T_{\text{mixing}}) = (T_S^k + T_{\text{mixing}}^k)^{\frac{1}{k}}$ where T_S is a saturation limit of T_e at T_{mixing} = 0 mK and k is an exponent that depends on the thermalization mechanisms, we estimate T_S = 72 mK and k = 3.35, indicating that Wiedemann-Franz cooling is a dominant cooling mechanism rather than electron-phonon cooling [31].

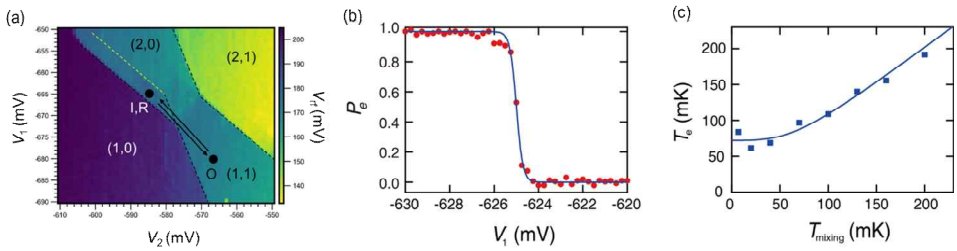

Fig. 1.S1. (a) Charge stability diagram measured at the mixing chamber temperature T_{mixing} = 7 mK. The Yellow dashed line indicates the boundary of the EST-readout window. (b) Normalized charge transition signal from (1,0) to (0,0) as a function of V_1 at T_{mixing} = 7 mK. (c) Electron temperature T_e extracted from broadening of the Fermi-Dirac distribution as a function of T_{mixing} showing estimated T_e of 72 mK at T_{mixing} = 7 mK.

5.3.1.S2. Charge sensitivity

We evaluate the sensitivity of the charge sensor by observing the integration time t_{int} dependence of the signal-to-noise ratio (SNR). We define the SNR by $\Delta V / \sigma$, where ΔV is the sensor signal contrast for a single electron charge transition and σ is the rms noise amplitude at a given t_{int}. The sampling rate of the oscilloscope is set above 200 MHz. As shown in Fig. 1.S2, the SNR is proportional to $\sqrt{t_{int}}$ and we linearly fit the SNR^2 to extract the minimum integration time for achieving SNR = 1, τ_{min} of 2.45 ns [32].

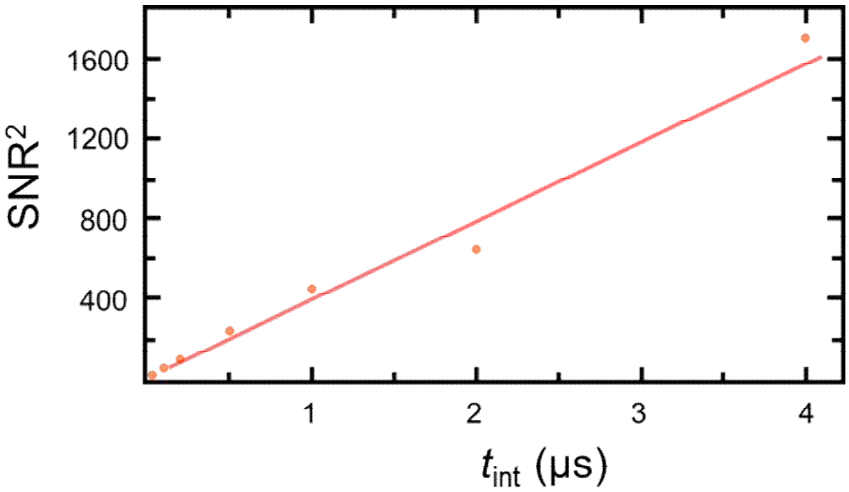

Fig. 1.S2. Signal to noise ratio (SNR) of the RF-single-electron transistor charge sensor as a function of integration time t_{int}. The minimum integration time $\tau_{\min}$ ~ 2.45 ns corresponding to the integration time for achieving the unit SNR is obtained from extrapolating a linear fit to the data.

Using $\tau_{\min}$ as a suitable metric for binary charge detection sensitivity $\mathrm{e}\sqrt{\tau_{\min}}$ [24,33], we compare performances of the recently published works as shown in Table 1.S1 [24,32,34-36] showing that the charge sensitivity achieved in this work is one of the best values available. By comparison, the charge sensor used in this work is more sensitive than a dispersive sensor with a cavity-coupled Josephson parametric amplifier [32] but less sensitive than a similarly prepared RF-SET in a strong quantum dot – sensor capacitive coupling regime [24].

Literature	$\tau_{\min}$ (ns)	Charge Sensitivity ($e\sqrt{\mathrm{Hz}}$)
C. Barthel *et al.* (2009)[Ref. 5]	400	6.32×10^{-4}
C. Barthel *et al.* (2010)[Ref. 6]	23	1.52×10^{-4}
J. Stehlik *et al.* (2015)[Ref. 2]	7	8.37×10^{-5}
D. Keith *et al.* (2019)[Ref. 3]	1.25	3.54×10^{-5}
A. Noiri *et al.* (2020)[Ref. 7]	38	1.95×10^{-4}
Our work (2022)	2.45	4.95×10^{-5}

Table 1.S1. Comparison of minimum integration time $\tau_{\min}$ and corresponding charge sensitivity.

5.3.1.S3. Measurement setup and FPGA implementation

An RF-single electron transistor (RF-SET) sensor is used to detect the quantum states of the ST_0 qubit. An impedance matching tank circuit as shown in Fig. 1.S3 is attached to the RF-ohmic contact of the device. With the inductor value L = 1500 nH and the parasitic capacitance C_p = 1.4 pF of the circuit board, the resonance frequency is about 125 MHz, and the impedance matching occurs when the conductance of the RF-SET sensor is approximately 0.5 h/e^2 where h is Plank's constant and e is the electron charge. A commercial high-frequency lock-in amplifier (Zurich Instrument, UHFLI) is used as the carrier generator, RF-demodulator for the homodyne detection, and further signal processing units such as gated integration and timing marker generation. Carrier power of – 40 dBm is generated at room temperature and further attenuated through the cryogenic attenuators and the directional coupler by -60 dB. The reflected signal is first amplified by 50 dB with a two-stage commercial cryogenic amplifier (Caltech Microwave Research Group, CITLF2 x 2 in series), and further amplified by 25 dB at room temperature using a home-made low-noise RF amplifier.

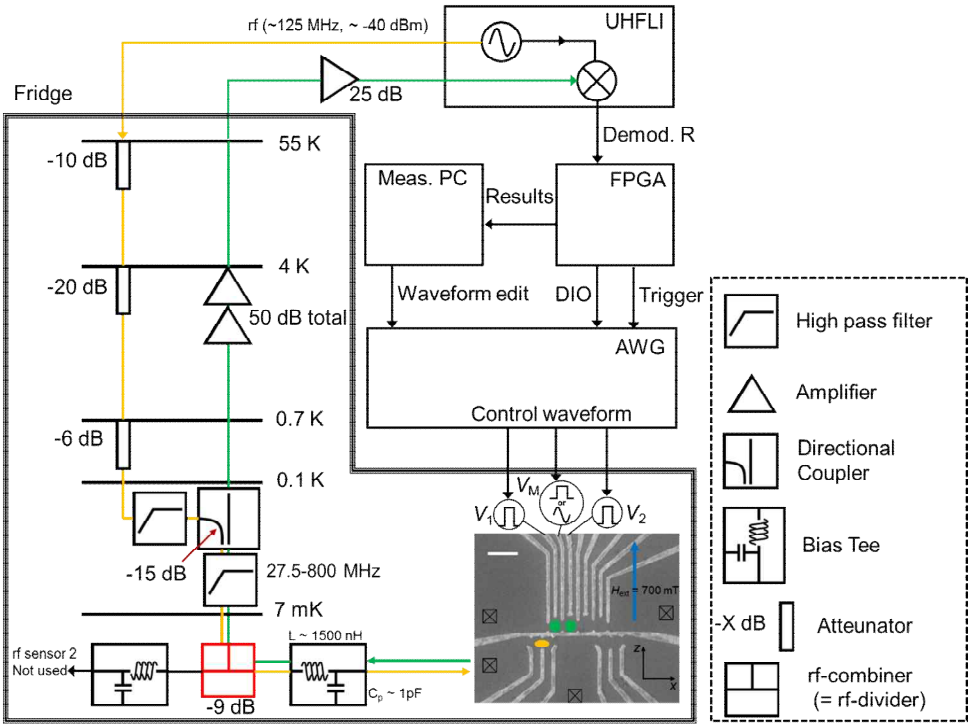

Fig. 1.S3. Measurement setup for radio frequency (RF)-reflectometry and signal block diagram. An impedance matching tank-circuit (L ~1500 nH, C_p ~1.4 pF) is attached to the RF-SET sensor Ohmic contact for homodyne detection. The yellow (green) line indicates the input (reflected) signal. The reflected signal is demodulated in the UHFLI, and subsequently processed in a Field Programmable Gate Array (FPGA) for the EST readout-based Bayesian estimation.

For real-time data processing, we implement a digital logic circuit with a Field Programmable Gate Array board (FPGA, Digilent Zedboard with Zynq-7000 XC7Z020-CLG484). The RF-demodulated analog signal from the UHFLI is input to the 12-bit ad-converter of the FPGA. For single-shot discrimination, the transient tunneling events of the qubit state are thresholded in real-time by comparing the preset threshold value with the data in parallel. The discriminator records bit 1 immediately when data above the threshold value is detected. The bit 0 is recorded when such events did not happen throughout the preset measurement period of 15 μs. The Bayesian estimation after a single shot measurement for the probe step

is carried out by calculating the posterior probability distribution for 512 values of ΔB_z between 10 and 160 MHz. We use a look-up table (LUT) storing all the possible values of the likelihood function in the Block RAM inside the FPGA and design a 512-parallelized calculation module to minimize latency due to data processing. After the calculation, the FPGA follows either of the following steps depending on the operation mode. For the heralded mode operation, the user-defined controller triggers the operation step provided that the ΔB_z calculated after the Nth Bayesian update is in the range $\Delta B_{z,t} \pm \delta(\Delta B_z)_{\mathrm{set}}$ where $\Delta B_{z.t}$ is the target frequency and $\delta(\Delta B_z)_{\mathrm{set}}$ is the preset tolerance. For the active feedback mode, the FPGA converts the estimated ΔB_z into a 9-bit digital signal and sends it to the digital input/output port of the arbitrary waveform generator (Zurich Instruments, HDAWG). The HDAWG applies the square-wave enveloped sinusoidal waveform with the frequency corresponding to the digital value to V_M using the multifrequency modulation function. For both probe and operation steps, an adaptive state initialization is performed by acquiring a 200 ns long sample and thresholding repeatedly until the lastest value falls below the threshold. For the entire data processing, about 60% of LUT and 38% of Flip Flop resources were used.

5.3.2. Optimization of Bayesian estimators

First, we demonstrate the performance of the EST readout-based Bayesian estimator using the heralded mode operation. Fig. 2(a) shows the representative Larmor oscillations measured in the heralded mode, where P_1 is the triplet return probability with $N = 70$, $\Delta B_{z.t} = 30$ MHz, and $\delta(\Delta B_z)_{\mathrm{set}} =$ 0.1 MHz. The measurement of $T_2^*(N)$, extracted by fitting the Larmor oscillations to a Gaussian decay for a given N, reveals the uncertainty of the EST-Bayesian estimation, as shown in Fig. 2(b). The initial increase in

T_2*(N) corresponds to an improvement in the estimation accuracy. Eventually, T_2* reaches an optimal coherence time of over 800 ns near N = 70 and subsequently decreases for N > 80. This reflects the effect of nuclear fluctuation during the long estimation period consistent with the variance of the estimated ΔB_z increasing linearly with time as shown in Fig. 2(c), exhibiting diffusive behavior with diffusivity D = 10.16 kHz^2/μs [2].

Fig. 2(d) shows the $\delta(\Delta B_z)_{\mathrm{set}}$ dependence of the experimental estimation uncertainty extracted from the measured T_2*, $\sigma_{\Delta B_z} = 1/\sqrt{2}\pi T_2^*$ [37]. As we set the tolerance more stringently (smaller $\delta(\Delta B_z)_{\mathrm{set}}$), T_2* increases correspondingly. The residual uncertainty of the EST readout-based Bayesian estimator when $\delta(\Delta B_z)_{\mathrm{set}} = 0$ is approximately 0.25 MHz. Considering that this uncertainty is measured using the Larmor operation step, which takes 0.32 ms (16 μs × 20 shots) after the probe step, it is likely overestimated by the nuclear fluctuation during the operation step. Thus, we conclude that our Hamiltonian estimation scheme enables qubit frequency estimation in 70 shots with an accuracy better than 0.25 MHz. Note also that while the maximum T_2* = 835 ns we observe is less than the PSB readout-based Hamiltonian estimation [2], the actual performance of the PSB and EST readout-based Bayesian estimators is difficult to directly compare so far because the dynamic nuclear polarization [3,38] is not used before the probe step in the current experiment.

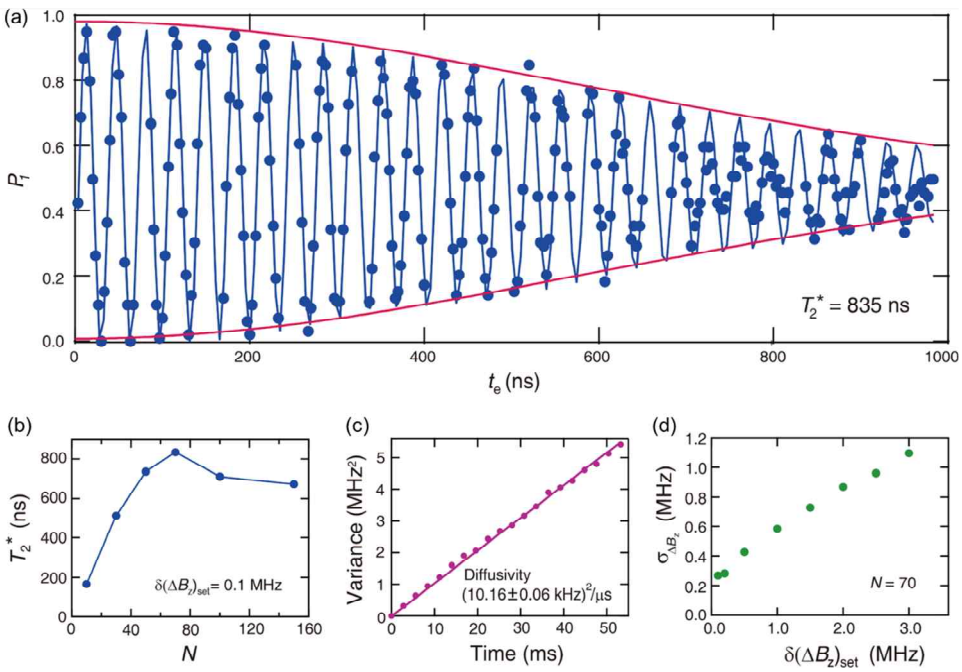

Fig. 2. (a) Representative Larmor oscillations with $N = 70$ showing coherence time $T_2^* = 835$ ns, with a fit to a Gaussian decay function (red envelope and blue oscillatory fit). The triplet return probability P_1 is calculated using 100 shots per point. **(b)** T_2^* as a function of N, showing an optimal $N = 70$, where T_2^* is 835 ns with target frequency $\Delta B_{z,t} = 30$ MHz and tolerance $\delta(\Delta B_z)_{set} = 0.1$ MHz. **(c)** The variance of the continuous EST-Bayesian estimation traces as a function of elapsed lab time, showing a diffusion process of the ΔB_z with the diffusivity $(10.16 \pm 0.06\ \text{kHz})^2 / \mu\text{s}$. **(d)** The experimentally measured uncertainty of the frequency estimation $\sigma_{\Delta B_z}$ as a function of the half-width of the tolerance $\delta(\Delta B_z)_{set}$.

5.3.3. Application of Bayesian estimators for quantum oscillations

We now discuss the application of the EST readout-based Hamiltonian estimation to general single-qubit operations using the heralded (active feedback) mode corresponding to the results in Fig. 3 (Fig. 4). Fig. 3(a) shows coherent Larmor oscillations with $\Delta B_{z,t} = 30$ MHz, where P_1 was measured with 100 shots per point. The oscillation shows the visibility of

approximately 97.7%. Considering the possible deviation of the rotation axis from the x-axis of the Bloch sphere on the order of 1 degree due to residual J and imperfect non-adiabaticity due to finite rise time (~0.4 ns) of the waveform generator, the result shows that the EST readout-based Bayesian method enables accurate qubit frequency estimation and high measurement fidelity at the same time, leading to near ideal visibility. By comparing the oscillation with the numerical simulation, we estimate measurement fidelity of 99% with less than 0.1% initialization errors for the heralded mode (see 5.3.3.S1, see also below for corresponding results for the active feedback mode).

By switching the operation sequence to symmetric barrier-pulse operation, recently demonstrated in Ref. [39], Fig. 3(b) shows representative coherent exchange oscillations with $\Delta B_{z,t}$ = 30 MHz, and J = 75 MHz. Using the same measurement condition in Fig. 3(b), a two-dimensional map of the exchange oscillations is measured as a function of exchange amplitude A_{ex} and exchange duration t_e (Fig. 3(c)), showing the oscillations with a high-quality factor Q. Moreover, $Q(J)$ follows the general trend observed in previous results [39] where Q (T_{decay}) tends to saturate (decrease) at large J owing to the crossover from nuclear noise to electrical noise-limited decoherence. While the maximum Q of ~40 is comparable to that in the previous report [39], our EST readout-based Bayesian method effectively suppresses the ΔB_z fluctuation, leading to the observation of Q > 30 in a wide range of J.

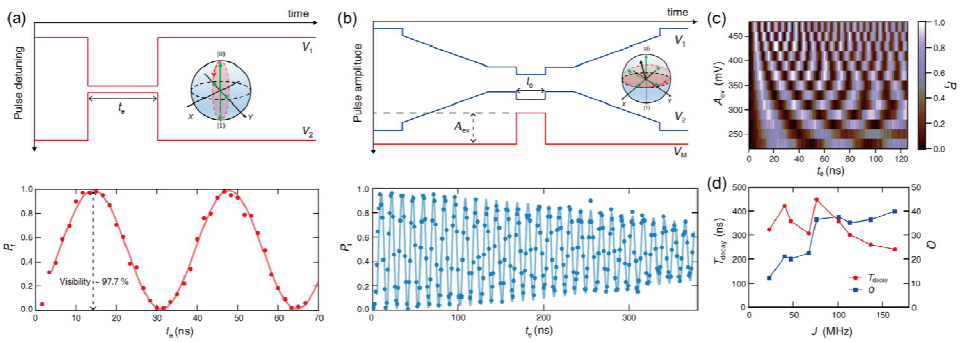

Fig. 3. (a) Top: Pulse sequences applied to gates V_1 and V_2 for coherent Larmor

oscillations measurement. Bottom: Larmor oscillations with visibility higher than 97% (b) Top: Pulse sequence for coherent exchange oscillations. The blue (red) pulse is applied to V_1 and V_2 (V_M) to induce potential detuning (abrupt exchange coupling). Bottom: Corresponding exchange oscillations at J = 75 MHz, $\Delta B_{z,t}$ = 30 MHz showing charge noise-limited coherence time T_{decay} = 450 ns. (c) Exchange oscillations as a function of barrier pulse amplitude A_{ex} and evolution time t_e. (d) T_{decay} and the quality factor Q, defined as the number of oscillations per T_{decay} as a function of exchange coupling J.

5.3.3.S1. Visibility analysis

We analyze the visibility of the quantum oscillation shown in Fig. 3 with a numerical model which includes the thermal tunneling, and the false initialization errors. The analysis essentially amounts to combining the visibility with the computed readout infidelities to extract the relevance of other effects. We first evaluate the tunneling detection infidelity of our readout circuit by numerically simulating the histogram of the RF single-shot traces [23,40]. Following the Ref. [23], we fit the numerical histogram obtained from the simulated traces to the experimental histogram which yields the tunneling detection error (Fig. 3.S1(a)) of E_T (E_N) ~ 1.4 % (0.7 %) where the E_T (E_N) corresponds to the infidelity for detecting the tunneling (no-tunneling) events.

Based on the tunneling detection infidelities, we extract the state measurement fidelities by fitting the Larmor oscillation curve to the numerical model which comprises the state relaxation, false initialization, and the thermal tunneling errors, where the following parameters describe the error rates respectively.

α_S : Thermal tunneling probability of the singlet (S) state

$\beta_{T(S)}$: Probability for the qubit state to be initialized to the triplet (singlet) state

: Relaxation probability ~ τ_{out}/T_1 ~ 0.3% where we use T_1 ~ 337 μs previously measured in Ref. [23] as a rough estimate. While T_1 time can

be different depending on tuning conditions, we obtain measurement fidelity consistent with that of gate set tomography (see section S5 below).

With $P_{\mathrm{flip}}(\tau) \sim \sin^2(\pi \Delta B_z \tau)$ corresponding to the ideal diabatic Larmor oscillation under the magnetic field gradient ΔB_z, we estimate the probability $P_{\mathrm{i}}(\tau)$ (i = S, T_0, T_+, T_-), which is the realistic probability for the qubit state to be at one of the two-spin states after the manipulation. We assume the polarized triplet states T_+, and T_- states are not involved in the coherent dynamics at the manipulation stage, and all three triplet states have the same relaxation rates to the ground (singlet) state. We also suppose that false initialization probability to each of three triplet states is all equal to $\beta_{\mathrm{T}}/3$. The estimation procedure is as follows.

i) $P_S(\tau)$: Probability for the final qubit state to be S after the manipulation.

- Initializes to S (β_{S}), does not flip under the manipulation pulse (1- $P_{\mathrm{flip}}(\tau)$)
- Initializes to S (β_{S}), flip under the manipulation pulse ($P_{\mathrm{flip}}(\tau)$), relax to the ground state (γ)
- Initializes to T_0 ($\beta_{\mathrm{T}}/3$), flip under the manipulation pulse ($P_{\mathrm{flip}}(\tau)$)
- Initializes to T+ or T- ($2\beta_{\mathrm{T}}/3$), relax to the ground state (γ)

$$\Rightarrow P_S(\tau) = \beta_{\mathrm{S}}[1 - P_{\mathrm{flip}}(\tau) + P_{\mathrm{flip}}(\tau)\gamma] + \beta_{\mathrm{T}}/3\,[P_{\mathrm{flip}}(\tau) + (1 - P_{\mathrm{flip}}(\tau)\gamma)] + 2\beta_{\mathrm{T}}/3\,\gamma$$

ii) $P_{T0}(\tau)$: Probability for the final qubit state to be the T_0 after the manipulation.

- Initialize to S (β_{S}), flip under the manipulation pulse ($P_{\mathrm{flip}}(\tau)$), does not relax to the ground state (1-γ)
- Initialize to T_0 ($\beta_{\mathrm{T}}/3$), does not flip under the manipulation pulse (1-$P_{\mathrm{flip}}(\tau)$), does not relax to the ground state (1-γ)

$$\Rightarrow P_{T0}(\tau) = \beta_{\mathrm{S}} P_{\mathrm{flip}}(\tau)(1-\gamma) + \beta_{\mathrm{T}}/3\,(1 - P_{\mathrm{flip}})(1-\gamma)$$

iii) $P_{T+}(\tau)$ ($P_{T-}(\tau)$) : Probability for the final qubit state to be the T+ (T-) after the manipulation.

- Initialize to T+ (T-) ($\beta_T/3$), does not relax to the ground state (1-γ)

$$\Rightarrow P_{T+}(\tau) = P_{T-}(\tau) = \beta_T/3\,(1-\gamma)$$

Combined with the tunneling detection infidelities, the probability for the tunneling event to be detected $P_D(\tau)$ can be calculated as, $P_D(\tau) = (P_{T0}(\tau) + P_{T+}(\tau) + P_{T-}(\tau))(1-E_T) + P_S(\tau)E_N + \alpha_S P_S(\tau)(1-E_T)$. We neglect the terms proportional to $E_T \cdot E_N$. By fitting the $P_D(\tau)$ to the measured Larmor oscillation (Fig. 3.S1(b)), we extract the thermal tunneling error $\alpha_S \sim 0.6$ %, and $\beta_T < 0.1$ %. Note that the adaptive initialization scheme described above facilitates very low false initialization error β_T and we expect the accurate measure of the β_T should be possible with the self-consistent tomography schemes [41]. Also, large $E_{ST}/k_B T_e$ at the EST readout position provided by singlet-triplet splitting E_{ST} on the order of 30 GHz [9] enables $\alpha_S < 1$ %. Based on the error rates, we evaluate the singlet (triplet) measurement fidelity F_S (F_{T0}) ~ 99.28 % (~ 98.53 %) yielding the total measurement fidelity about 99 %. This corresponds to the quantum oscillation visibility of ~ 98 % consistent with the observation.

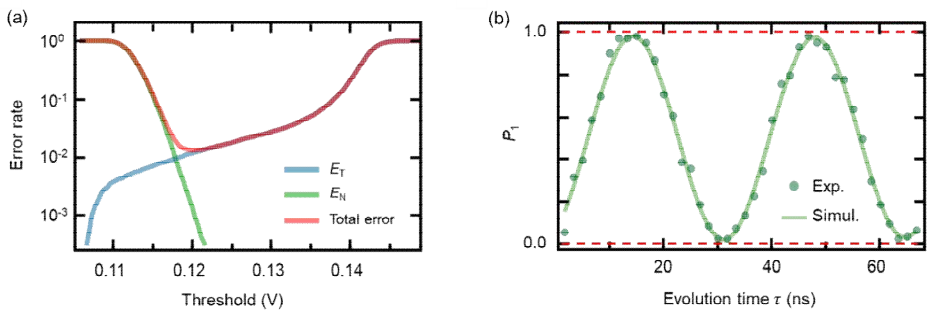

Fig. 3.S1. Quantum oscillation visibility analysis. (a) Tunneling (no-tunneling) detection infidelity shown in blue (green) curves. At the optimum threshold voltage, the error rate for the tunneling (no-tunneling) detection E_T (E_N) ~ 1.4 % (0.7 %) is obtained. The red curve corresponds to the total error ($E_T + E_N$) as a function of the threshold voltage. (b) Experimental Larmor oscillation curve (green dot) and the numerical model (green curve) comprising the thermal tunneling, false initialization, and the relaxation errors. Fit to the model yield thermal tunneling

error (α_S) ~ 0.6 % with the false initialization error (β_T) < 0.1 %.

5.3.4. Application of Bayesian estimators for active feedback mode

Although the heralded mode operation exemplifies the performance of the EST readout-based Hamiltonian estimator with minimal overhead in the Bayesian circuit, the main drawback of this mode is the low duty cycle (actual operation/waiting time) since one has to wait for desired ΔB_z to happen. Depending on a preset tolerance, the resulting duty cycle can be < 1%. Thus we further develop our methodology using ac-driven qubit operation in active feedback mode. The pulse sequence for qubit operation is the same as in Fig. 3(b) except that a sinusoidal RF pulse is applied to V_M using the frequency detected in the probe step to resonantly modulate $J(\varepsilon)$. In this manner, the total waiting time is reduced down to one probe step (70 shots x 26 μs = 1.82 ms). Fig. 4(a) shows the coherent Rabi oscillation measured as a function of the RF pulse duration and controlled detuning δf. The pulse amplitude A_{RF} (measured at the output of the signal generator) is chosen to maximize the Q factor $Q_{Rabi} = f_{Rabi} T_{Rabi} \approx 12$ with the Rabi frequency f_{Rabi} of 6.05 MHz and the Rabi decay time T_{Rabi} of 1.71 μs (see the inset to Fig.4 (a)). Notably, the oscillation visibility reaches approximately 97.6 %, (Fig. 4(b)). This near-ideal visibility of the RF-driven oscillation even without dynamic nuclear polarization again reveals the precise qubit frequency estimation and high measurement fidelity simultaneously enabled by the EST readout-based Bayesian estimator.

Furthermore, we perform the standard randomized benchmarking (RB) and interleaved randomized benchmarking (IRB) where single-qubit gates X, Y, X/2, Y/2, −X/2, and −Y/2 are interleaved to random Clifford gates [42-44]. The recovery gate is chosen such that the final state is ideally singlet, and the gate fidelity is obtained by fitting the measured data to the exponentially decaying curve (see 5.3.4.S1). From RB and IRB, we find

F_{avg} of 96.80 % and F_X of 99.13 %, the latter being close to the Q-factor limited value $e^{-1/(2Q_{Rabi})^2} = 99.76 \pm 0.03$ %.

To compare the state preparation and measurement (SPAM) errors between two operation modes, we perform gate-set tomography (GST) [41] for the active feedback mode. Fig. 4(d) shows the density matrix (top row) and the Pauli transfer matrix (PTM, bottom row), which are obtained using a single qubit GST protocol with a gate set {I, X/2, and Y/2} (see 5.3.4.S1). By comparing the measured PTM to the ideal PTM, we obtain $F_{X/2}$ = 99.05 % and $F_{Y/2}$ =98.2 %, consistent with the values obtained from IRB. Furthermore, the GST yields the initialization fidelity of 99.7% and measurement fidelity of 98.3%. We ascribe slightly lower initialization and measurement fidelity for the active feedback mode compared to the heralded mode to an additional leakage probability through S-T_+ anticrossing while preparing (projecting) a state on the x(z)-axis of the Bloch sphere. Nevertheless, these results consolidate the high gate fidelity and low SPAM error illustrating that our Hamiltonian estimation enables the real-time application of general qubit operations in GaAs with the fidelities reaching the level of singlet-triplet qubits in Si devices [45].

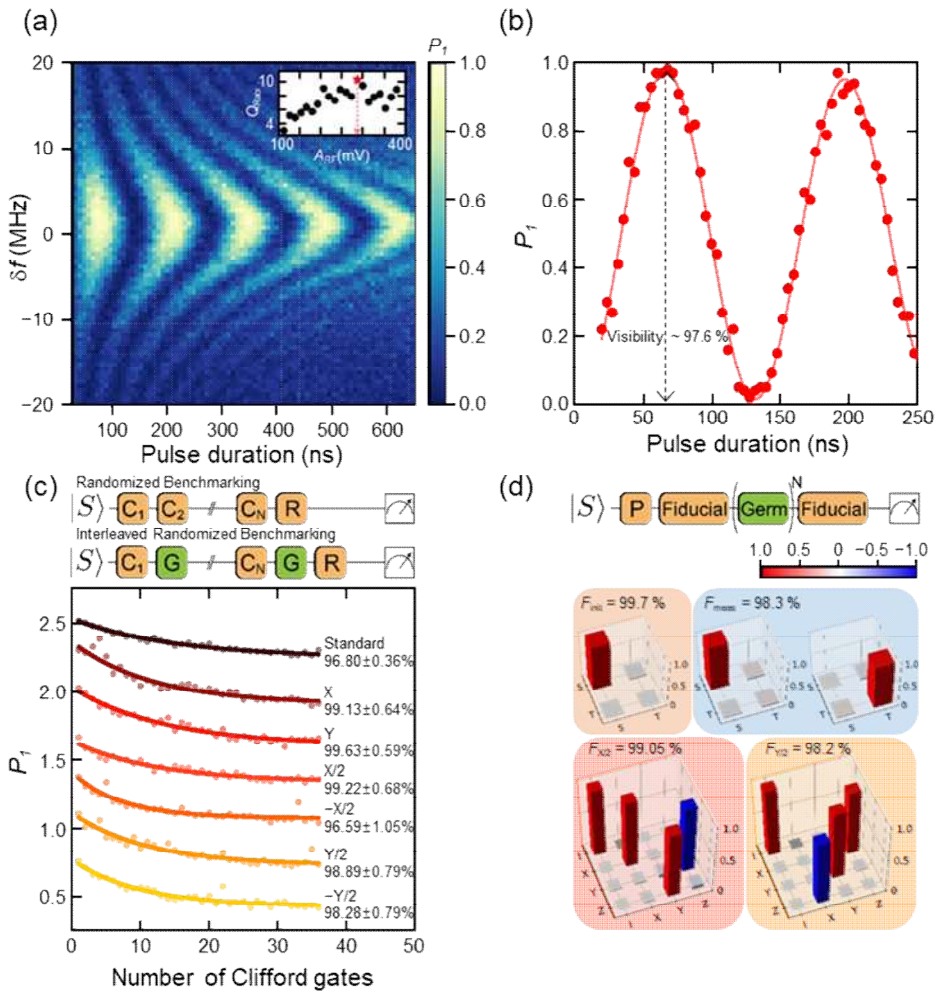

Fig. 4. (a) Rabi oscillation of P_1 as a function of controlled detuning δf and pulse duration. Inset: Oscillation quality factor Q_{Rabi} as a function of RF amplitude A_{RF} (measured at the output of the signal generator). The red star-shaped symbol marks the condition for the maximum Q_{Rabi}. (b) Representative Rabi oscillation at the resonant driving frequency that is actively adjusted with visibility higher than 97 %. The oscillation is fit to the sinusoidal function with the Gaussian envelope, from which Rabi decay time $T_{\mathrm{Rabi}} = 1.71\ \mu s$ is obtained. (c) P_1 as a function of the number of random Clifford gates obtained from a single qubit standard and interleaved randomized benchmarking. Traces are offset by 0.3 for clarity. Each single-qubit gate fidelity annotates the corresponding benchmarking sequence. (d) Density matrices (top row) and Pauli transfer matrices (bottom row) evaluated by gate set tomography. Each matrix is annotated by the corresponding fidelities.

5.3.4.S1. Randomized Benchmarking and Gate Set Tomography

Randomized benchmarking (RB and IRB)*:* A single-qubit Clifford gate set is constructed using primitive gates I, X, Y, ±X/2, and ±Y/2, which are implemented by calibrated RF bursts. For concatenating RF bursts, we use an idle time of 16 ns. The elements of the Clifford gate set are randomly selected during the benchmarking. Each point in Fig. 4(c) is obtained by averaging 1000 single-shot measurements per sequence. The measurement data obtained from the standard randomized benchmarking (RB) is fitted to the exponentially decaying curve $P_1(m) = Ap_{\text{avg}}^m + B$ where m denotes the number of Clifford gates. The average gate fidelity F_{avg} is then determined by the depolarizing parameter p_{avg} as $\left(1 + p_{\text{avg}}\right)/2$ [44].

The gate fidelity of each primitive gate, on the other hand, is obtained with respect to the reference random Clifford gate sets using interleaved randomized benchmarking (IRB) protocol [12]. The measurement data from the interleaved randomized benchmarking is fitted to the same exponentially decaying curve $P_1(m) = Ap_{\text{gate}}^m + B$ to obtain the depolarizing parameter p_{gate}. The gate fidelity is then obtained as $\left(1 + p_{\text{gate}} / p_{\text{avg}}\right)/2$, where the effect of the reference RB is reflected as $1/p_{\text{avg}}$ [44].

Gate set tomography (GST): We use a single qubit gate set of {I, X/2, Y/2}, where the notation for each element is the same as those in the RB. Specifically, the length of all gates is fixed to a specific length, including the idle gate I. Compositing the elements in the gate set, we conducted the GST experiment with germs {I, X/2, Y/2, X/2∘Y/2, X/2∘X/2∘Y/2} and fiducials {null, X/2, Y/2, X/2∘X/2, X/2∘X/2∘X/2, Y/2∘Y/2∘Y/2} and the results are analyzed using the open-source python package, pyGSTi [46].

5.4. Conclusion

In conclusion, using energy-selective tunneling readout-based Hamiltonian parameter estimation of an ST_0 qubit in GaAs, we demonstrated passive and active suppression of nuclear noise, leading to T_2* above 800 ns and near-ideal quantum oscillation visibility consistent with low SPAM errors below 0.3%. The flexibility of the EST readout-based Bayesian circuit facilitates various quantum operations in both heralded and active feedback mode, enabling the execution of widely used validation protocols such as randomized benchmarking and gate set tomography. With the large SNR of the charge sensor and real-time capability, the EST readout-based Hamiltonian estimation is potentially useful for advanced quantum control protocols with affordable overhead in classical signal processing, such as error mitigation schemes and entanglement demonstration experiments, where fast qubit parameter calibration with large readout visibility is essential [27].

5.5. References

[1] C. Ferrie, C. Granade, G. Paz-Silva, and H. M. Wiseman, *Bayesian quantum noise spectroscopy*, New J. Phys. **20,** 123005 (2018).

[2] M. D. Shulman, S. P. Harvey, J. M. Nichol, S. D. Bartlett, A. C. Doherty, V. Umansky, and A. Yacoby, *Suppressing qubit dephasing using real-time Hamiltonian estimation*, Nat. Commun. **5,** 5156 (2014).

[3] H. Bluhm, S. Foletti, D. Mahalu, V. Umansky, and A. Yacoby, *Enhancing the Coherence of a Spin Qubit by Operating it as a Feedback Loop That Controls its Nuclear Spin Bath*, Phys. Rev. Lett. **105,** 216803 (2010).

[4] A. Sergeevich, A. Chandran, J. Combes, S. D. Bartlett, and H. M. Wiseman, *Characterization of a qubit Hamiltonian using adaptive measurements in a fixed basis*, Physical Review A **84,** 052315 (2011).

[5] G. Waldherr *et al.*, *High-dynamic-range magnetometry with a single nuclear spin in diamond*, Nat. Nanotech. **7,** 105 (2012).

[6] N. M. Nusran, M. U. Momeen, and M. V. G. Dutt, *High-dynamic-range magnetometry with a single electronic spin in diamond*, Nat. Nanotech. **7,** 109 (2012).

[7] T. Nakajima *et al.*, *Coherence of a Driven Electron Spin Qubit Actively Decoupled from Quasistatic Noise*, Physical Review X **10,** 011060 (2020).

[8] M. Veldhorst *et al.*, *An addressable quantum dot qubit with fault-tolerant control-fidelity*, Nat. Nanotech. **9,** 981 (2014).

[9] J. Yoneda *et al.*, *A quantum-dot spin qubit with coherence limited by charge noise and fidelity higher than 99.9%*, Nat. Nanotech. **13,** 102 (2018).

[10] O. E. Dial, M. D. Shulman, S. P. Harvey, H. Bluhm, V. Umansky, and A. Yacoby, *Charge Noise Spectroscopy Using Coherent Exchange Oscillations in a Singlet-Triplet Qubit*, Phys. Rev. Lett. **110,** 146804 (2013).
[11] J. M. Elzerman, R. Hanson, L. H. W. van Beveren, B. Witkamp, L. M. K. Vandersypen, and L. P. Kouwenhoven, *Single-shot read-out of an individual electron spin in a quantum dot*, Nature **430,** 431 (2004).
[12] R. Hanson, L. H. W. van Beveren, I. T. Vink, J. M. Elzerman, W. J. M. Naber, F. H. L. Koppens, L. P. Kouwenhoven, and L. M. K. Vandersypen, *Single-shot readout of electron spin states in a quantum dot using spin-dependent tunnel rates*, Phys. Rev. Lett. **94,** 196802 (2005).
[13] J. R. Petta, A. C. Johnson, J. M. Taylor, E. A. Laird, A. Yacoby, M. D. Lukin, C. M. Marcus, M. P. Hanson, and A. C. Gossard, *Coherent manipulation of coupled electron spins in semiconductor quantum dots*, Science **309,** 2180 (2005).
[14] J. Medford *et al.*, *Self-consistent measurement and state tomography of an exchange-only spin qubit*, Nat. Nanotech. **8,** 654 (2013).
[15] C. Barthel, D. J. Reilly, C. M. Marcus, M. P. Hanson, and A. C. Gossard, *Rapid Single-Shot Measurement of a Singlet-Triplet Qubit*, Phys. Rev. Lett. **103,** 4 (2009).
[16] C. Barthel, J. Medford, H. Bluhm, A. Yacoby, C. M. Marcus, M. P. Hanson, and A. C. Gossard, *Relaxation and readout visibility of a singlet-triplet qubit in an Overhauser field gradient*, Phys. Rev. B **85,** 7 (2012).
[17] P. Harvey-Collard *et al.*, *High-Fidelity Single-Shot Readout for a Spin Qubit via an Enhanced Latching Mechanism*, Physical Review X **8,** 021046 (2018).
[18] T. Nakajima *et al.*, *Robust Single-Shot Spin Measurement with 99.5% Fidelity in a Quantum Dot Array*, Phys. Rev. Lett. **119,** 017701 (2017).
[19] L. A. Orona, J. M. Nichol, S. P. Harvey, C. G. L. Bottcher, S. Fallahi, G. C. Gardner, M. J. Manfra, and A. Yacoby, *Readout of singlet-triplet qubits at large magnetic field gradients*, Phys. Rev. B **98,** 125404 (2018).
[20] K. Eng *et al.*, *Isotopically enhanced triple-quantum-dot qubit*, Sci. Adv. **1,** 7 (2015).
[21] L. A. Tracy, D. R. Luhman, S. M. Carr, N. C. Bishop, G. A. Ten Eyck, T. Pluym, J. R. Wendt, M. P. Lilly, and M. S. Carroll, *Single shot spin readout using a cryogenic high-electron-mobility transistor amplifier at sub-Kelvin temperatures*, Applied Physics Letters **108,** 5 (2016).
[22] J. P. Dehollain *et al.*, *Optimization of a solid-state electron spin qubit using gate set tomography*, New J. Phys. **18,** 9 (2016).
[23] W. Jang, J. Kim, M. K. Cho, H. Chung, S. Park, J. Eom, V. Umansky, Y. C. Chung, and D. Kim, *Robust energy-selective tunneling readout of singlet-triplet qubits under large magnetic field gradient*, Npj Quantum Information **6,** 7 (2020).
[24] D. Keith, M. G. House, M. B. Donnelly, T. F. Watson, B. Weber, and M. Y. Simmons, *Single-Shot Spin Readout in Semiconductors Near the Shot-Noise Sensitivity Limit*, Physical Review X **9,** 041003 (2019).
[25] D. Keith, S. K. Gorman, L. Kranz, Y. He, J. G. Keizer, M. A. Broome, and M. Y. Simmons, *Benchmarking high fidelity single-shot readout of semiconductor qubits*, New J. Phys. **21,** 063011 (2019).
[26] M. A. I. Johnson, M. T. Mądzik, F. E. Hudson, K. M. Itoh, A. M. Jakob, D. N. Jamieson, A. Dzurak, and A. Morello, *Beating the thermal limit of qubit initialization with a Bayesian 'Maxwell's demon'*, arXiv: **2110,** .02046 (2021).
[27] J. P. Dehollain *et al.*, *Bell's inequality violation with spins in silicon*, Nat.

Nanotech. **11,** 242 (2016).
[28] F. K. Malinowski *et al.*, *Spectrum of the Nuclear Environment for GaAs Spin Qubits*, Phys. Rev. Lett. **118,** 177702 (2017).
[29] H. F. Qiao, Y. P. Kandel, K. Y. Deng, S. Fallahi, G. C. Gardner, M. J. Manfra, E. Barnes, and J. M. Nichol, *Coherent Multispin Exchange Coupling in a Quantum-Dot Spin Chain*, Physical Review X **10,** 031006 (2020).
[30] I. Ahmed, A. Chatterjee, S. Barraud, J. J. L. Morton, J. A. Haigh, and M. F. Gonzalez-Zalba, *Primary thermometry of a single reservoir using cyclic electron tunneling to a quantum dot*, Communications Physics **1,** 66 (2018).
[31] C. P. Scheller, S. Heizmann, K. Bedner, D. Giss, M. Meschke, D. M. Zumbuhl, J. D. Zimmerman, and A. C. Gossard, *Silver-epoxy microwave filters and thermalizers for millikelvin experiments*, Applied Physics Letters **104,** 5 (2014).
[32] J. Stehlik, Y. Y. Liu, C. M. Quintana, C. Eichler, T. R. Hartke, and J. R. Petta, *Fast Charge Sensing of a Cavity-Coupled Double Quantum Dot Using a Josephson Parametric Amplifier*, Physical Review Applied **4,** 014018 (2015).
[33] Y. Makhlin, G. Schon, and A. Shnirman, *Quantum-state engineering with Josephson-junction devices*, Reviews of Modern Physics **73,** 357 (2001).
[34] C. Barthel, D. J. Reilly, C. M. Marcus, M. P. Hanson, and A. C. Gossard, *Rapid Single-Shot Measurement of a Singlet-Triplet Qubit*, Phys. Rev. Lett. **103,** 160503 (2009).
[35] C. Barthel, M. Kjaergaard, J. Medford, M. Stopa, C. M. Marcus, M. P. Hanson, and A. C. Gossard, *Fast sensing of double-dot charge arrangement and spin state with a radio-frequency sensor quantum dot*, Phys. Rev. B **81,** 161308 (2010).
[36] A. Noiri, K. Takeda, J. Yoneda, T. Nakajima, T. Kodera, and S. Tarucha, *Radio-Frequency-Detected Fast Charge Sensing in Undoped Silicon Quantum Dots*, Nano Lett. **20,** 947 (2020).
[37] F. H. L. Koppens *et al.*, *Control and detection of singlet-triplet mixing in a random nuclear field*, Science **309,** 5739 (2005).
[38] S. Foletti, H. Bluhm, D. Mahalu, V. Umansky, and A. Yacoby, *Universal quantum control of two-electron spin quantum bits using dynamic nuclear polarization*, Nat. Phys. **5,** 903 (2009).
[39] F. Martins, F. K. Malinowski, P. D. Nissen, E. Barnes, S. Fallahi, G. C. Gardner, M. J. Manfra, C. M. Marcus, and F. Kuemmeth, *Noise Suppression Using Symmetric Exchange Gates in Spin Qubits*, Phys. Rev. Lett. **116,** 5 (2016).
[40] A. Morello *et al.*, *Single-shot readout of an electron spin in silicon*, Nature **467,** 687 (2010).
[41] R. Blume-Kohout, J. K. Gamble, E. Nielsen, K. Rudinger, J. Mizrahi, K. Fortier, and P. Maunz, *Demonstration of qubit operations below a rigorous fault tolerance threshold with gate set tomography*, Nat. Commun. **8,** 14485 (2017).
[42] E. Magesan, J. M. Gambetta, and J. Emerson, *Scalable and Robust Randomized Benchmarking of Quantum Processes*, Phys. Rev. Lett. **106,** 180504 (2011).
[43] E. Magesan, J. M. Gambetta, and J. Emerson, *Characterizing quantum gates via randomized benchmarking*, Physical Review A **85,** 042311 (2012).
[44] E. Magesan *et al.*, *Efficient Measurement of Quantum Gate Error by Interleaved Randomized Benchmarking*, Phys. Rev. Lett. **109,** 080505 (2012).
[45] K. Takeda, A. Noiri, J. Yoneda, T. Nakajima, and S. Tarucha, *Resonantly Driven Singlet-Triplet Spin Qubit in Silicon*, Phys. Rev. Lett. **124,** 5 (2020).

[46] E. Nielsen, K. Rudinger, T. Proctor, A. Russo, K. Young, and R. Blume-Kohout, *Probing quantum processor performance with pyGSTi*, Quantum Science and Technology **5,** 044002 (2020).

Appendix A

A. Fabrication of quantum dot devices

The overall process: Mesa → Ohmic contact → e-beam align marker only→ e-beam gate → optical pad → e-beam (magnet)

A. Mesa etch

Objective : Etch mesa patterns to remove the Si quantum well, preventing the formation of the quantum dots that you do not want. The etching is performed using liquid chemical (wet etching).

1. Clean the sample surface. Repeat the process below 3 times.

   TCE (80℃ 5min) → Acetone (80℃ 5min) → Methanol (80℃ 5min)
   After last process, rinse under IPA for ~ 10 sec and blow dry with N_2.

2. Spin coating of PR.

   Spin S1805 at 5000 RPM for 40 sec.
   Bake at 80℃ for 300 sec.

3. Expose UV onto the sample surface for 15 sec using mask aligner with hard contact mode.

Optimal exposure time depends on the intensity and energy of the UV source (Dose = Intensity/Area × Exposure time). If you use diffrent UV

sources or different materials other than GaAs, you should find the optimal exposure time in order to make the desired pattern.

4. Development

   Soak the sample in MF320 for 40 sec
   Rinse under DI water to stop the development
   Blow dry with N_2

5. Hard baking to make PR more rigid

   Bake at 120℃ for 60 sec while pumping from the bottom of the sample

I recommend the sample to be completely in contact with the surface of the hot plate using vacuum pump, which results in the stable etching condition.

6. Wet etching

   Soak the sample in H_2PO_3 : H_2O_2 : DI = 1 : 1 : 50 volume ratio with slightly agitation for 80 sec (average etching rate = 1.25 nm/sec for GaAs/AlGaAs heterostructure)

Usually, the sample is etched to the depth of 2DEG, but partial etching of AlGaAs layer can lead to the depletion of 2DEG

   Soak the sample in DI water and rinse under DI water to stop the etching

7. PR removal

   Repeat the process below 3 times

   Acetone (80℃ 5min) → Methanol (80℃ 5min) → IPA (80℃ 5min)

   Rinse under IPA

B. Ohmic contact

Objective : Using metal diffusion method, Ohmic contact between 2DEG and diffused metal is formed, enabling 2DEG to be connected to the reservoir.

1. Spin coating of PR.

   Spin SF11 at 5000 RPM for 40 sec.

   Bake at 180℃ for 900 sec while pumping from the bottom of the sample

SF11 is used as lift of resist to improve the lift-off. Sufficient baking time for SF11 is very important, otherwise, SF11 could move away during the development.

Spin S1805 at 5000 RPM for 40 sec

Bake at 80℃ for 300 sec

2. Expose UV onto the sample surface for 15 sec using mask aligner with hard contact mode.

3. Development

   Soak the sample in MF320 for 120 sec

   Rinse under DI water to stop the development

   Blow dry with N_2

4. Strip the resist

   O2 plasma cleaning for 30 sec at 50 W RF power

5. Wet etching to remove the oxide layer

   Soak the sample in $HCl:H_2O=1:1$ for 10 sec

Rinse under DI water to stop the etching

6. Metal deposition

   Evaporate 3 nm Ni at 1 Å/s, 150 nm Au at 2 Å/s, 75 nm Ge at 1.5 Å/s, 56.5 nm Ni at 1 Å/s and 30 nm Au at 2 Å/s

7. Lift-off

   Soak the sample in PG remover with slightly agitation for 30 min at 60℃

   Rinse under DI water

8. Rapid thermal annealing in Ar atmosphere

   Control the temperature as a function of time shown below in order to diffuse the Ni, Ge and Ge deposited into AlGaAs layer.

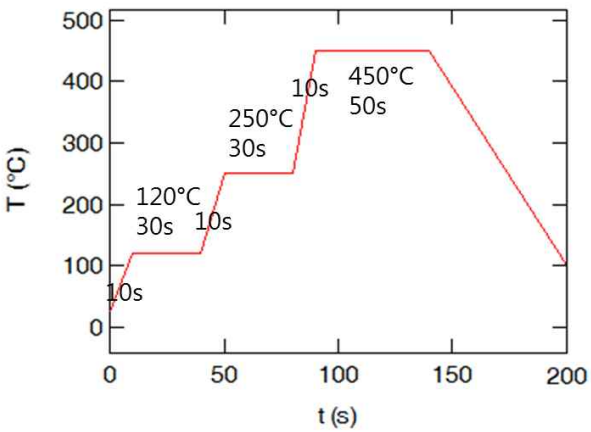

9. Clean the sample surface. Repeat the process below 3 times.

   TCE (80℃ 5min) → Acetone (80℃ 5min) → Methanol (80℃ 5min)

   After last process, rinse under IPA for ~ 10 sec and blow dry with N_2.

C. Align markers

Objective : Align markers are used for fine alignment when making nonogates. Cross-shaped align marker with uniform width should be prepared for high accurate alignment.

1. Spin coating of PR.

   Spin SF11 at 5000 RPM for 40 sec.

   Bake at 180℃ for 900 sec while pumping from the bottom of the sample

   Spin S1805 at 5000 RPM for 40 sec

   Bake at 80℃ for 300 sec

2. Expose UV onto the sample surface for 15 sec using mask aligner with hard contact mode.

3. Development

   Soak the sample in MF320 for 120 sec

   Rinse under DI water to stop the development

   Blow dry with N_2

4. Metal deposition

   Evaporate 25 nm Ti at 1 Å/s and 175 nm Au at 2 Å/s

5. Lift-off

   Soak the sample in PG remover with slightly agitation for 30 min at 60℃

   Sonicate the sample in PG remover for 30 sec

   (I recommend to use teflon beaker to avoid breaking the sample)

   Rinse under DI water

D. nanogates

Objective : Electrical voltage is applied to the nanogates to induce in-plane confinement potential in 2DEG, resulting in the formation of the quantum dots.

1. Spin coating of ER

   Spin PMMA950A3 at 3000 RPM for 60 sec

   Bake at 180℃ for 300 sec

2. Expose e-beam

3. Development

   Soak the sample in MIBK:IPA 1:3 solution for 60 sec

   Rinse under IPA for 30 sec

   Blow dry with N_2

4. Strip the resist

   O2 plasma cleaning for 5 sec at 50 W RF power

5. Wet etching to remove the oxide layer

   Soak the sample in $HCl:H_2O$=1:1 for 3 sec

   Rinse under DI water to stop the etching

6. Metal deposition

   Evaporate 5 nm Ti at 1 Å/s and 30 nm Au at 1 Å/s

7. Lift-off

   Soak the sample in Acetone with slightly agitation for 60 min at 60℃

   Rinse under DI water

E. Bond pads

Objective : Evaporate pads for wire bonding acting as a bridge between the device and the measurement PCB.

1. Spin coating of PR.

   Spin SF11 at 5000 RPM for 40 sec.

   Bake at 180℃ for 900 sec while pumping from the bottom of the sample

   Spin S1805 at 5000 RPM for 40 sec

   Bake at 80℃ for 300 sec

2. Expose UV onto the sample surface for 15 sec using mask aligner with hard contact mode.

3. Development

   Soak the sample in MF320 for 120 sec

   Rinse under DI water to stop the development

   Blow dry with N_2

4. Strip the resist

   O2 plasma cleaning for 30 sec at 50 W RF power

5. Wet etching to remove the oxide layer

   Soak the sample in $HCl:H_2O=1:1$ for 10 sec

   Rinse under DI water to stop the etching

6. Metal deposition

   Evaporate 20 nm Ni at 1 Å/s and 200 nm Au at 2 Å/s

7. Lift-off

Soak the sample in PG remover with slightly agitation for 60 min at 60℃

Rinse under DI water

F. Micromagnet

Objective : Micromagnet is placed near the quantum dots to create the magnetic field gradient in the area where the quantum dots are positioned.

1. Spin coating of ER

Spin PMMA495 A4 at 3500 RPM for 60 sec

Bake at 180℃ for 600 sec

Repeat the process above 3 times to make 540 nm of total ER thickness

Spin PMMA950 A6 at 3500 RPM for 60 sec

Bake at 180℃ for 600 sec

Total ER thickness will be about 900 nm enough for evaporating the micromagnet with 200 nm thickness

2. Expose e-beam

3. Development

Soak the sample in MIBK:IPA 1:3 solution for 60 sec

Rinse under IPA for 30 sec

Blow dry with N_2

4. Reactive ion etching

For adhesion enhancement, etch the surface of AlGaAs to form rough surface under the condition such that Ar 80 sccm, Cl_2 20 sccm and working pressure 75 mTorr at 150 W RF power for 40 sec

5. Metal deposition

   Evaporate 10 nm Ni at 1 Å/s, 200 nm Co at 2 Å/s and 5 nm Au at 1 Å/s

6. Lift-off

   Soak the sample in Acetone for 60 min

   Rinse under DI water

Appendix B

B. Basic concept of RF-reflectometry & Setup

RF-reflectometry is one of the key method enabling the fast and sensitive measurement. So, it can be exploited widely in order to measure the spin degree of freedom for few electrons because the spin information should be measured before the decoherence is occurred by the interaction between the environment and qubits. The RF-reflectometry setup is consist of outer RF signal transmission lines (Fig. 1) and RLC tank circuit including the resistance of the sensor quantum dots (Fig. 2(a)). As electromagnetic waveswith RF are reflected at the interface between a medium having different impedance Z, the difference between the impedance for outer RF signal lines, usualy having Z_0 = 50 Ω, and the impedance for the tank circuit leads to the change of the reflectance Γ defined as $\Gamma = \frac{Z-Z_0}{Z+Z_0}$.

The impedance for RLC tank circuit in figure xx can be calculated as $Z(w) = iwL + \frac{1}{\frac{1}{R}+iwC_P}$ where L is the inductance of inductor positioned in PCB surface, C_p is the parasitic capacitance which can result from stray capacitance of bond wires or from the capacitance between the Ohmic contacts and the 2DEG, and R is the resistance of the sensor quantum dot which is higher than the inverse of conductance quantum.

At the resonance condition where the imaginary part of Z(w) become zero, the resonance frequency f_R is determined as $f_R = \frac{1}{2\pi}\sqrt{\frac{1}{LC_P} - (\frac{1}{RC_P})^2} \sim \frac{1}{2\pi}\sqrt{\frac{1}{LC_P}}$ in first order approximation. Because how much the tank circuit reflects depends on the frequency of the RF and the change in the reflectance is large near the resonance frequency, RF with resonance frequency is used as a carrier for RF-reflectometry whose

frequency is usually around 150 MHz.

Therefore, the impedance for the tank circuit at the resonance condition is determined as $Z(f_R) \sim \frac{L}{RC_p}$ depending on the conductance of the sensor quantum dot. This imepedance $Z(f_R)$ should be matched to the impedance of outer RF signal lines Z_0 in order to maximize the sensitivity by adjusting R. So, small changes in R lead to large changes in the reflectance, which is described in the Fig. 2(b) showing the resonant behavior as a function of a carrier frequency.

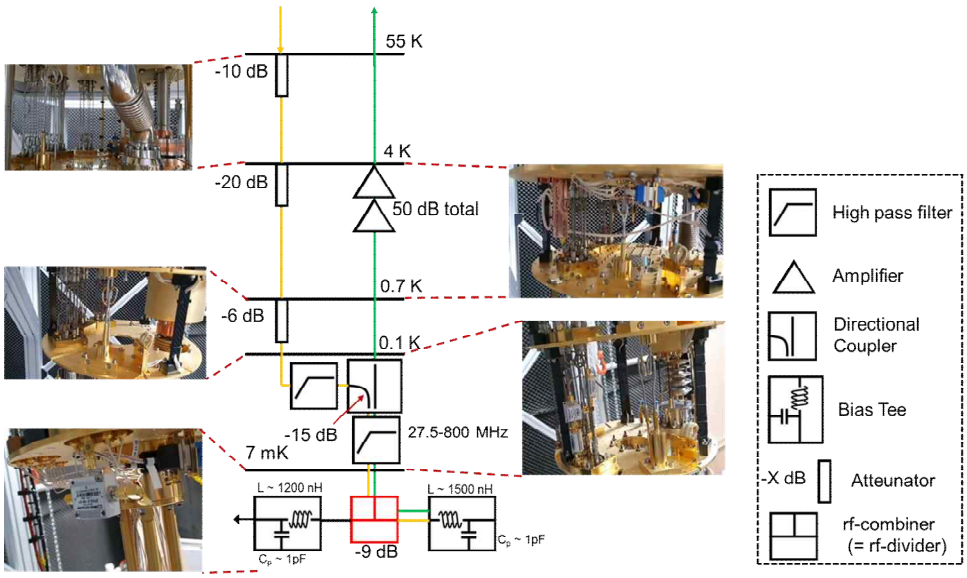

Fig 1. Overview of RF-reflectometry setup showing outer RF signal transmission lines. Real pictures are shown according to the plates with a different temperature.

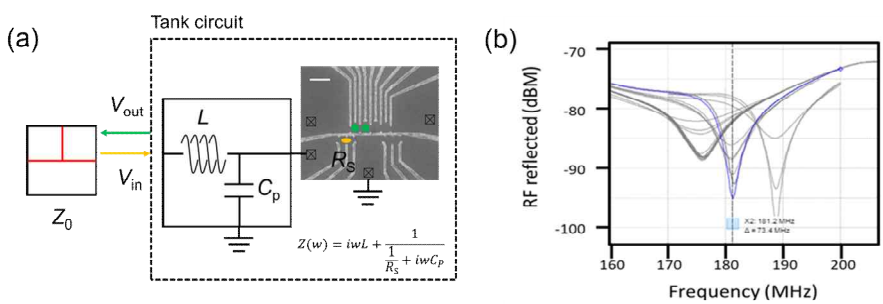

Fig. 2. (a) RF-reflectometry setup showing RLC tank circuit part. Rs is a resistance of a sensor quantum dot, L is the inductance of inductor positioned in PCB surface,

C_p is the parasitic capacitance. (b) RF reflectance as a function of a carrier frequency, showing a resonant behavior.

Abstract in Korean

고대 시대에 신비한 돌로 알려진 자석의 발견을 시작으로, 근대의 Stern-Gerlach 의 실험을 통해 밝혀진 spin 의 발견은 우리 생활에 엄청난 영향을 주어 큰 변화에 박차를 가하였다. 물질의 기본 물리량인 질량, 전하 와 더불어 spin 은 현재 생활 곳곳에 많이 응용이 되고 있다. 특히, 정보를 저장하고 처리하기 위한 전자소자 분야에는 spin 이 없어서는 안되는 물리량이다. 시스템의 크기에 따라, classical spin picture 로 설명 가능한 앙상블 스핀 system 과, quantum spin picture 로 설명 가능한 few-electron spin system 으로 응용처를 분류해 볼 수 있다. Classical spin 의 경우 Spintronics 라는 분야에서 spin 메모리 소자와 spin transistor 로 spin 이 응용되고 있고, Quantum spin 의 경우 최근 양자정보 분야의 대표인 양자컴퓨팅 분야에서 전자 spin 이 응용 되고 있다. 이러한 응용을 위해 공통적으로 중요한 부분은, 전자 spin 상태를 정밀하게 조절하고 읽어내는 기술이다.

이 논문은 크게 두 부분으로 나뉘어져 있다. 전반부는 SmB_6 single crystal 의 표면에 흐르는 ensemble spin 을 검출하는 연구에 관련된 내용이다. SmB_6 는 대표적인 Kondo insulator 로서, 그 동안 SmB_6 표면에 spin-momentum locking 특성이 존재한다는 것을 보여주는 이론적인 연구와 실험 연구가 진행되어 왔다. 하지만 그 동안 전기적인 측정 방법으로 spin 측정 연구가 진행되지 않았고, potentiometric 측정법이라 불리는 방법을 차용, 강자성체를 ensemble spin 의 방향을 측정하는 검출기로 이용하여, SmB_6 표면에 spin polarized 전류가 흐름을 보였다. 또한, 전류와 측정전압용 터미널 위치를 서로 바꾸어, 강자성체에 의해 만들어진 spin polarized 전류를 역으로 SmB_6 표면 상태를 이용해 측정 하였다. 이러한 결과는 SmB_6 표면에 spin-momentum locking 관계가 있음을 보여주는 전기적 측정 결과라고 볼 수 있다.

후반부 연구 내용은, GaAs 양자점 소자에서 spin singlet-triplet qubit 를 형성하고, 그 qubit 의 spin 상태를 조절하고 측정하는 연구에 대한 내용이다. singlet-triplet qubit 상태의 spin-to-charge conversion 을 성공 시키기 위해서, Elzerman 유형 readout 이라고 불리는 이중 양자점과 reservoir 사이의 energy selective tunneling (EST) 을 이용하는 새로운 방법이 시현 되었다. 이 방법을 더 개선하기 위해, 실시간 Hamiltonian parameter estimation 방법을 적용하여, 앞서 언급한 EST 측정법의 정확도를 향상 시켰다. Adaptive initialization 와 real-time Bayesian inference 을 기반으로 하는 효과적인 qubit 진동수 추정법의 도입과 함께, 측정 정확도의 최적화는 single-shot 측정 시간을 평균 16 us 까지 줄이는 것을 가능하게 했다. 또한, active feedback 방법의 도입을 통해, 양자 진동의 visibility, single-shot 측정의 정확도, 상태 초기화 정확도를 각각 97.7%, 99%, 99.7% 이상으로 향상 시키는데 성공하였다.

시스템의 크기에 따라서, 또는 시스템의 action 값이 플랑크 상수 근처인지 아닌지에 따라, 시스템의 spin 을 조절하고 측정하기 위해 적절한 방법이 고려되어야 한다. 이번 연구는, 임의의 quasiparticle 의 spin 상태를 정확하게 조절하고 측정하기 위해서, spin-to-charge conversion, measurement setup 그리고 design for device structure 부분을 어떻게 계획하고 확장해야 하는가 라는 부분에 있어 도움이 될 것으로 기대 된다.